ALMA MATER STUDIORUM
UNIVERSITÀ DI BOLOGNA

DOTTORATO DI RICERCA IN

IL FUTURO DELLA TERRA, CAMBIAMENTI CLIMATICI E SFIDE SOCIALI

Ciclo 36

Settore Concorsuale: 04/A4 - GEOFISICA
Settore Scientifico Disciplinare: GEO/12 OCEANOGRAFIA E FISICA DELL'ATMOSFERA

EMILIA-ROMAGNA COASTAL SEDIMENT MODELLING AND DEPOSITIONAL PATTERNS

Presentata da: Emilia Rizzi

Coordinatore Dottorato
Prof. ssa Silvana Di Sabatino

Supervisore
Prof. Andrea Valentini

Co-supervisori
Prof. ssa Nadia Pinardi
Jacopo Alessandri
Ivan Federico

Esame finale anno 2025

[...]

If you can dream - and not make dreams your master;

If you can think - and not make thoughts your aim;

If you can meet with Triumph and Disaster

And treat those two impostors just the same;

[...]

If you can make one heap of all your winnings

And risk it on one turn of pitch-and-toss,

And lose, and start again at your beginnings

And never breathe a word about your loss;

[...]

If you can talk with crowds and keep your virtue,

Or walk with Kings - nor lose the common touch,

If neither foes nor loving friends can hurt you,

If all men count with you, but none too much;

If you can fill the unforgiving minute

With sixty seconds' worth of distance run,

Yours is the Earth and everything that's in it,

And - which is more - you'll be a Man, my son!

Rudyard Kipling, If: A Father's Advice to His Son

Abstract

Coastal erosion is a global problem that is projected to worsen in the context of climate change, thus prompting significant interest in the development of practical tools for predicting the coastal response to various climate scenarios and for identifying optimal management strategies. The Emilia-Romagna coastline is a case in point, and the present thesis aims to design a sediment transport model that correctly represents the sediment dispersal patterns and the erosion and deposition patterns of the area.

The numerical model used is SHYFEM-MPI, which uses a finite element method and works on unstructured triangular grids. The model offers a sediment transport module, and it is possible to consider multiple sediment classes. Specifically, this thesis employs five distinct grain sizes. To ascertain the most suitable model configuration for sediment transport, a sensitivity analysis was conducted. The findings revealed that the horizontal diffusion coefficient exerts minimal influence on sediment transport, and the most effective method for describing sediment transport in the study area is the Van Rijn method.

A one-year simulation was conducted for the year 2019. The model demonstrated competence in its depiction of the along-shore sediment transport, which is recognised as the predominant transport pathway, albeit with lower concentrations than those that were empirically measured. This discrepancy is hypothesised to be attributable to an absence of sediment boundary conditions at the open boundary. Furthermore, during the flood event, the model exhibited a plume geometry that was analogous to the observed one. Following a year-long simulation period, the model exhibited erosion and deposition patterns analogous to the observed ones, and the grain size pattern began to mirror the local pattern.

This thesis signifies the initial attempt to utilise a finite element model with multiple sediment classes on the Emilia-Romagna coast. The most significant challenge was the paucity of sediment data, particularly from rivers. To enhance this model further, it is recommended that

turbidity and discharge measurements be taken at river mouths, and that SHYFEM-MPI be coupled with a third-generation wave model.

Contents

Nomenclature

ATL	Atlantic satellite dataset
$A_{b,w}$	bottom orbital diameter given by waves [m]
$C_{eq(i)}$	equilibrium concentration for the sediment class i [kgm^{-3}]
$C_{l(i)}$	concentration of sediment class i at level l [kgm^{-3}]
CC	Climate Change
CMCC	Centro Euro-Mediterraneo sui Cambiamenti Climatici
CMEMS	Copernicus Marine Service
CMOC	Central Mediterranean Overturning Circulation
D_{50}	median sediment diameter [m]
$D_{(i)}$	diameter of sediment class i [m]
$D_{*(i)}$	dimensionless diameter for sediment class i [-]
EACC	Eastern Adriatic Coastal Current
$ED_{(i)}$	net exchange flux between the sea bottom and the water column for sediment class i [$kgm^{-2}s^{-1}$]
f_{cw}	bed friction factor [-]
g	gravity acceleration [ms^{-2}]
GLO	Global satellite dataset
h	water depth [m]
h_a	averaged depth along the fetch direction [m]
h_b	bottom elevation [m]
H_l	thickness of vertical level l [m]
H_s	significant wave height [m]
k	wave number [-]

K_h	horizontal turbulent diffusion coefficient $[m^2 s^{-1}]$
$K_{sed,h}$	horizontal turbulent diffusion coefficient for sediments $[m^2 s^{-1}]$
$K_{v,l}$	vertical turbulent coefficient for the layer l $[m^2 s^{-1}]$
MAE	Mean Absolute Error $[kgm^{-3}]$
N	number of observations [-]
q	total bedload transport rate $[m^2 s^{-1}]$
q_x	total bedload transport rate in the x direction $[m^2 s^{-1}]$
q_y	total bedload transport rate in the y direction $[m^2 s^{-1}]$
R	Pearson correlation coefficient [-]
RMSE	Root Mean Square Error $[kgm^{-3}]$
SPM	Suspended Particulate Matter
SSC	Suspended Sediment Concentration
SSH	Sea Surface Height [m]
T	wave period [s]
TSM	Total Suspended Matter
T_m	mean wave period [s]
T_p	peak wave period [s]
UNIFE	University of Ferrara
U_{100}	current velocity at one meter from seabed $[ms^{-1}]$
U_A	wind speed $[ms^{-1}]$
U_a	current velocity at the top of the wave-current boundary layer $[ms^{-1}]$
$U_{b,w}$	bottom orbital velocity from waves $[ms^{-1}]$
U_c	total shear velocity for current case $[ms^{-1}]$
$U_{cr,b}$	critical velocity for bedload initiation $[ms^{-1}]$
$U_{cr,s}$	critical velocity for suspended load initiation $[ms^{-1}]$
U_{cw}	total shear velocity for combined case $[ms^{-1}]$
U_l	velocity in the x direction for layer l $[ms^{-1}]$
$U_{s,c}$	skin-friction velocity for current case $[ms^{-1}]$
$U_{s,cw}$	skin-friction velocity for combined case $[ms^{-1}]$
$U_{s,w}$	skin-friction velocity for wave case $[ms^{-1}]$

$U_{sb,cw}$	transport-related shear velocity for combined case $[ms^{-1}]$
$U_{se,cw}$	effective skin-friction shear velocity for combined case $[ms^{-1}]$
U_w	total shear velocity for wave case $[ms^{-1}]$
$U_{z,c}$	current velocity at height z from seabed $[ms^{-1}]$
V_l	velocity in the y direction for layer l $[ms^{-1}]$
W_l	velocity in the z direction for layer l $[ms^{-1}]$
$W_{s(i)}$	settling velocity of sediment class i $[ms^{-1}]$
WACC	Western Adriatic Coastal Current
WWW	Wave Watch III
III	
X	wind fetch [m]
Y	Yalin's parameter
ZSD	Secchi depth
Z_0	bed roughness [m]
$Z_{0,c}$	apparent bed roughness length [m]

Greek letters

γ_0	empirical sediment resuspension coefficient [-]
δ_{cw}	height of the wave-current boundary layer [m]
Δz	vertical distance between the centre of the last layer and Z_0 [m]
ϵ	sediment porosity [-]
η_i	availability of sediment class i at the bed [-]
ϑ_{cr}	Shield's parameter
ν	Kinematic viscosity of the seawater $[kgm^{-1}s^{-1}]$
ν_h	horizontal eddy viscosity $[m^2s^{-1}]$
ν_v	vertical eddy viscosity $[m^2s^{-1}]$
ρ_s	sediment grain density $[kgm^{-3}]$
ρ_w	water density $[kgm^{-3}]$
τ_*	normalized excess shear stress $[kgm^{-1}s^{-2}]$
τ_c	initial critical erosion stress $[kgm^{-1}s^{-2}]$
$\tau_{cr,b}$	critical shear stress for bedload initiation $[kgm^{-1}s^{-2}]$

$\tau_{s,c}$	skin-friction shear stress for current case$[kgm^{-1}s^{-2}]$
$\tau_{s,cw}$	skin-friction shear stress for combined case $[kgm^{-1}s^{-2}]$
ϕ_{100}	angle between wave and current direction at one meter from the seabed [rad]
ϕ_b	angle between wave and current direction at the top of the wave-current boundary layer [rad]
ϕ_m	model outputs
ϕ_o	observations
$\overline{\phi_m}$	model outputs mean
$\overline{\phi_o}$	observations mean
$\phi_{\sigma m}$	model outputs standard deviation
$\phi_{\sigma o}$	observations standard deviation
ω	wave angular frequency $[rads^{-1}]$

Chapter 1

Introduction

1.1 Climate change and coastal erosion

Coastal areas have always constituted a pivotal focal point on a global scale, given their importance in terms of higher population growth and urbanisation rates when compared with inland areas (Neumann et al., 2015). In addition to their resident population, these areas are significant tourist attractions during the warmer seasons of the year, especially regarding seaside activities. This dual function renders the need to combat beach erosion and maintain a stable coastline of paramount importance. (Kroon, 2016).

Globally, 163 coastal countries are facing erosion problems (Martínez et al., 2007) and, looking at sandy beaches only, 24% of the world's beaches are facing a reduction in width. The complex dynamics of beach erosion and accretion are intricately linked to natural processes and human activities, as highlighted by numerous studies (see Luijendijk et al. (2018)). For instance, a natural process affecting coastlines is the gradual subsidence of delta regions due to secondary consolidation (Bezzi et al., 2021). Conversely, anthropogenic activities, such as river damming, afforestation, or riverbed mining, can lead to a decrease in sediment loading in rivers (Syvitski et al., 2005). The ability to predict coastal evolution over time, and to identify the primary causes, remains a challenging endeavour, and there is currently no precise instrument available for this purpose.

Numerical models are regarded as a solution to this issue; however, there is still no development of a model that can be applied to various coastal settings, adequately tested, and extensively accepted, and, importantly, readily available (Warner et al., 2008). Nevertheless, local applica-

tions of numerical models are used to study sediment transport processes, since these models can help in understanding the key issues affecting the coast and can be a relevant instrument for producing management plans (Filipponi et al., 2015). In addition to the current state of coastlines, great interest is now being given to the changes that will happen with climate change (CC). Specifically, it is anticipated that CC will lead to alterations in environmental forcings, particularly wind and precipitation, which in turn will affect sediment transport processes. Consequently, it is imperative to estimate the projected effects of CC scenarios on coastal processes to formulate robust approaches to coastal management (Bonaldo et al., 2015). Indeed, as asserted by Zhu et al. (2021), human interventions tend to influence only the short term, while atmospheric forcings exert an effect over the long term. This underscores the necessity for a robust numerical model and CC scenarios to facilitate the adaption of a well-prepared management plan.

1.2 Study Area

The geographical area selected for the present thesis is the Emilia-Romagna coastline. Emilia-Romagna, a region in North Italy, is renowned for its erosion, as highlighted by the works of Alessandri (2022), and its significance for the regional economy, as highlighted by Cilli et al. (2021). Another notable geographical feature of the region is the Po River, which traverses its northernmost extent. The Po River is the longest in Italy (691 km long) and the main source of freshwater to the Adriatic Sea, with a mean discharge rate of 1500-1700 $m^3 s^{-1}$ (Wang and Pinardi, 2002; Wang et al., 2007).

The Adriatic Sea is an enclosed basin of the Mediterranean Sea, extending approximately 200 x 800 km (width x length) (Wang et al., 2007), located between Italy and the Balkan Peninsula. The basin can be divided into three distinct areas: a northern shallow area (depth $<$ 100 m) with a gentle slope (about 0.02°) (Filipponi et al., 2015); a middle area where depressions reaching 250 m of depth are present; and a southern deep area, reaching depths of 1200 m, that connects the Adriatic to the Mediterranean Sea with the Otranto Straight (Harris et al., 2008). The Western coast is distinguished by its gently sloping, smooth inclines, in contrast to the precipitous and uneven terrain of the opposing coastline, which is characterised by a plethora of islands and channels (Simoncelli, 2010). An overview of the Adriatic Sea bathymetry and

the three areas just described are given in figure 1.1.

Two primary wind regimes have been identified as crucial factors in shaping the Adriatic Sea's circulation. The first is the cold and favourable downwelling Bora wind, which originates from the north-eastern direction (Cavaleri and Bertotti, 1997). The second is the warm and favourable upwelling Scirocco wind, which originates from the south-eastern direction (Wang et al., 2007). As posited by Sedrati et al. (2011), the former wind forcing exhibits stronger events, especially during the winter period. Conversely, the latter events are more frequent, albeit with lower intensities.

It is widely acknowledged that winds and freshwater inputs represent two of the primary forcings for the basin circulation, with the third forcing being attributed to the tidal waves originating from the Mediterranean Sea (Orlic et al., 1992). The basin circulation exhibits a cyclonic pattern, characterised by the presence of three distinct surface gyres, each situated in the designated areas illustrated in figure 1.1. These gyres demonstrate a high degree of seasonal dependency, as highlighted by Guarnieri-Minnucci (2011). In addition to the surface circulation, two cyclonic gyres can be identified in deeper areas, located in the middle and southern Adriatic Sea (Artegiani et al., 1998). Two notable features of the basin circulation are the two

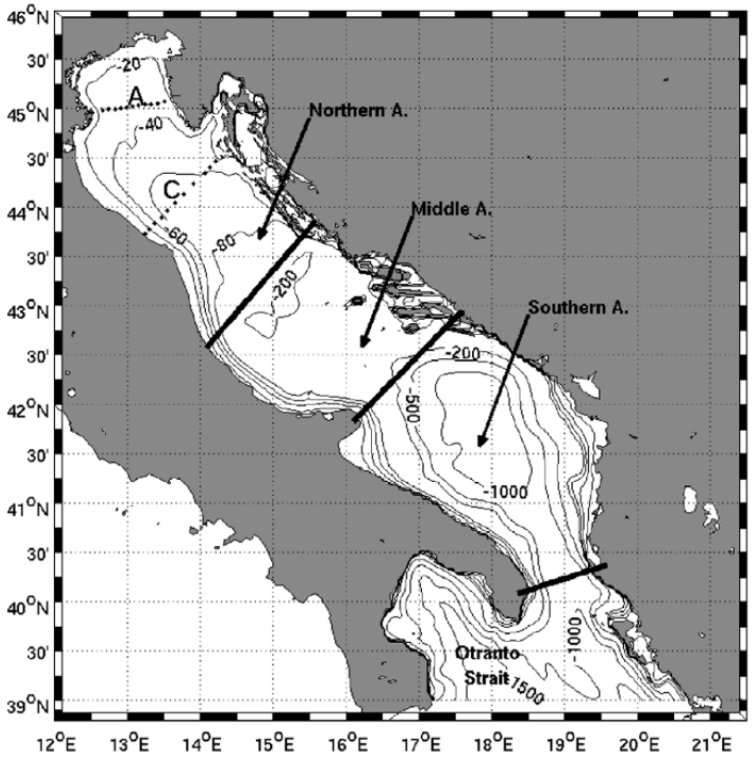

Figure 1.1: Adriatic Sea bathymetry and subsequent division of the basin into three areas. Source: Oddo et al. (2005)

coastal currents present on the eastern and western boundaries, respectively directed towards the north and south. The former current is recognised as the Eastern Adriatic Coastal Current (EACC), while the latter is recognized as the Western Adriatic Coastal Current (WACC). Both these currents are a result of the thermohaline circulation in the basin, where the saltier waters of the south exchange with the freshwater of the north (Fain et al., 2007). An overview of the general surface circulation pattern of the Adriatic Sea is shown in figure 1.2. The seasonality of the basin pattern is characterised by alterations in two of its forcings throughout the year. A study of river discharges reveals that high discharges are recorded during spring and autumn, respectively, due to snowmelt processes and increased precipitation on land (Cattaneo et al., 2003). Conversely, winds tend to be stronger during the winter period, with Bora events (e.g. Unguendoli et al. (2023)). Overall, some of the main seasonal responses are the change of the WACC position, which tends to get stronger and closer to the coast during the winter, and the Northern gyre variability (Alessandri, 2022).

As previously stated, the geographical area under investigation in this study is the Emilia-Romagna coast, located in the northern section of the Adriatic Sea. The region is recognised as microtidal, with tides ranging between 80-90 cm for spring and between 30-40 cm for neap (Harley et al., 2012) and with a low energy wave field, since significant wave heights are gen-

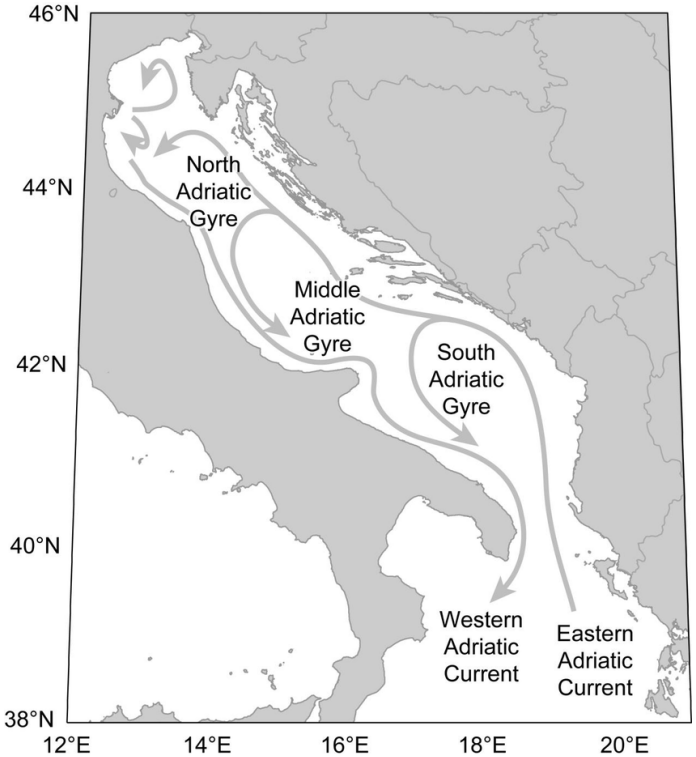

Figure 1.2: Surface circulation pattern of the Adriatic Sea. Source: Melià et al. (2016)

erally (91%) lower than 1.25 m (Ciavola et al., 2007). Another important forcing to consider along the coastline is the natural subsidence rate, which has reached values of 2.5-7.5 $mmyr^{-1}$ (Bitelli et al., 2020). Overall, the coastline is already facing erosion problems, that are only expected to increase over time due to CC conditions (Gallina et al., 2019). To address this issue, various coastal defences have been installed along the shoreline, including breakwaters, jetties, groins, and sea walls. Additionally, when feasible, sand nourishments are applied to enhance the shoreline's resilience (Alessandri, 2022).

To overcome the erosion, more knowledge of the processes affecting sediment transport in the area is needed. The subsequent chapter proffers an overview of the extant literature pertaining to sediment transport in the study area, thereby furnishing the reader with a generalised understanding of the subject.

1.3 Sediment transport literature

The Po River is the primary single source of sediments in the Northern Adriatic Sea, as evidenced by recent studies (Filipponi et al., 2015). Specifically, the sediment load of the Po River was augmented by the diversion of Porto Viro, a project executed by Venetian engineers at the inception of the 17^{th} century, as documented by Simeoni and Corbau (2009). This diversion was undertaken to prevent the infilling of sediments in the Venetian lagoon. This resulted in rapid seaward growth of the river delta (Bondesan, 1990). The subsequent evolution of the Delta is illustrated in figure 1.3. At the time of the diversion, the most efficient branch was the Po di Maistra, as reported by Ciabatti (1967). However, following the 1872 flooding, the Po di Maistra began to lose importance, with the Pila branch becoming the primary distributary (Friedrichs and Scully, 2007). The Po River's sediment loading has undergone a substantial decline in recent decades, particularly over the past fifty years, as highlighted by studies such as Cencini (1998) and Stefani and Vincenzi (2005) research, which focused on granular sediments. Simeoni et al. (1997) reported a decrease in solid discharge from 12.8 $Mtyr^{-1}$ (1918-1943) to 4.7 $Mtyr^{-1}$ (1986-1991). This trend is also reflected by the data collected by Arpae on solid discharge, from 2011 to 2019. Specifically, figure 1.4 illustrates the annual sediment yields for the Po River, calculated from the daily turbidity values collected by Arpae at the Pontelagoscuro station. The primary factor contributing to this decline in sediment supply is considered to

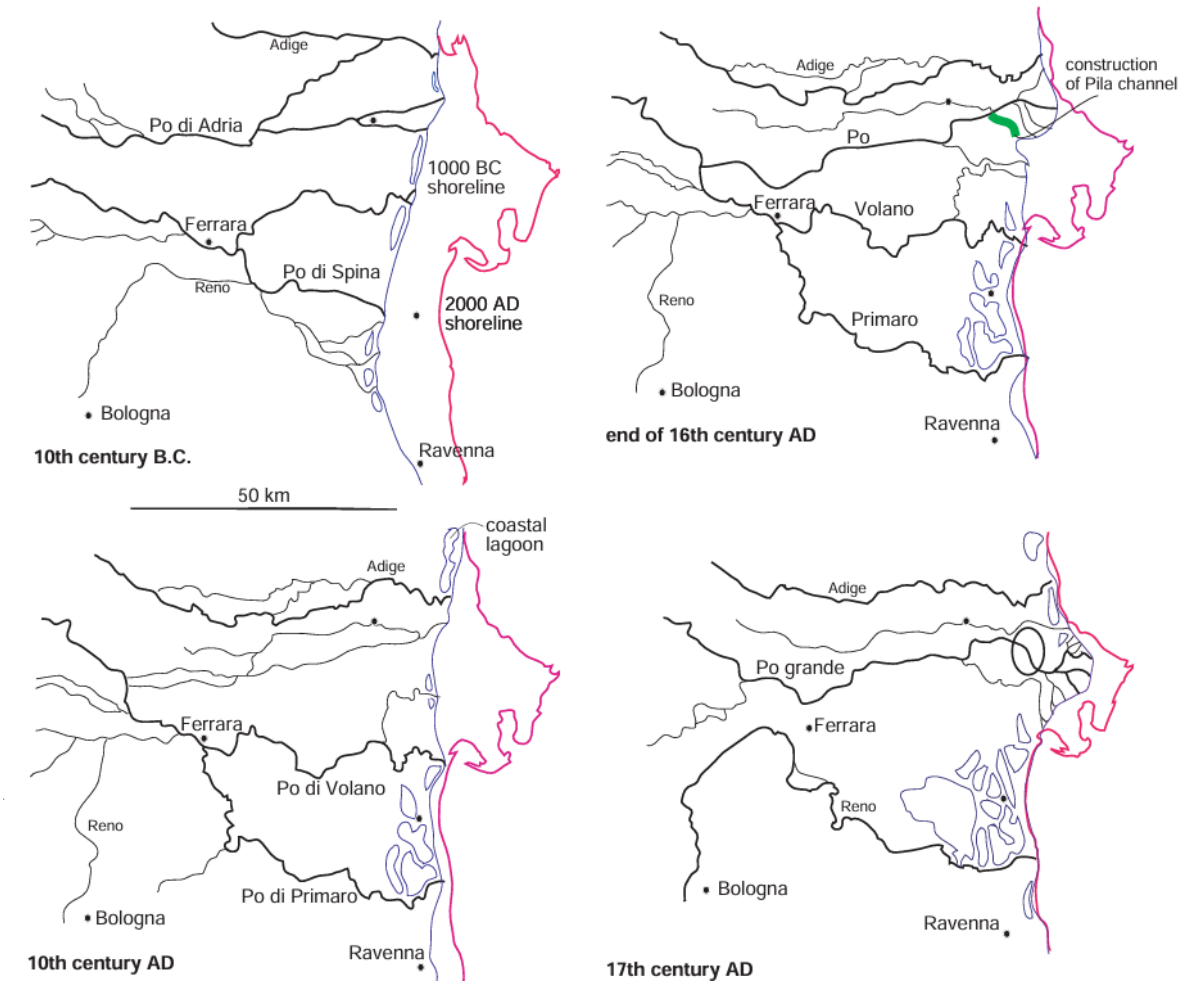

Figure 1.3: Evolution of the river channels and shoreline over time.
Source: Syvitski et al. (2005)

be anthropogenic interventions, both in the immediate vicinity of the riverbed (e.g. riverbed mining, dam construction (Cilli et al., 2018)) and in adjacent regions (e.g. changes in land use, afforestation (Billi and Spalevic, 2022)). For instance, Italy has witnessed a notable expansion of forested areas in recent years, reaching approximately 40% of its total territory (Marchetti et al., 2018), which has consequently led to a decline in the erosion of the land and, by extension, a decrease in the sediment yield of the rivers.

In addition to the Po River, the study area encompasses Apennine rivers that have been classified by Milliman and Syvitski (1992) as small mountainous rivers. These rivers supply most sediments to the coast, but only when considered collectively (Harris et al., 2008). Specifically, the estimation by Cattaneo et al. (2003) suggests that the discharge of 15 $Mtyr^{-1}$ of sediments to the coast by the Po River is accompanied by a combined discharge of 32 $Mtyr^{-1}$ from Apennine rivers. This indicates a twofold increase in sediment input to the Adriatic Sea. This finding underscores the significance of these rivers in terms of sediment input into the Adriatic

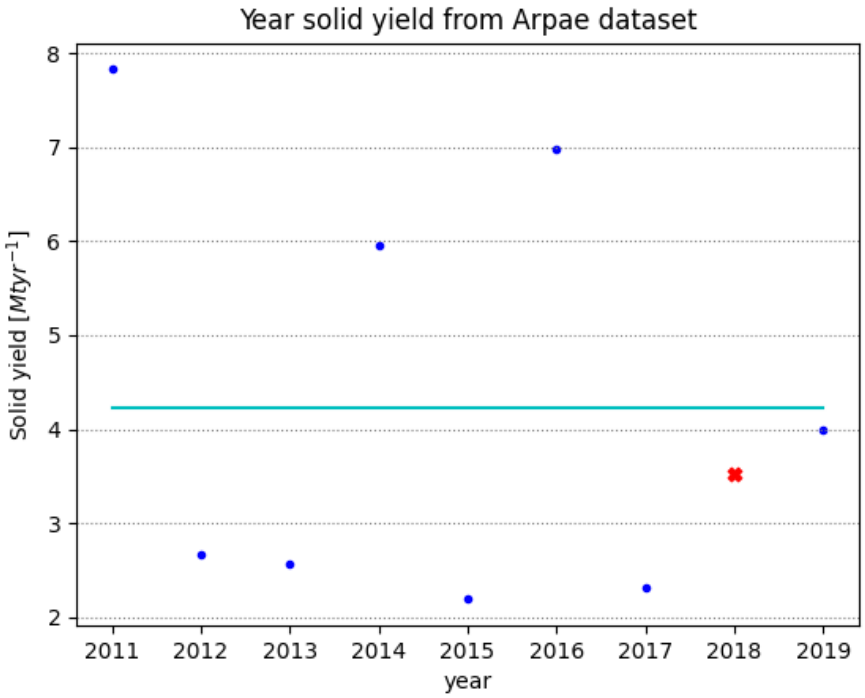

Figure 1.4: Solid yearly yield [$Mtyr^{-1}$] of the Po River, calculated using the Arpae turbidity dataset at Pontelagoscuro station. A red cross is used to represent the yield calculated for 2018 because that year does not have a complete time series of measurements; the cyan line shows the calculated mean sediment yield (4.23 $Mtyr^{-1}$).

Sea (Syvitski and Kettner, 2007; Cilli et al., 2021). In the contemporary era, these waterways are subjected to stringent regulation, with the implementation of sluice gates to modulate their flow. This, in turn, has a concomitant effect on the sediment yield, es evinced by Cilli et al. (2020).

The sediments supplied by these rivers are fine-grained and are categorised as silt and clay (Brambati et al., 1973). The sedimentation pattern of these newly introduced sediments follows exactly the hydrodynamic circulation, as demonstrated in the study by Alvisi et al. (2019). Of particular note is the presence of a substantial mud belt at intermediate depths, characterised by its elongated, shore-parallel orientation, extending to the Gargano Delta (Puig et al., 2007). The fine sediments, introduced by the Po and the Apennine rivers (Amorosi et al., 2022), are trapped near the Western Adriatic coast by the WACC (Pellegrini et al., 2021) and settle to form the mud belt. This sedimentation pattern is further substantiated by the seabed substrate map provided by EMODnet, which categorises seven distinct sediment classes (Folk 7), as depicted in figure 1.5. The map clearly delineates the mud belt that extends itself from the Po River Delta in a shore parallel pattern, with coarser classes present on both sides of the

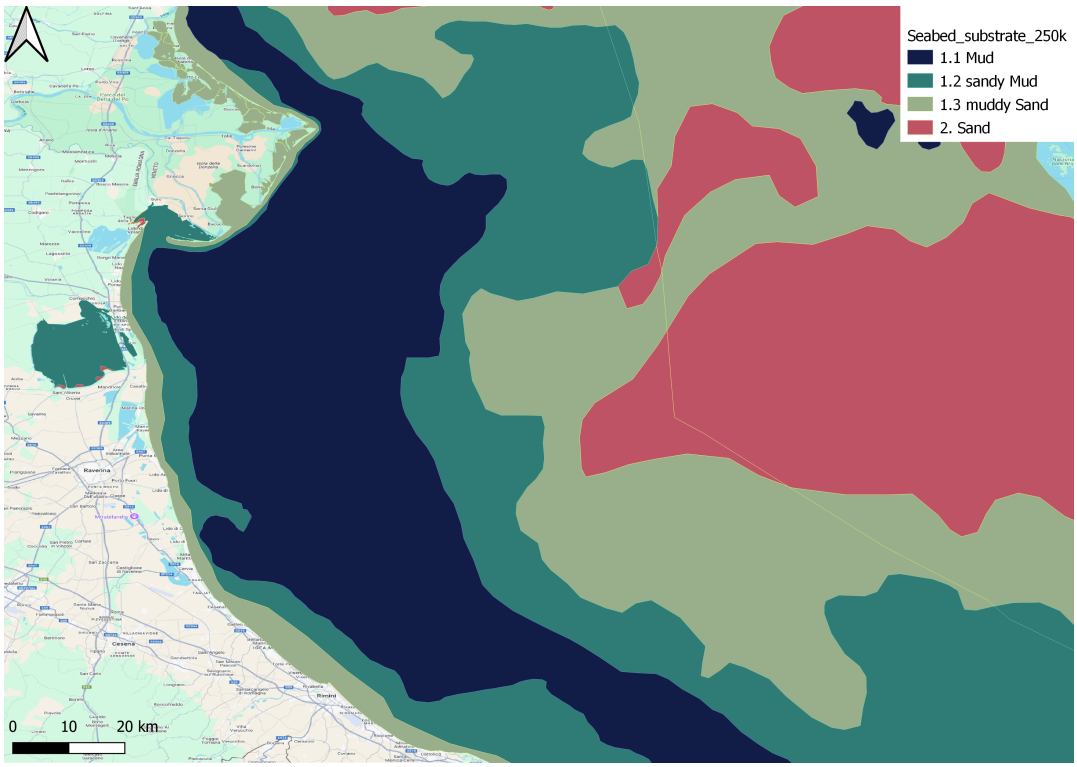

Figure 1.5: Seabed substrate data for the study area. Dataset: Seabed_substraate_250k with 7 substrate classes (Folk 7), offered by EMODnet.

belt. Out of the seven sediment classes used for the EMODnet dataset, only four are present in the study area: mud, sandy mud, muddy sand, and sand. Utilising the Udden-Wentworth grain-size scale, a widely adopted scale that provides comprehensive descriptions of the fractions of sand and mud (Blair and McPherson, 1999), the respective grain size ranges for each class are as follows:

Mud: 2 - 63 μm (mean value: 32.5 μm)

Sandy mud: 63 - 125 μm (mean value: 94 μm)

Muddy sand: 125 - 250 μm (mean value: 187 μm)

Sand: 250 - 500 μm (mean value: 375 μm)

It has been determined that the Pro delta of the Po River is the location of the most significant sedimentation, particularly in the vicinity of the Pila mouth (Palinkas and Nittrouer, 2007; Harris et al., 2008). During flood events, secondary distributaries are also expected to become more active, contributing to an increase in sedimentation within the area (Wheatcroft et al., 2006). The Pro delta, formed by these settlements, is skewed towards the south, reflecting

the prevalent sediment dispersal pattern (Bosman et al., 2020). While most sediments remain within a 15 km radius of the Po River mouths, as highlighted by Bever et al. (2009), another depositional hotspot has been identified in front of Ancona, particularly for non-flocculated and low-settling materials, as noted by Wang et al. (2007). Notwithstanding the sedimentation occurring within the Po River area, the Delta is confronted with significant issues of subsidence, attributable to secondary consolidation. This area has one of the highest relative sea level rise rates of the area (Corbau et al., 2022).

The phenomenon of land subsidence is widely regarded as a primary contributing factor to the coastal erosion observed in the designated study area. Contemporary river sediment loading does not counterbalance the subsidence rates observed in the region (Bezzi et al., 2021). Another crucial element for coastal erosion is the decrease of sediment loading by rivers. The predominant source of sediments on beaches is the erosion of sediments from adjacent areas (Simeoni and Corbau, 2009). The final recognised agent for coastal erosion is the decrease in sediment grain sizes transported from rivers, since the granular transport has stopped, and the median diameter of the transported sediments goes from 13.5 μm to 216.12 μm (Bosman et al., 2020).

It is imperative to recognise that the erosion has a detrimental effect on both the population and the economy of the area. To devise management plans that can reduce or halt the erosion, it is essential to develop a more profound understanding of the processes involved. A potential solution is to utilize numerical models, which have increasingly been recognized as management tools to describe marine processes and their environments in recent years (Umgiesser et al., 2022).

1.3.1 Numerical models for sediment transport in the northern Adriatic

The following section provides an overview of the numerical models that have been employed to investigate sediment transport in the study area. In addition, the concluding results of each application are presented.

The first model application presented is that offered by Wang and Pinardi (2002). The grid utilised in this study encompasses the entire Adriatic Sea, showing an irregular spacing, with

resolutions ranging from 10 km at the Otranto Straight to 3 km in the Northern Adriatic, encompassing 21 sigma coordinate vertical levels, as outlined by Zavatarelli et al. (2002). The hydrodynamic model employed is the three-dimensional Princeton Ocean Model (POM) (Blumberg and Mellor, 1987). This model has been coupled with a sediment transport model. The sediment transport model is analogous to the one proposed by Ribbe and Holloway (2001) for the Australian Northwest shelf. It operates under the assumption that all sediment classes are non-cohesive, thereby precluding flocculation or aggregation. The model utilises two distinct sediment classes: a coarse class, comprising grains with a diameter greater than 50 μm, and a finer class, comprising grains with a diameter less than 50 μm. The settling velocity of each class is calculated using Stokes law, and the sediment density is set at 1100 kgm^{-3}. The two major findings that emerge from this application are as follows: firstly, wave resuspension cannot be disregarded in the shallow western shore of the Northern Adriatic Sea; and secondly, vertical mixing of wave-resuspended sediments is prevented by plume-induced stratification.

The second study is based on the findings of the previous study and is offered by Wang et al. (2007). The grid previously utilised has undergone an update, being transformed into a regular grid with a 5 km resolution encompassing the entire Adriatic Sea (see reference Zavatarelli and Pinardi (2003)). The vertical dimension continues to employ 21 sigma levels. With regards to the numerical models employed in the simulations, the only update has been the coupling with a third-generation wave model, SWAN. The simulations performed in this study are forced with realistic wind stress, surface heat flux, and river runoffs. However, due to the unavailability of data for comparing model results, the conclusions given are only of explanatory nature. The most significant finding is that tides do not influence sedimentation.

The third model application is presented in Harris et al. (2008), which uses the Regional Ocean Modelling System (ROMS) for the hydrodynamics and sediment transport, and SWAN to estimate the wave fields. The configuration utilises a regular grid with a 3 km resolution, encompassing the entire Adriatic Sea, and 20 vertical s-coordinate levels. The wind and heat flux forcing are taken from COAMPS, while the fluvial discharges are taken from measurements, where available, and monthly mean climatologies. Solid loading was imposed at the Po and Apennine rivers using estimates provided by HYDROTREND (Kettner and Syvitski, 2008). The present study investigates six distinct grain sizes, ranging from clays and sands to floccu-

lated particles, all with a constant density of 2650 kgm^{-3}. An initial sediment distribution was applied, based on observations. As Harris et al. (2008) have demonstrated, the redistribution of sediment is contingent on its inherent properties (e.g. settling velocity and critical shear stress) in conjunction with prevailing oceanographic conditions.

The fourth study of sediment transport was conducted by Bever et al. (2009) and employed the same models and configuration as Harris et al. (2008), apart from an updated grid. The grid utilised in this study is of an orthogonal curvilinear nature, with enhanced horizontal resolution in the Po Delta area (750 m) and 20 stretched terrain following vertical levels. The second update applied to this implementation, following the increased resolution at the Po River Delta, is the division of the Po River discharge into the different mouths, using estimates from Nelson (1970). The third and final adjustment to the model setup involves a reduction in the number of sediment classes from six to five, with three classes present at the seabed (0.063, 0.125, and 0.225 μm) and two classes forced at the Po River (0.015 and 0.063 μm). This model setup has enabled the identification of two key findings. The first finding indicates that during flood periods, the buoyant plume plays a significant role in sediment transport and exerts an influence on the deposition of the Po River subaqueous delta. The second finding demonstrates that transport rates and pathways are predominantly influenced by wave action and current direction.

The fifth and final published work addressing the modelling of sediment transport in the study area is that of Sherwood et al. (2015). The setup utilised in this publication is identical to that employed in the aforementioned work by Harris et al. (2008), with the sole difference being the use of a regular grid with a 4 km resolution for ROMS and a 2 km resolution grid for SWAN. The autors' conclusion is that southward transport will prevail, irrespective of the timing or mechanism of sediment resuspension.

The unpublished work of Guarnieri et al. (2014) is here presented. The numerical models employed in this study are identical to those utilised in Wang et al. (2007), namely POM for hydrodynamics and SWAN for waves, with a regular grid comprising a horizontal resolution of 1/45° and 31 sigma levels in the vertical dimension. Two distinct classes of sediments are considered: a coarse class, characterised by a grain size of 55 μm and a settling velocity of 10^{-4} $[ms^{-1}]$, and a fine class, distinguished by a grain size of 17 μm and a settling velocity of 10^{-5}

$[ms^{-1}]$. The settling velocities are calculated using Stokes law, and both classes use a sediment density of 1800 kgm^{-3}. As a lateral boundary condition for sediments at the Po River mouth, a constant flux of 450 kgs^{-1} is applied, while for other rivers the constant flux is of approximately 6.50 kgs^{-1}. During periods of flooding in the Po River, a parametric estimation of the solid discharge is employed, which is assumed to be linearly dependent on the liquid discharge. The estimation is formulated as follows:

$$\begin{cases} Q_s = \frac{Q_w}{12000} & \text{for } Q_w \leq 3500 \\ Q_s = \frac{Q_w}{5500} & \text{for } Q_w > 3500 \end{cases} \tag{1.1}$$

where Q_s and Q_w $[m^3s^{-1}]$ represents the flows of solid and liquid materials, respectively. The study yielded several notable conclusions. Firstly, the sediment characterisation employed in this study lacked the requisite accuracy. Secondly, the critical shear stress for erosion was found to vary both temporally and geographically, a factor that must be considered in future studies. Thirdly, the active layer at the seabed was found to have a variable thickness.

In conclusion, it should be noted that none of the proposed numerical models were intended to serve as an operational tool for sediment transport modelling; however, they all concentrated on understanding the processes affecting this specific subject and provided a comprehensive overview of the main processes that should be considered and the main patterns that should be represented by a sediment transport model of the area.

1.4 Aim of the project

In light of the preceding sections, two conclusions can be drawn. Firstly, erosion constitutes a significant problem, and it is anticipated to intensify under CC conditions. Secondly, there is a clear necessity for adequate tools to study and predict this process.

This project's objective is to design the first sediment transport model of the Emilia-Romagna coastline, utilising a finite-element model and multiple sediment classes. The significance of these characteristics is underscored by the fact that no existing model has employed grids with variable resolution and four classes of sediments. Achieving this objective is challenging, as sediment transport models are required to elucidate intricate processes that are yet to be fully

comprehended, whilst concurrently addressing phenomena across a broad spectrum of spatial and temporal scales (Amoudry and Souza, 2011). In addition, this project provides an overview of the available datasets for suspended sediments in the study area.

For the purposes of this thesis, it has been decided to use SHYFEM-MPI with the sediment module. The underlying rationale for this choice is that the work of Alessandri (2022) provides an unstructured grid of the study area, already calibrated, and validated in SHYFEM-MPI for the hydrodynamic parameters. The grid has been designed to be computationally reasonable, even having an increased resolution at the coast. This latter feature is of primary importance, given that the sediment module offered by SHYFEM-MPI has not yet been parallelised, and thus the model is run in sequential mode.

The designed model is then compared with the depositional arrangement at the sea bottom and the erosion deposition patterns recorded along the Emilia-Romagna coastline. The depositional distribution of the model should resemble the one shown in figure 1.5, while the erosion deposition patterns should follow the rates of figure 1.6. The latter figure displays shoreline erosion and accretion rates, measured by satellite images for sandy beaches. These rates were

Figure 1.6: Shoreline erosion (red) and deposition (green) rates are presented, calculated over the period 1984-2016, using shoreline positions from satellite data, with transects of 500m. This dataset is offered by Deltares, and the global analysis results are presented in Luijendijk et al. (2018).

calculated by Luijendijk et al. (2018) over a period of thirty years, and the map only shows the results calculated for the Po Delta region. Consequently, three research questions have been identified for this thesis:

1. Does SHYFEM-MPI have the capacity to adequately represent the observed suspended sediment concentration patterns along the coast? Does the plume geometry and evolution resemble the observed patterns?

2. Can the model reproduce the depositional pattern of the study area? Is the mud belt surrounded by coarser sediments?

3. Can the model reproduce the recorded erosion deposition patterns? Can the model represent the erosion in the Po di Goro area and in front of Ravenna? Can the model represent the deposition present at the Goro lagoon?

The coming chapters are organised as follows: chapter two offers an overview of the numerical model used, with particular attention to the sediment transport part and the different forcings; chapter three is dedicated to the sensitivity analysis and to the decision of the best model set up; in chapter four, the results of the one-year simulation are presented; the discussion of the final results is given in chapter five and, lastly, chapter six summarizes the main results of this thesis and also gives inputs for future steps.

Chapter 2

Model description

The primary goal of this research is to define a numerical model capable of representing the sediment transport along the Emilia-Romagna coastline, with particular attention to the distribution pattern of the sediment load of the River Po. To describe the sediment transport, the resolution of the model at the coast should be as fine as possible to represent the detailed geometry of the coastline (Maicu et al., 2021), but the resolution at the open boundary or in the deeper areas can be coarser. This type of grid (changing resolution from coarser to finer in the areas of interest) is used to reduce computational effort compared to a grid with a constant high resolution throughout the domain. To seamlessly resolve different spatial scales, an unstructured (or variable) grid model is recommended. As already mentioned in chapter 1.4, for this research it was decided to use SHYFEM-MPI (System of HYdrodynamic Finite Element Modules), which works on unstructured grids with triangular elements and uses the finite element method to solve the equation of motion.

2.1 Description of SHYFEM-MPI ocean model

The model was initially developed by ISMAR-CNR (Umgiesser et al., 2004) and based on Umgiesser (1986). However, the version of the model used in this thesis is SHYFEM-MPI, developed by Centro Euro-Mediterraneo sui Cambiamenti Climatici (CMCC) (Micaletto et al., 2021). The model resolves the primitive hydrodynamic equations using two assumptions: the hydrostatic approximation, and the Boussinesq approximation. The former assumes that the pressure at any point in the domain is given by the weight of the water that is above that point

($p = \rho_w g z$), while the latter assumes that there is no density differences in the fluid, since the differences are expected to be small and so negligible, except when the terms are multiplied by the gravity acceleration. The Boussinesq approximation is instrumental in deriving the assumption that water is incompressible. The use of these approximations is instrumental in simplifying the equations, thereby facilitating their nonlinearity. The domain is discretised in a staggered manner, employing an Arakawa B grid, wherein the scalar quantities are defined at the nodes and the vectors are centred within the elements. Conversely, the vertical dimension is discretised with z levels, which is the only vertical discretization offered by SHYFEM (Umgiesser et al., 2006).

Alessandri (2022) has previously employed SHYFEM-MPI to investigate the hydrodynamics of the Emilia-Romagna coastline and the Goro Lagoon. For the two distinct areas, two different grids were utilised: ShyfER and GOLFEM grids, respectively. The former grid possesses a resolution of 2.2 km at the open boundary, which subsequently increases to a resolution of 300 m along the coast. In contrast, the latter varies from 2.2 km to 10 m within the lagoon's channels.

In view of the favourable outcomes attained by Alessandri (2022) with the ShyfER grid in relation to the hydrodynamics of the study area, it was determined that the utilisation of the

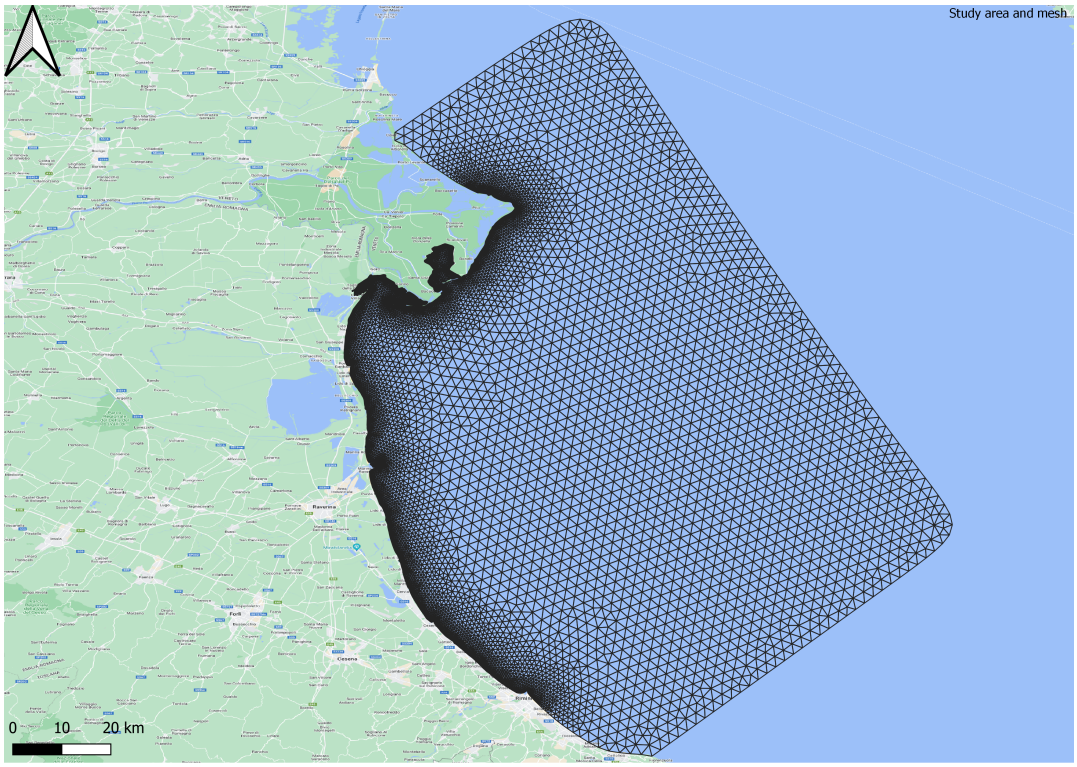

Figure 2.1: ShyfER unstructured grid. Source: Alessandri (2022)

aforementioned grid would be appropriate for the present research. The configuration of this grid is illustrated in figure 2.1 and it possesses 8148 nodes that are utilised to generate 15392 elements. In addition to the grid, the parameterization for the hydrodynamic component of the model and the generation methods for the initial and boundary conditions were also adopted. Alessandri (2022) conducted a sensitivity analysis for several parameters, determining the optimal combination through a comprehensive evaluation of currents, salinity, and temperature. A notable parameter that underwent rigorous testing is the horizontal turbulent diffusion coefficient of tracers, K_h. This analysis yielded a value of 0.2 $m^2 s^{-1}$. This coefficient is distinct from the horizontal eddy viscosity, denoted by ν_h $[m^2 s^{-1}]$, which is employed in the horizontal momentum equations and is calculated using the Smagorinsky formulation (Smagorinsky, 1963). Conversely, the vertical eddy viscosity, ν_v, is derived from the GOTM turbulence model (see Burchard et al. (1999)) and has been integrated within the SHYFEM-MPI framework. An example of the input file for SHYFEM-MPI is provided in Appendix A. The validation of the final setup of Alessandri (2022) is illustrated in figure 2.2, where the model results are compared with the measurements carried out at Porto Garibaldi station for salinity (a), temperature (b),

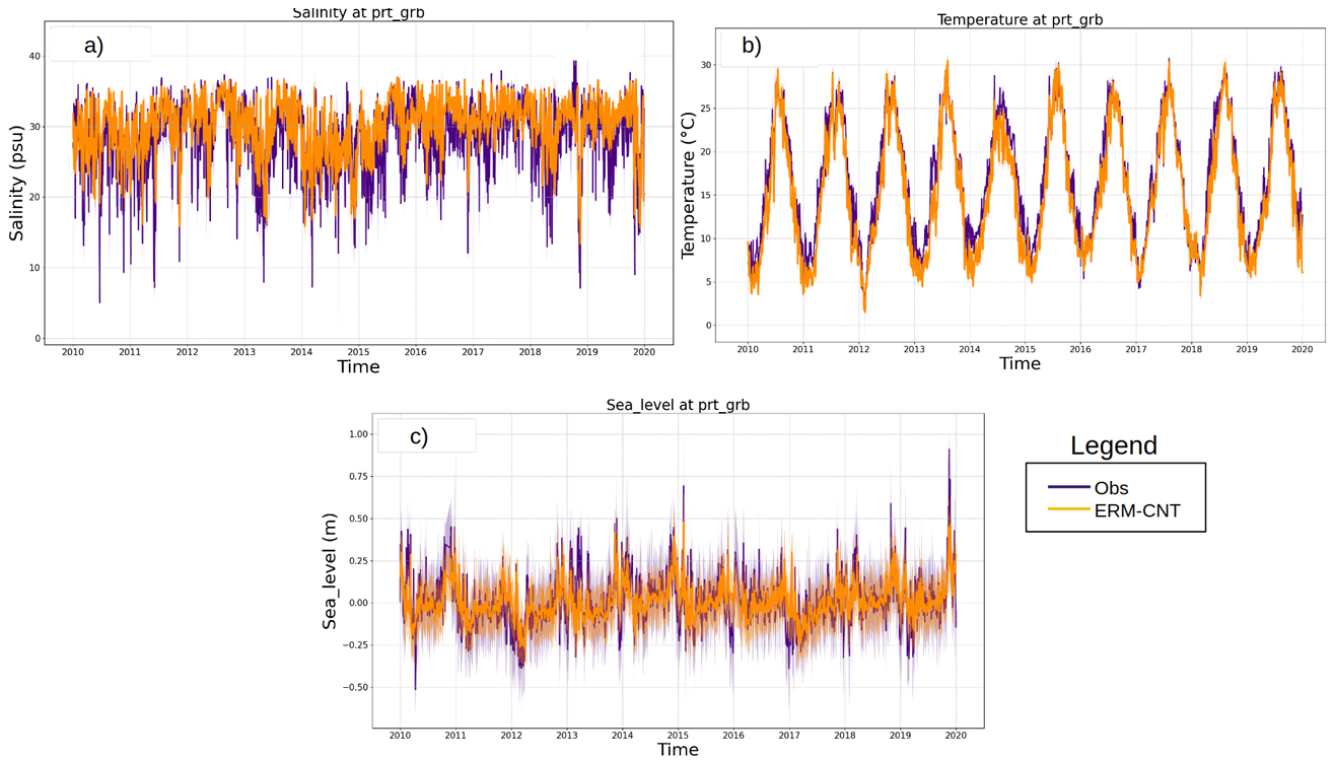

Figure 2.2: Validation of the ShyfER grid with the final model setup. A comparison was made between the daily values of the model (purple) and observations at Porto Garibaldi (orange) for salinity (a), temperature (b), and sea level (c). Source: Alessandri (2022)

and sea level (c). It is noteworthy that the same grid and parametrization of the model has been employed by Pillai et al. (2022).

The ShyfER grid has been updated to incorporate the latest bathymetric data, which was obtained for the CASCADE project, in which Arpae participated. Specifically, the updated bathymetry utilises the data from EMODnet 2020, with a resolution of 115 m, for the deeper areas, while for coastal regions, the multibeam surveys conducted by Arpae in 2018, along various transects of the Emilia-Romagna coastline, with additional measurements obtained in the Goro lagoon in 2022, are employed. Another reason why the bathymetry used for this project has been updated is that the grid used in Alessandri (2022) and Pillai et al. (2022) was made with a minimum depth value of 1.5 m; since their project aimed at an offline coupling with the spectral wave model Wave Watch III (WWIII) (Group, 2016). However, the coupling with a third-generation wave model is not considered in this thesis.

With the changes to the bathymetry, the vertical levels used also had to be varied. In particular, Alessandri (2022) utilised a first vertical level with a thickness of one meter, whereas in the present study, the surface level is one and a half meter thick. This increased depth of the initial z layer is necessary because, otherwise, some open boundary nodes dried out, resulting in an error that terminated the simulation. The updated surface level employed in this thesis is consistent with that utilised by Arpae in their operational SHYFEM model. The updated bathymetry is displayed in figure 2.3 and the colormap employed utilises the same intervals as the z levels considered. Specifically, the vertical levels ranging from a depth of two metres to ten metres exhibit a thickness of one meter, while the interval from ten metres to the total depth of 56 meters is characterised by a thickness of two metres.

SHYFEM-MPI provides a suite of modules that can be integrated into the hydrodynamic framework. One such module is utilised for the calculation of sediment transport, thereby rendering this model an appropriate tool for the present research. A more detailed description of the module and its associated equations can be found in the subsequent section.

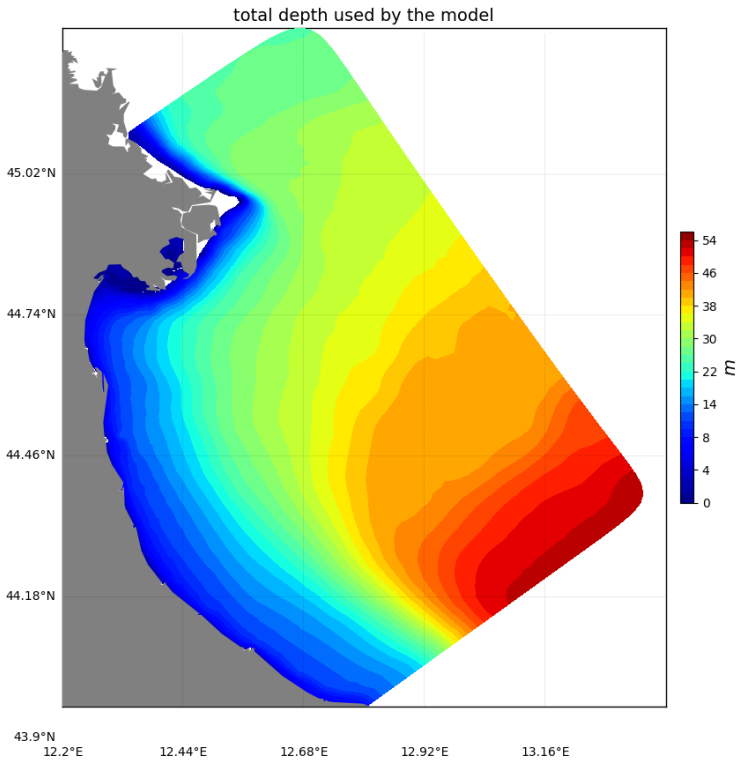

Figure 2.3: Updated bathymetry for the ShyfER grid. The colormap has been discretized according to the vertical levels employed by the model configuration.

2.1.1 Surface and lateral boundary condition for the circulation model

As previously stated, the initial and lateral boundary conditions for the hydrodynamics are generated using the same approach as in Alessandri (2022).

In the following subsections, a concise description of the forcings utilised for the circulation model is provided, along with information on the data set employed to generate them.

Surface forcings - Atmosphere

All the atmospheric boundary conditions are sourced from ECMWF. Specifically, the deterministic, high-resolution model from ECMWF at global scale was employed (ECMWF-IFS (Owens and Hewson, 2018)). The resolution of the data set is 12.5 km, and the analysis frequency is six hours. To correct the model results with the observations, the model uses a 4DVAR assimilation scheme.

The following variables are used for forcing the circulation model under investigation in this thesis:

- wind velocity in the x and y directions [ms^{-1}];
- mean sea level pressure [Pa];
- solar radiation [Wm^{-2}];
- air temperature [C°];
- dew point temperature [C°];
- cloud cover [-];
- precipitation [mmd^{-1}], with a negative value indicating evaporation

Open boundary conditions - Ocean circulation

The data set employed to generate the initial and boundary conditions is the Mediterranean Sea Physics Reanalysis, which is offered by the Copernicus Marine Environment Monitoring Service (CMEMS). Specifically, the product identifier in Copernicus is: MEDSEA_MULTIYEAR_PHY_006_004. The horizontal resolution of the grid is of 1/24°, while the vertical resolution is 141 levels, unevenly spaced (Lecci et al., 2022).
Four variables are extracted from the data set:

- Sea surface height (SSH) above the geoid (zos [m]), with an hourly mean field given in 2D (med-cmcc-ssh-rean-h);
- Eastward and northward sea water velocity (respectively uo and vo [ms^{-1}], offered as a 3D daily mean (med-cmcc-cur-rean-d)
- Salinity (so [psu]), as a 3D daily mean (med-cmcc-sal-rean-d)
- Potential temperature (T [C°]), as a 3D daily mean (med-cmcc-tem-rean-d)

These data sets are then used to generate the initial and boundary condition files for the model. The only variable that needs to be manipulated before use is the sea surface height. It should be noted that the MED-MFS SSH does not incorporate tides; therefore, it is necessary to determine and incorporate them into the downloaded data. In Alessandri (2022), tides are computed using the barotropic TPXO model (Egbert and Erofeeva, 2002), which is offered by

the Oregon State University, with a resolution of 1/30°. These tides are then added to the MED-MFS sea level data. The model incorporates eight tide components: K1, O1, P1, S1, K2, S2, M2 and N2.
The files that are then generated to force SHYFEM-MPI are:

- Initial condition for salinity
- Initial condition for temperature
- Initial condition for currents
- Boundary condition for sea level
- Boundary condition for salinity
- Boundary condition for temperature
- Boundary condition for currents

No initial condition of the sea level is given, since, looking at the kinetic energy, the domain requires only eight hours to reach an equilibrium state. Additionally, using an initial condition for sea level resulted in issues in running the model. The open boundary is specified as a level boundary, and it is subject to two distinct conditions for flux entry and exit: the Dirichlet condition and the Neumann condition, respectively. Furthermore, a nudging procedure is applied to the velocity condition, with a thirty-minutes nudging time (Alessandri, 2022).
Conversely, the closed boundary employs a full slip condition.

Lateral boundary - River discharge

The Emilia-Romagna coastline is characterised by a multitude of rivers, the overview of which is illustrated in figure 2.4. Of these, the Po River is distinguished by its deltaic feature, and this study encompasses the Po Delta along with all its outflows. An overview of the mouths utilised in the model configuration, along with their respective nomenclature, is presented in figure 2.5.

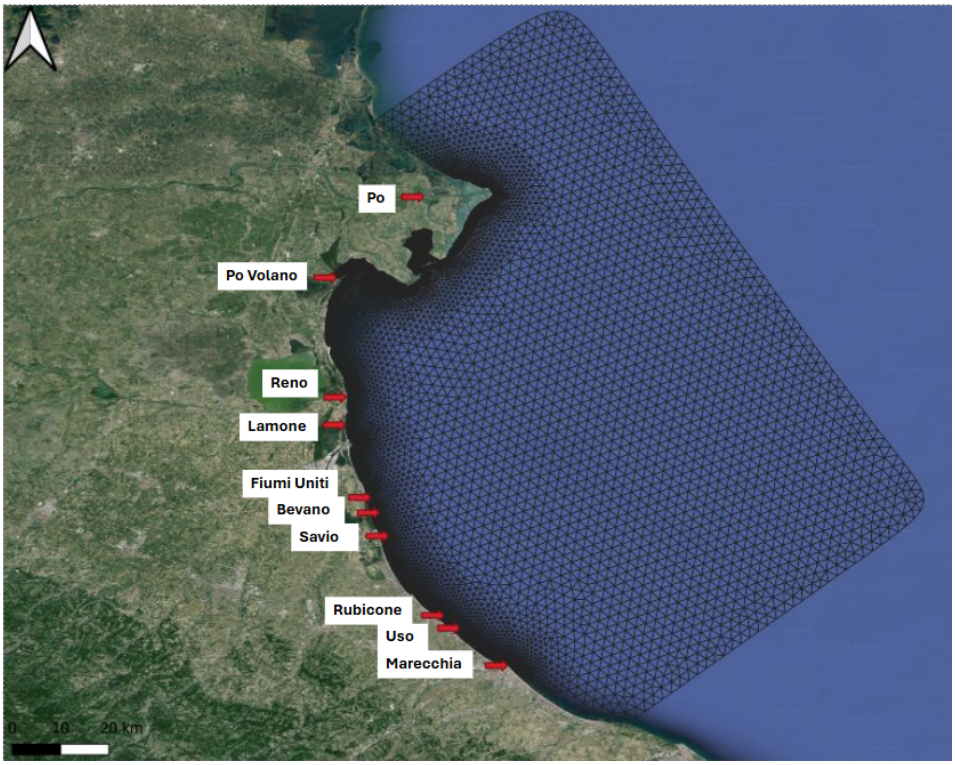

Figure 2.4: Map illustrating the various river mouths within the confines of the study area. All these rivers are considered to delineate the lateral boundaries.

Rivers are described as flux open boundaries, which are specified along the coastline. Specifically, they are represented as lateral surface open boundaries. For each flux boundary, parameters such as runoff, solid transport, temperature, and salinity can be specified (Maicu et al., 2021).

In Alessandri (2022)'s SHYFEM-MPI setup, the discharges forced at all the rivers depicted in figure 2.4, excluding the Po River, correspond to the monthly climatology determined by Raicich (1994). However, for the Po River, given the availability of a measuring station that provides daily mean discharges, the observed values are utilised. Regarding temperature, the monthly climatology of Raicich (1994) is utilised for all rivers. For salinity, a constant value of 15 psu is employed for all other rivers (Zavatarelli and Pinardi, 2003), while for all Po mouths depicted in figure 2.5, the constant salinity is set to 17 psu (Oddo et al., 2005). This configuration was also utilised by Verri et al. (2018) in their study of the Central Mediterranean Overturning Circulation (CMOC), as detailed in the text.

The data employed for the Po River discharge is derived from measurements collected at the Pontelagoscuro station. It should be noted that this station is one of several measuring stations situated along the river, but it is the closest to the delta and the point at which the

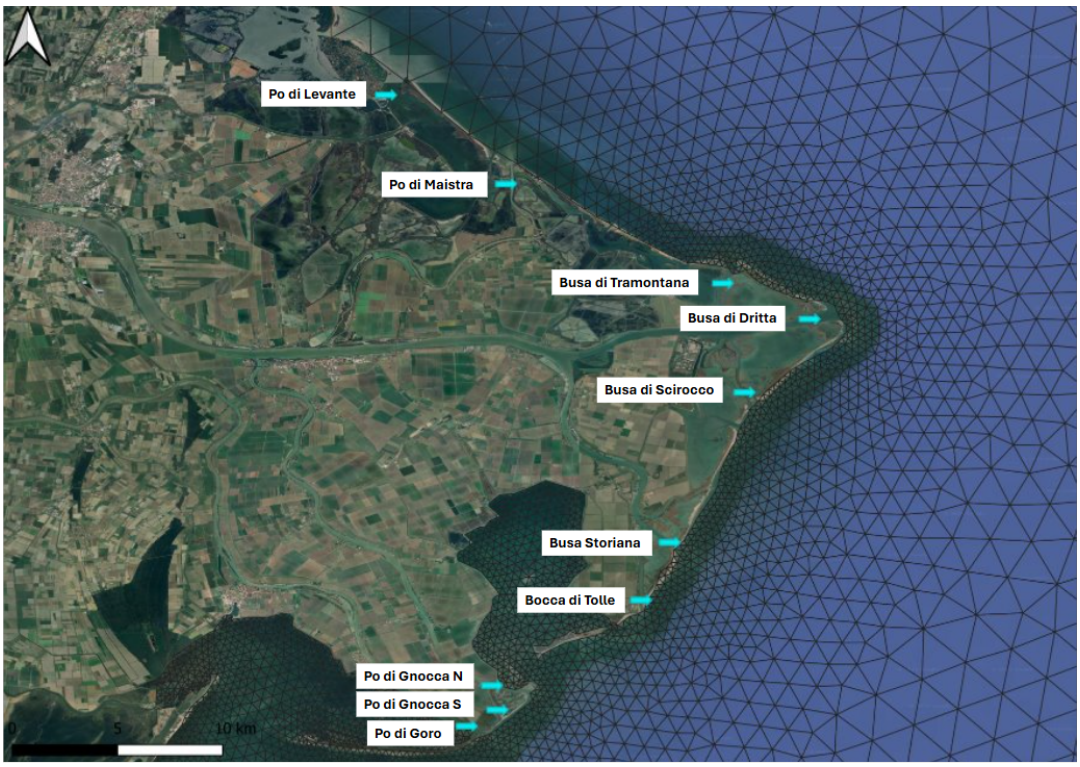

Figure 2.5: Po River Delta, with its mouths distinguished by their respective names.

Po River bifurcates into its multiple mouths. The daily mean discharge data for this station can be obtained from a free platform offered by Arpae. This platform is called Dext3r and can be accessed via the following link: https://simc.arpae.it/dext3r/. The discharge measured at Pontelagoscuro is then divided between the different mouths using the repartitioning method determined by Zasso and Settin (2012) (Arpa Veneto).

2.2 Sediment transport module

The sediment module employed by SHYFEM-MPI is SEDTRANS, which was initially introduced by Li and Amos (2001) and subsequently refined by Neumeier et al. (2008).

The equation employed to calculate the advection and diffusion of suspended sediments is the same as that used for all tracers and it is written as follows (Ferrarin et al., 2010; Verri et al., 2023):

$$\frac{\partial \left(H_l C_{l(i)}\right)}{\partial t} + \frac{\partial U_l C_{l(i)}}{\partial x} + \frac{\partial V_l C_{l(i)}}{\partial y} + \int_{z_l}^{z_{l-1}} \frac{\partial \left(W_l - W_{s(i)}\right) C_{l(i)}}{\partial z} dz = H_l K_{sed,h} \left(\frac{\partial^2 C_{l(i)}}{\partial x^2} + \frac{\partial^2 C_{l(i)}}{\partial y^2} \right) + \int_{z_l}^{z_{l-1}} \frac{\partial}{\partial z} K_{v,l} \frac{\partial C_{l(i)}}{\partial z} dz + F \quad (2.1)$$

Where: H_l denotes the thickness of the l vertical level [m]; $C_{l(i)}[kgm^{-3}]$ represents the concentration of the i^{th} sediment class at the vertical layer l; $U_l, V_l[m^2s^{-1}]$, are, respectively, the integrated velocities over the layer l in x and y direction, while $W_l[ms^{-1}]$ is the velocity in the z direction at the layer l; $W_{s(i)}\ [ms^{-1}]$ is the settling velocity for the sediment class i; $K_{sed,h}[m^2s^{-1}]$ is the horizontal turbulent diffusion coefficient; $K_{v,l}[m^2s^{-1}]$ is the vertical turbulent diffusion coefficient for the l level; and finally, F represents the external source terms.

The difference between the advection and diffusion equation for sediments and other tracers, such as salinity and temperature (equations presented in Verri et al. (2023)), is the presence of a settling velocity for the particles. $W_{s(i)}$ is added to the vertical advective term. Sediment particles are known to exhibit a natural tendency to settle.

The vertical boundary conditions for sediments are expressed as follows:

$$-K_{v,top}\frac{\partial C_{(i)}}{\partial z}\bigg|_{z=top} + W_{s(i)}C_{top(i)} = 0 \tag{2.2}$$

$$+K_{v,bot}\frac{\partial C_{(i)}}{\partial z}\bigg|_{z=bot} + W_{s(i)}C_{bot(i)} = ED_{(i)} \tag{2.3}$$

The net exchange flux between the water column and the seafloor for sediment class i^{th} is denoted by $ED_{(i)}[kgm^{-2}s^{-1}]$. Specifically, ED exhibits a positive value in the event of resuspension of sediments, and a negative value in the event of deposition.

The particle settling velocity is calculated using the Soulsby (1997) method:

$$W_{s(i)} = \frac{\nu}{D_{(i)}}\left[\left(10.36^2 + 1.049D_{*(i)}^3\right)^{0.5} - 10.36\right] \tag{2.4}$$

$\nu[kgm^{-1}s^{-1}]$ is the kinematic viscosity of the seawater; $D_{(i)}[m]$ is the diameter of sediment class i, and $D_{*(i)}[-]$ is the dimensionless diameter, calculated as:

$$D_{*(i)} = \left[\frac{g\left(\frac{\rho_s}{\rho_w} - 1\right)}{\nu^2}\right]^{\frac{1}{3}} D_{(i)}$$

where $g[ms^{-2}]$ is the gravitational acceleration, ρ_s and $\rho_w[kgm^{-3}]$ are the sediment and water densities, respectively. The sediment density is the grain density.

It is important to note that Soulsby's method is not the only one that can be used to define

the settling velocity. Another method that has been employed in previous studies (e.g. Wang and Pinardi (2002), Wang et al. (2007), and Guarnieri-Minnucci (2011)) is to calculate $W_{s(i)}$ using Stokes' law:

$$W_{s(i)} = \frac{gD_{(i)}^2}{18\nu}\left(\frac{\rho_s}{\rho_w} - 1\right)$$

Sediment transport can occur in two diverse ways: as bed transport or suspended sediment transport. The former type of transport represents sediment moving just above the seabed by saltation or rolling, and the threshold for its initiation is calculated using the modified Yalin method, as outlined by Miller et al. (1977). This method is employed to define the Shield parameter, denoted by ϑ_{cr}, based on the Yalin parameter, Y:

$$Y = \sqrt{\frac{(\rho_s - \rho_w)\, gD^3}{\rho_w \nu^2}}$$

$$\begin{cases} log\vartheta_{cr} = 0.041(logY)^2 - 0.356logY - 0.997 & \text{for } Y \leq 100 \\ log\vartheta_{cr} = 0.132logY - 1.804 & \text{for } 100 < Y \leq 3000 \\ \vartheta_{cr} = 0.045 & \text{for } Y > 3000 \end{cases} \tag{2.5}$$

The conversion of the Shield parameter to the critical shear velocity is achieved through the utilisation of the following equation:

$$U_{cr,b} = \sqrt{\vartheta_{cr}\frac{(\rho_s - \rho_w)gD}{\rho_w}}$$

Conversely, suspended sediment transport constitutes the sediment particles dispersed along the water column and transported by advection and diffusion. The calculation of the threshold velocity for suspended matter transport is achieved by means of the Van Rijn method (Van Rijn et al., 1993):

$$\begin{cases} \frac{U_{cr,s}}{W_s} = \frac{4}{D_*} & \text{for } 1 < D_* \leq 10 \\ \frac{U_{cr,s}}{W_s} = 0.4 & \text{for } D_* > 10 \end{cases} \tag{2.6}$$

After the critical shear velocities for initiation of motion, the model calculates several other variables. The following list provides a detailed description of these variables:

$U_a, U_{100}[ms^{-1}]$: current velocity at the top of the wave-current boundary layer and current velocity one metre above the seabed;

$\phi_b, \phi_{100}[rad]$: angle between wave and current direction within the wave boundary layer and at one metre above the seabed;

$U_{s,c}, U_{s,w}, U_{s,cw}[ms^{-1}]$: skin friction shear velocity for current, wave and combined case;

$U_{se,cw}[ms^{-1}]$: effective combined skin friction shear velocity;

$U_{sb,cw}[ms^{-1}]$: transport related combined shear velocity;

$U_c, U_w, U_{cw}[ms^{-1}]$: total shear velocity from current, wave and combined cases;

The table 2.1 provides an overview of several additional parameters calculated for sediment transport.

A comprehensive description of the calculation of these variables and parameters can be found in the work of Li and Amos (2001). It is imperative to acknowledge that the model segregates the calculation process into three distinct cases: pure current, pure wave, and combined. The distinction between these three cases is determined by the variables $U_{b,w}$ and $U_{z,c}$, which represent the bottom orbital velocity given by the waves and the current velocity at a height z from the seabed, respectively. It is noteworthy that for $U_{b,w} < 0.01$ there is a pure current case, for $U_{z,c} = 0$ there is a pure wave case, otherwise there is a combined case.

The bottom orbital velocity, denoted by $U_{b,w}$, and the bottom horizontal excursion, denoted by $A_{b,w}$ [m] are defined by linear wave theory. In particular, the wave parameters are calculated

Parameter	Description
Z_0	Bed roughness [m]
$Z_{0,c}$	Apparent bed roughness length
f_{cw}	Bed friction factor [-]
δ_{cw}	Height of the wave current boundary layer [m]

Table 2.1: Parameters employed in the calculation of sediment transport.

using the wave significant height, H_s, and the wave period, T:

$$U_{b,w} = \pi \frac{H_s}{T \sinh(kh)}$$

$$A_{b,w} = \frac{U_{b,w}}{\omega}$$

where: k [-] is the wave number; h [m] is the water depth; and $\omega[s^{-1}]$ is the angular frequency of the wave.

It is possible to calculate these using the mean wave period, T_m, or the peak wave period, T_p. As there is no coupling to a wave model for this research, waves are calculated using an additional module offered by SHYFEM-MPI, which uses linear wave theory. In particular, the waves are calculated using the empirical equations given in the Shore Protection Manual (Center, 1984):

$$\frac{gH_s}{U_A^2} = 0.283 tanh\left[0.530\left(\frac{gh_a}{U_A^2}\right)^{\frac{3}{4}}\right] tanh\left[\frac{0.00565\left(\frac{gX}{U_A^2}\right)^{\frac{1}{2}}}{tanh\left[0.530\left(\frac{gh_a}{U_A^2}\right)^{\frac{3}{4}}\right]}\right]$$

$$\frac{gT_p}{U_A} = 7.54 tanh\left[0.833\left(\frac{gh_a}{U_A^2}\right)^{\frac{3}{8}}\right] tanh\left[\frac{0.0379\left(\frac{gX}{U_A^2}\right)^{\frac{1}{3}}}{tanh\left[0.833\left(\frac{gh_a}{U_A^2}\right)^{\frac{3}{8}}\right]}\right]$$

U_A $[ms^{-1}]$ is the wind speed, h_a [m] is the average water depth along the fetch, and X [m] is the wind fetch, which varies with wind direction.

The methodology employed for wave calculations is overly simplistic in nature, thus being incapable of describing swells; it is only able to describe generation waves. Moreover, it does not consider other processes such as reflection, refraction and wave breaking. The prevailing wind field and the same domain are the only forcing considerations taken into account. Given these limitations, the wave model is expected to provide reasonably accurate results under intense Bora conditions but may underestimate the wave field under all other conditions, particularly during Scirocco events. To validate this hypothesis, a comparative analysis is conducted between model outcomes and observational data. Specifically, the comparison is made in three different periods: one under intense Bora conditions, another under a Po flood with Scirocco winds, and a third mixed condition (subsequent Scirocco and Bora events). The observations utilised for the comparison are provided by the Nausicaa wave buoy, which is located eight kilometres off the coast of

Cesenatico at a depth of ten metres (for further information, please refer to the Arapae website: https://www.arpae.it/it/temi-ambientali/mare/dati-e-indicatori/dati-boa-ondametrica). The parameters considered for the comparison are: significant wave height, H_s, and mean wave period, T_m.

The first comparison is made for an intense Bora event recorded between 25^{th} and 26^{th} of March 2019, more information on the event is provided in chapter 3.3.1. The comparison for the significant wave height and the mean wave period are shown in figure 2.6 plots (a) and (b), respectively. Upon examination of both plots, it becomes evident that the model underestimates both wave parameters. This underestimation is observed to increase on the 4^{th} of April, coinciding with the onset of Scirocco wind conditions. Notwithstanding, the model displays a competent representation of the wave conditions for this period, albeit with a certain degree of underestimation.

The second comparison is made during the Po flood of 2019, which took place between November and December. Further information regarding this event can be found in chapter 3.3.2. The comparison between the Nausicaa buoy observations and the model results is shown in figure 2.7. In this case, the underestimation of the model is significantly larger than in figure 2.6, like the underestimation from the 4^{th} of April. This outcome is consistent with the prevailing wind conditions during the flood, namely Scirocco, which was the dominant wind regime in the domain. Furthermore, examination of plot (b) of figure 2.7 reveals an increase in the mean

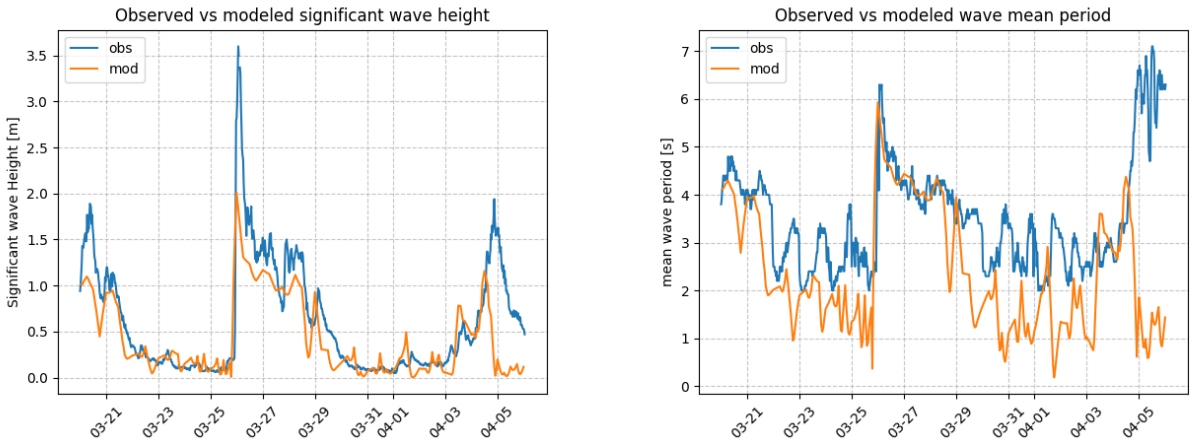

(a) (b)

Figure 2.6: Comparison made between the model (yellow) and the observations (blue) at the Nausicaa wave buoy during an intense Bora event (25-26 March 2019). The two plots demonstrate the significant wave height (a) and the mean wave period (b).

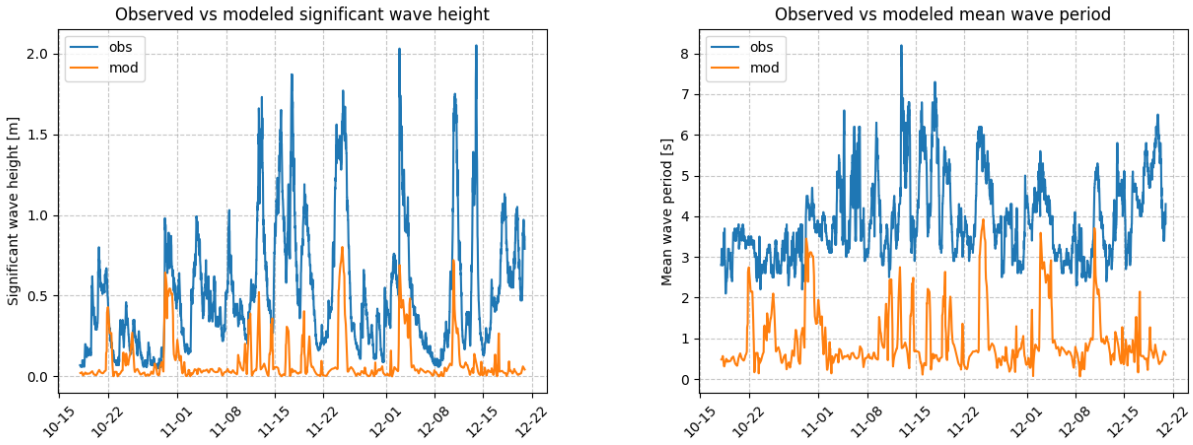

(a) (b)

Figure 2.7: Comparison made between the model (yellow) and the observations (blue) at the Nausicaa wave buoy during the 2019 Po flood. The two plots demonstrate the significant wave height (a) and the mean wave period (b).

wave periods recorded by the buoy. This indicates that the waves observed are associated with swell, a phenomenon not supported by the linear theory employed by the model.

The third and final period for comparing wave data with model results is carried out under mixed conditions. Specifically, the period under consideration extends from 1^{th} to 20^{th} May, as two distinct wave events were documented during this time: the initial event commenced on the 5^{th} and persisted for less than a day under Scirocco conditions, while the subsequent event began on the 12^{th} and endured for nearly three days under Bora conditions. The comparison is displayed in figure 2.8. The underestimation observed in this study is positioned between the

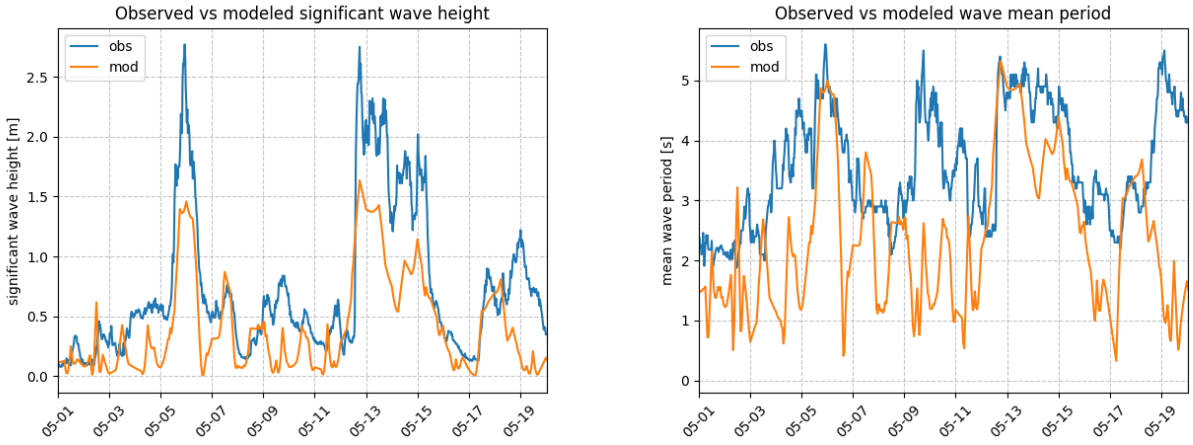

(a) (b)

Figure 2.8: Comparison made between the model (yellow) and the observations (blue) at the Nausicaa wave buoy during two consecutive wave events in different wind regimes. The two plots demonstrate the significant wave height (a) and the mean wave period (b).

underestimation recorded in figures 2.6 and 2.7. The model demonstrates an overall capacity to represent the wave field within the study area, though it does exhibit a tendency towards underestimation. This underestimation is observed to increase in the presence of swell waves within the domain (figure 2.7), while it is observed to decrease under conditions of intense Bora (figure 2.6). This finding aligns with the initial expectations derived from the application of this elementary wave model. Notwithstanding this underestimation, the decision has been taken to continue using this simple wave model, as it remains the sole available method to incorporate wave action in the SHYFEM-MPI sediment transport calculations, a process which is significant to sediment transport in coastal areas (Wang and Pinardi, 2002).

To calculate sediment transport rates for each sediment class, SEDTRANS divides them into cohesive and non-cohesive sediments. This is because these two sediment classes behave in markedly diverse ways. Specifically, cohesive sediments have a propensity to flocculate, and their sole mode of transport is by suspension. Conversely, non-cohesive sediments do not flocculate, and their transport can be by either suspension or bedload.

For the purposes of this project, all sediment classes are considered to be non-cohesive. This approach aligns with the methodology employed in previous studies of sediment transport in the northern Adriatic Sea (e.g. Wang et al. (2007)). For those interested in the algorithm used for cohesive sediments, a thorough description can be found in Li and Amos (2001) and Neumeier et al. (2008).

For non-cohesive sediments, transport rates can be calculated using five different methods. An overview of these methods can be found in table 2.2, along with the recommended particle size range. It is important to note that total load methods already calculate the transport rate of both bedload and suspended sediment, without dividing between the two modes, while bedload only methods calculate the suspended sediment rate separately.

Method	transport mode	grain-size[mm]
1.Engelund and Hansen (1967)	Total load	> 0.15
2.Brown (1950)	Bedload	0.3-28.6
3.Bagnold (1963)	Total load	0.18-0.45
4.Yalin (1963)	Bedload	> 0.2
5.Van Rijn et al. (1993)	Bedload	0.05-29.1

Table 2.2: Summary of the possible methods for calculating the transport of non-cohesive sediments, along with their appropriate grain size range. Source: Neumeier et al. (2008)

A review of the extant literature reveals that only two of the five methods have been utilised to study sediment transport in the northern Adriatic: the Engelund-Hansen method (Umgiesser et al., 2006) and the Van Rijn algorithm (Ferrarin et al., 2016). The Engelund-Hansen method is a total load method, while the Van Rijn algorithm is a bedload-only method. Consequently, this study will focus exclusively on these two algorithms, aiming to ascertain which one provides the most accurate result for the sediment transport processes in the study area.

For the Engelund-Hansen algorithm, the total load sediment transport, $q[m^2 s^{-1}]$, in a pure current case is calculated using the following equation:

$$q = 0.05 U_{100}^2 \frac{\rho_w^2 U_{s,c}^3}{D\left[g\left(\rho_s - \rho_w\right)\right]^2} \tag{2.7}$$

In the case of the combined case, the equation 2.7 remains unchanged; however, the current skin friction shear velocity, $U_{s,c}$, is substituted with the combined skin friction shear velocity, $U_{s,cw}$.

Conversely, the Van Rijn algorithm in a pure current case, calculates the bedload transport rate, $q[m^2 s^{-1}]$, as follows:

$$q = 0.053 \sqrt{g\left(\frac{\rho_s}{\rho_w} - 1\right)} D^{1.5} D_*^{-0.3} \left(\frac{\tau_{s,c} - \tau_{cr,b}}{\tau_{cr,b}}\right)^{2.1} \tag{2.8}$$

$\tau_{s,c}[kgm^{-1}s^{-2}]$, is the skin friction shear stress given by the current, while $\tau_{cr,b}[kgm^{-1}s^{-2}]$ is the critical stress for initiation of bedload transport. The aforementioned stresses are calculated as follows: $\tau = \rho_w U^2$ using the previously determined velocities. The velocities are skin-friction shear velocities and already take into account the friction coefficient, so it should not be added to the equation.

Conversely, the bedload transport for the combined case ($U_{b,w} > 0$) is calculated as follows:

$$q = 0.25 \left(1 - \sqrt{\frac{H_s}{h}}\right) D D_*^{-0.3} U_{s,cw} \left(\frac{\tau_{s,cw} - \tau_{cr,b}}{\tau_{cr,b}}\right) \tag{2.9}$$

Using the Van Rijn method, the suspended load is defined as the net flux exchange between the water column and the seabed (ED), which is calculated immediately following the bedload transport rate. The expression for the suspended sediment flux is derived as the difference

between the equilibrium concentration and the suspended sediment concentration at the lowermost vertical level, as expressed in the following equation (Lesser et al., 2004):

$$\begin{cases} ED_{(i)} = C_{bot(i)} \left(\frac{K_v}{\Delta z} + W_{s(i)}\right) & \text{for } C_{eq(i)} < C_{bot(i)}[\text{sink}] \\ ED_{(i)} = \overline{C_{eq(i)}} \left(\frac{K_v}{\Delta z}\right) & \text{for } C_{eq(i)} \geq C_{bot(i)}[\text{source}] \end{cases} \tag{2.10}$$

The equilibrium concentration, $C_{eq(i)}$, is calculated using the following formula (Smith and McLean, 1977):

$$C_{eq(i)} = 0.65\eta_i\gamma_0\frac{\tau_*}{1+\tau_*}$$

In these equations: $\Delta z[m]$ is the vertical distance between the centre of the last layer ($\frac{H_{bot}}{2}$, where H_{bot} is the thickness of the last vertical layer) and the bottom roughness height, $Z_0[m]$. The sink and source terms are employed exclusively to delineate between the two distinct scenarios. Specifically, the sink condition describes the process of sediment removal from the water column (deposition, $ED_{(i)} < 0$), while the source condition describes the process of sediment addition to the water column from the seafloor (erosion, $ED_{(i)} > 0$). The availability of the i^{th} sediment fraction at the bottom is denoted by η_i and the empirical sediment resuspension coefficient is denoted by γ_0. τ_* represents the normalised excess shear stress and it is calculated as $\tau_* = \frac{\tau_{s,cw}+\tau_{cr,s}}{\tau_{cr,s}}$. For a pure current case, the previous equation is changed to: $\tau_* = \frac{\tau_{s,c}+\tau_{cr,s}}{\tau_{cr,s}}$
If both the bedload and suspended sediment transport rates, calculated using the Van Rijn method, or the total load rate, calculated using the Engelund and Hansen method, are known, it is possible to determine the changes in bed elevation (h_b [m]). Utilising the continuity equation for sediments, the bed elevation change attributable to bed load or total load is expressed as follows (Ferrarin et al., 2008):

$$\frac{\partial h_b}{\partial t} = \frac{1}{1-\epsilon}\left(\frac{\partial q_x}{\partial x} + \frac{\partial q_y}{\partial y}\right) \tag{2.11}$$

q_x and $q_y[m^2s^{-1}]$ denote the bedload transport rate, as measured by the Van Rijn method, or the total load transport rate, as determined by the Engelund and Hansen method, in the x and y directions, respectively. The surface porosity, denoted by $\epsilon[-]$, is to be utilised for the purpose of newly deposited sediments. The value of 0.6 is employed in this thesis.
For methods that calculate a total load rate, the bed elevation change is determined exclusively

by the equation 2.11. Conversely, for methodologies that distinguish between bed load and suspended load transport rates, an additional equation must be incorporated. This additional relation is employed to describe the bed elevation changes due to the redistribution of suspended transport and is written as:

$$\rho_s(1-\epsilon)\frac{\partial h_b}{\partial t} = -\sum_{n=1}^{N} ED_{(i)} \tag{2.12}$$

For methods that separate bedload and suspended load rates, the total bed elevation change is given by the sum of these two equations, 2.11 and 2.12.

2.2.1 Lateral and bottom boundary conditions for sediments

As the present project has a focus on the study of sediment transport, two additional conditions are introduced in relation to those employed by Alessandri (2022).
The first condition is the bottom boundary for sediments, which characterises the sediment classes present on the seabed of the study area, with their respective specifications.
The second condition is the lateral boundary condition at the river outlets, which specifies the sediment load forcing. It is important to note that solid load data and climatologies are only available for a limited number of Italian rivers. However, for the purposes of this thesis, a data set was identified with daily solid loads for the Po River, and climatologies indicating the total annual solid load for the Savio and Reno rivers, taken from Billi and Spalevic (2022).

Bottom boundary condition - Seabed composition

As previously mentioned in chapter 1.3 and visually shown in figure 1.5, four distinct sediment classes are present in the study area. Consequently, this thesis proposes an initialisation of the seabed with four different sediment classes, characterised by four distinct grain sizes:

Mud: 32.5 μm

Sandy mud: 94 μm

Muddy sand: 187 μm

Sand: 375 μm

These four classes are placed at equal percentages (25%) throughout the domain's seabed, resulting in a constant average grainsize of 172.1 μm throughout the study area.
The seabed pattern of figure 1.5 was not chosen as the initial bottom condition for sediments because the depositional pattern is highly related to the sediment transport processes. One aim of the model is to resemble that same pattern. In fact, resembling the depositional pattern would indicate that the model can describe how the different sediment classes are transported throughout the domain.

Lateral boundary condition - Solid load by rivers

In addition to the daily mean discharge, as previously introduced in chapter 2.1.1, the Pontelagoscuro station also has a dataset for specific turbidity. This dataset encompasses the period from 31.12.2010 to 01.01.2020, and it is available for download from Dext3r.
The measurement of specific turbidity was conducted daily, employing the Rossetti probe technique:

1. a one-litre sample of water was taken at one metre from the riverbed at three distinct locations of the river cross section. Specifically, the samples are to be taken at $\frac{1}{4}$, middle and $\frac{3}{4}$ points of the cross-section. The daily sample should thus be of three litres;
2. the filter is then heated until 110 °C, dried and then weighed;
3. the water sample is filtered through the previous filter, heated until 110 °C, dried and weighed;
4. the former weight (filter only) is then subtracted from the latter (filter plus sample) [g];
5. the weight [g] is then transformed into a concentration $[gl^{-1}]$, based on the initial volume of the sample (3 l);
6. the concentration $[kgm^{-3}]$ is then related to the liquid discharge $[m^3s^{-1}]$, to get the solid discharge $[kgs^{-1}]$

It is important to note that samples were taken only during working days; while on non-working days, a linear interpolation between the two successive sample weights (calculated at step 4 of

the process) is done. To illustrate this process, consider the case of Saturday and Sunday, for which a linear interpolation is performed between the weights of Friday and Monday.
The solid discharge measured at Pontelagoscuro station is then divided between the different Po branches following the partitioning outlined in the work of Correggiari et al. (2005): 1% at Po di Maistra, 73% at the Po di Pila, 7% at Po di Tolle, 11% at Po di Gnocca and 8% at Po di Goro. It should be noted that this partitioning exclusively considers the main branches of the Delta, excluding the actual mouths. The assumption is made that the partitioning of solid transport from the main branches is equivalent to that of liquid discharge.
The sediment data must be provided to the model as a concentration $[kgm^{-3}]$ for each grain size considered in the simulation and over the entire simulation time.
For the other two rivers, Savio and Reno, there is an indication of the mean annual sediment yield (see figure 2.4 for the location of the two rivers) in Billi and Spalevic (2022). Specifically, the Reno has a mean suspended yield of 943 $tkm^{-2}yr^{-1}$ and the Savio has a mean yield of 1490 $tkm^{-2}yr^{-1}$. The hydrological areas of the two rivers are 1051 km^2 and 586 km^2, respectively, which result in a mean sediment yield of: 991.09 $ktyr^{-1}$ for the Reno river and 873.14 $ktyr^{-1}$. Utilising these values, it is feasible to calculate a sediment transport rate, in kgs^{-1}, for the two rivers.

Notably, this research does not encompass sediment input from beaches and dunes. The primary rationale for this exclusion is the absence of the relevant type of lateral\surface boundary in SHYFEM-MPI, while the secondary rationale is the paucity of data concerning this process along the specified coastline.

Once the sediment transport module and its associated equations are understood, it becomes feasible to initiate a sensitivity analysis of the sediment transport parameters. The subsequent chapter will present the sensitivity analysis conducted over the sediment parameters, with the objective of identifying the most suitable configuration to describe sediment transport processes in the study area.

Chapter 3

Sensitivity analysis

To ascertain the most appropriate configuration of the model to describe the sediment transport processes in the study area, a sensitivity analysis is conducted. Furthermore, the objective of the sensitivity analysis is to enhance the comprehension of the sediment transport module offered by SHYFEM-MPI and its parameters. It should be noted that no sensitivity analysis was carried out on the hydrodynamics, since Alessandri (2022) had already conducted this type of analysis and the parametrization used is the same one, only with the addition of sediments. As previously mentioned, in this research all the sediment classes are treated as non-cohesive, so the sensitivity analysis does not consider parametrizations related to cohesive sediments. The subsequent sections contain the following: the sensitivity matrix employed in this project, accompanied by a concise explanation of the values considered for the analysis; the data set utilised to ascertain the most effective model setting; and an overview of the results obtained from for the analysis.

3.1 Sensitivity matrix

As illustrated in table 3.1, the document provides a comprehensive overview of the parameters considered in the sensitivity analysis, along with a detailed exposition of the values employed. The initial critical erosion stress, designated as τ_c [Pa], assigned to each sediment class, is the primary parameter examined in the sensitivity analysis. This parameter must be specified for all the sediment classes considered in the simulation, and two different approaches are used to define it for the sensitivity analysis. The first approach involves setting the same critical

Parameter	Values
Critical erosion stress, τ_c [Pa]	τ_c=0.02 for all sediment classes; τ_c calculated using Miller et al. (1977)
Settling velocity calculation, W_s	Soulsby (1997); Stokes law
Sediment transport calculation method	Engelund and Hansen (1967); Van Rijn et al. (1993)
Sediment classes forced at the Po River	4 classes (all); 2 classes (32.5 & 94μm); 2 classes (14 & 32.5μm)
Parametric waves	Yes; No
Sediment horizontal diffusion coefficient, $K_{sed,h}$	0; 0.005; 0.01; 0.05; 0.1; 0.2; 1
Sediment density, ρ_s [kgm^{-3}]	2650; 1800

Table 3.1: Sensitivity matrix of this thesis. For each parameter, the range of values considered for the analysis is specified.

erosion stress (0.02 Pa) for all the sediment classes under consideration, as previously outlined by Guarnieri et al. (2014). The second approach involves calculating the critical erosion stress using the method developed by Miller et al. (1977), as previously detailed in chapter 2.2. The critical erosion stresses for the latter method are as follows: 0.041, 0.058, 0.098, 0.15, 0.22 Pa, respectively for the grain sizes 14, 32.5, 94, 187, 375 μm.

The second sediment parameter considered for the sensitivity analysis is the settling velocity, W_s [ms^{-1}]. The settling velocity of the sediment classes is calculated using two different methods: the Soulsby (1997) method and the Stokes law. The settling velocities of the various grain sizes utilised in this study, are outlined in table 3.2, with the calculation of these velocities employing the methods.

The third parameter considered for the sensitivity analysis is the approach used to calculate sediment transport rates. Specifically, out of the five approaches offered by SHYFEM-MPI, only two are considered in this analysis: the method outlined by Engelund and Hansen (1967) and the method outlined by Van Rijn et al. (1993). The former approach calculates the total load of sediment transport, while the latter calculates separately the bed and suspended load. It is noteworthy that both methods have been previously employed to study sediment transport processes in Venice lagoon, which is geographically proximate to the study area and is situated within the northern Adriatic Sea basin. Consequently, it is hypothesised that the two methods

Grain size [μm]	14	32.5	94	187	375
W_s with Soulsby (1997) [mms^{-1}]	0.154	0.83	6.75	22.8	55.3
W_s with Stokes law [mms^{-1}]	1.69	9.13	7.63	30.2	122

Table 3.2: Settling velocities [ms^{-1}] of the various sediment classes utilised in the research. Two distinct methods were employed to calculate the settling velocities.

will also be the most suitable for the study of sediment transport along the Emilia-Romagna coastline. Furthermore, the discrepancy between the sediment transport calculations obtained using a total load method and those derived from a method that separates suspended and bed load transport is of interest. It is expected that the Van Rijn method will produce the most accurate results, particularly in view of the grain size range for which it has been validated, and the grain sizes utilised in this study.

The fourth aspect that has been considered for the sensitivity analysis is the sediment classes forced at the Po River open boundaries. To this end, three distinct configurations have been determined: the first configuration involves the application of all four sediment classes presented in chapter 1.4 at the river's mouths, with a 25% share of the total suspended load allocated to each class. The second configuration involves the application of only the two finer classes (mud and muddy sand) at the boundaries, with a 50% share of the total suspended sediment concentration allocated to each class. Finally, the third configuration involves the introduction of a new sediment class that is finer than all the previous ones (14 μm), and the total suspended sediment concentration used as forcing is divided equally between this new class and the other mud grain size (32.5 μm). The selection of this configuration is primary informed by extant literature, with reference to the transport of fine sediments into the Adriatic Sea by the Po River (Spagnoli et al., 2014). The decision is also informed by a measuring campaign conducted by Arpae in collaboration with the University of Ferrara (UNIFE). Specifically, the 2023 measuring campaign at Boretto station (216 km from the Delta area and 125 km upstream from Pontelagoscuro) revealed that most of the suspended sediment in the Po River is classified as silt (grain sizes between 2 and 63 μm). The value of 14 μm used in the simulations is based on the D_{50} of 18 μm measured at Boretto station, with the assumption that downstream, the grain sizes transported in suspension are finer. It is noteworthy that this configuration bears a resemblance to the setup employed in the study by Bever et al. (2009), where the two sediments discharged by the Po have a grain size of 15 and 63 μm, respectively.

The fifth parameter presented in the sensitivity table pertains to parametric waves. The objective of this analysis was to ascertain whether the utilisation of parametric waves, as provided by SHYFEM-MPI, yielded superior results in the representation of sediment transport when compared with the simulation involving only currents.

τ_c [Pa]	W_s calculation	sediment transport method	sediment at rivers	waves	$K_{sed,h}$ $[m^2s^{-1}]$	ρ_s $[kgm^{-3}]$
Calculated τ_c	Soulsby (1997)	Van Rijn et al. (1993)	4 classes	Yes	0	2650

Table 3.3: Values employed during the preliminary configuration of the model. The simulation is recognised by the addendum _4tauin to the simulation name.

The second-to-last parameter under consideration for the sensitivity analysis is the sediment horizontal diffusion coefficient. For this coefficient, the default value is 0, which is consistent across all the horizontal diffusion coefficients of tracers. As there is no information on values previously used in sediment transport research, it was decided to consider seven different values, starting with the default, and reaching a value of 1.

The last parameter considered is the sediment density, ρ_s. Two values are considered here: the default value of 2650 kgm^{-3} and the sediment density used by Guarnieri-Minnucci (2011) of 1800 kgm^{-3}.

The first configuration of the model used for the sensitivity analysis is described in table 3.3. From this configuration, only one parameter at a time was changed, resulting in thirteen simulations that were then compared.

A paucity of studies has been published on the subject, with the present author's research being the only one to calibrate sediment transport modelling using SHYFEM-MPI. The model developed by Ferrarin et al. (2010) can achieve a factor of two discrepancy between measured and modelled sediment transport values.

3.2 Measurement of near-surface Suspended Particulate Matter conducted through satellite imagery

To ascertain the most efficacious model parametrization in describing the sediment transport processes, observations are required. Indeed, the optimal model configuration is identified as that which yields the most precise correlation with observed values.

The project's two primary objectives are to study the sediment transport processes and their resulting depositional/erosion patterns along the Emilia-Romagna coastline. The variables of major interest are as follows: Suspended Sediment Concentrations (SSCs) and erosion/deposition rates, respectively. To analyse the latter variable, two bathymetric datasets for the same area

or transect are required. These two measurements should be taken after an interval of several weeks (15-20) to be able to see bed changes. This type of information is not available, especially for the time interval when turbidity data is available at Pontelagoscuro. Instead, for the former variable, datasets of Suspended Particulate Matter (SPM) derived from satellite imagery are available.

CMEMS provides various satellite observation datasets for different oceanographic variables (e.g. surface water temperature, sea surface height, Suspended Matter, Chlorophyll-a, etc.), but for this research, the focus is on datasets related to Ocean Colour. An overview of the assorted products offered by CMEMS can be found in Colella et al. (2023). All ocean colour products are classified as level 3 or 4, indicating that the raw satellite data (level 1) is processed to generate accessible datasets for end users. Level 3 products, for instance, represent the daily composite of a specific variable, obtained by merging all satellite passages during that day. In contrast, level 4 products employ temporal averaging on a monthly basis or an interpolation procedure to fill missing values in the dataset.

Of the datasets examined, a mere two encompassed the time period, spatial area of interest of this research and had SPM measurements: the Global Ocean Colour (Copernicus-GlobColour), Bio-Geo-Chemical, L3 (daily) from Satellite Observations (1997-ongoing) [product name: OCEANCOLOUR_GLO_BGC_L3_MY_009_103], and the North Atlantic Ocean Colour Plankton, Reflectance, Transparency and Optics MY L3 daily observations [product name: OCEANCOLOUR_ATL_BGC_L3_MY_009_113]. In addition to the spatial domain encompassed by the two datasets, the former encompasses the global ocean (latitude from 90°S to 90°N and longitude from 180°W to 180°E), while the latter is confined to the Atlantic ocean (latitude from 20°N to 66°N and longitude from 46°W to 13°E). A salient difference between the two is the resolution. Specifically, the resolution for the GLO dataset is 4 km, while the ATL dataset has a resolution of 1 km. As illustrated in figure 3.1, a comparison is made between the SPM measurements of the two datasets for the same date (27.04.2019).

Between the two datasets, only the higher resolution one is considered in this research. This is primarily due to the highly confined nature of the study area and the exceptional resolution of the grid, particularly in the coastal regions where most of the sediment transport is anticipated. Furthermore, as there is a strong interest in accurately representing the sediment plume of the

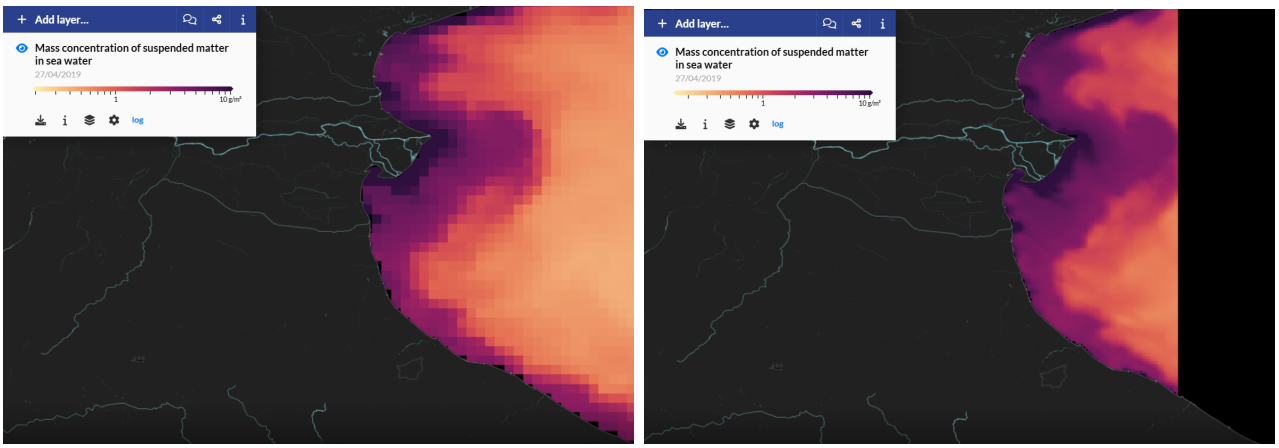

(a) OCEANCOLOUR_GLO_BGC_L3_MY_009_103

(b) OCEANCOLOUR_ATL_BGC_L3_MY_009_113

Figure 3.1: Comparison of the two available datasets for SPM measurements. Both images depict the SPM recording for the 27^{th} April 2019.

Po River, it is evident from figure 3.1 that the product which provides superior representation is the one shown in figure 3.1(b).

The dataset is presented as a daily value of SPM, expressed in gm^{-3}. It should be noted that the dataset exclusively pertains to inorganic matter. The daily values, as previously mentioned, are obtained by merging all the satellite passages available for that day; thus, the data is collected over a 24-hour period, and no information is provided on the time at which the satellites collected the data. In addition to SPM, the dataset encompasses a measurement of the Secchi depth of sea water (ZSD) for each SPM measurement. The Secchi depth is utilised to quantify the transparency of the water, and it is subject to noteworthy influence from turbidity. Consequently, the Secchi depth is utilised as an indicator of the depth to which the satellite sensor can penetrate below the sea surface for a given date. In instances where the SPM dataset is available, it is presented as a surface value. The data is saved on a regular grid with a resolution of one km and can be freely downloaded from the CMEMS website in NetCDF format.

Copernicus offers a further tool (accessible at https://browser.dataspace.copernicus.eu/) that enables the visualisation of raw data collected by various satellites. However, of all the satellites, merely two - Sentinel 2 and Sentinel 3 - collect data for water bodies and oceans. These satellites are equipped with MSI and OLCI sensors, respectively, enabling the acquisition of true-colour images. The SPM concentrations can then be derived from these images using the ACOLITE processor (further information on the processor is available at:

https://odnature.naturalsciences.be/remsem/software-and-data/acolite). Of the two satellites, Sentinel 2 offers the optimal images for the study period, and these images align closely with the measurements provided by the CMEMS dataset, as demonstrated in figure 3.2. This figure presents the raw satellite data and the corresponding SPM measurement from the CMEMS for the same date (01.04.2019). It is evident from the figure that the satellite image employed to calculate the SPM is the one displayed in the Copernicus Browser, as the two images exhibit analogous patterns (e.g. in the vicinity of Comacchio and Ravenna, the two plumes extending eastward towards the open ocean). This observation suggests that the Sentinel satellites are utilised for the calculation of SPM concentrations in CMEMS, and the time which the images were collected can be obtained from Copernicus Browser. The decision has been taken to employ Sentinel 2 data exclusively, as they provide the most suitable images for the study period, with a maximum cloud cover of 30%. This parameter can be configured within Copernicus Browser. A comprehensive list of all available dates in 2019 that meet these criteria is provided in the Appendix C, and all images are collected around 10 o'clock.

It is possible to compare the model outputs (which are set to be provided every hour) with the observations, given that the dates and times at which the measurements are taken are known.

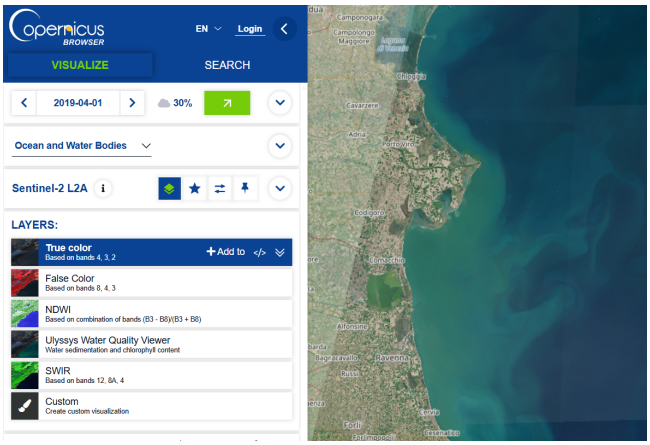

(a) S2A_MSIL2A_20190401T10

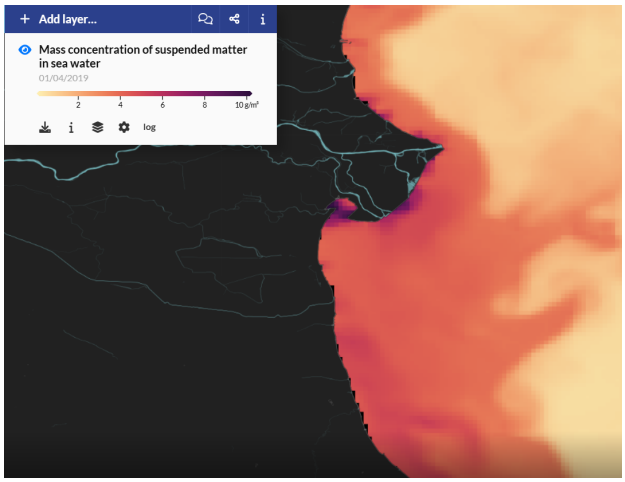

(b) OCEANCOLOUR_ATL_BGC_L3_MY_009_113

Figure 3.2: Raw satellite image and the corresponding SPM measurement for the same date (1 April 2019).

3.2.1 Comparison of satellite data with model results

For the purpose of comparison, the satellite daily values of SPM are juxtaposed with the model result of SSC for the same date at 10 o'clock. The former data set is given as a 2D array (only x and y, dimensions), while the model results for SSC are in 3D (also the vertical dimension, z). To facilitate a meaningful comparison between the two arrays, it is necessary to transform the model results into a 2D format. In this thesis, the daily measured Secchi depth is treated as the maximum depth that can be penetrated by the satellite. The Secchi depth is a measurement of water turbidity and transparency, given in metres, and the depth of light penetration depends on it (Dunn et al., 2019). Consequently, the Secchi depth serves as an indicator of the number of model vertical levels employed in the calculation of the SSC. The model result and the satellite data are both presented as concentrations; however, the satellite dataset is transformed from gm^{-3} to kgm^{-3} to align with the measurement unit of the model results.

The model's output of suspended sediments is provided at all nodes and at all depths. To facilitate a comparison between the model results and the satellite data, the model results are regridded into the regular grid used by the satellite data, from a higher resolution to a lower one. This is because extrapolation is required when regridding from a lower resolution to a higher one (the opposite of the method employed here), which can lead to significant errors. The regridding process employed in this analysis utilises linear interpolation. After this, a comparison can be conducted. For the purposes of this research, three distinct methods have been selected: the Root Mean Square Error (RMSE), the Mean Absolute Error (MAE), and the Pearson correlation coefficient (R). The calculation of each of these statistical indices is outlined below (Campos-Caba et al., 2024):

$$RMSE = \sqrt{\frac{\sum_{i=1}^{N} (\phi_m^i - \phi_o^i)}{N}} \tag{3.1}$$

$$MAE = \frac{1}{N} \sum_{i=1}^{N} \left| \phi_m^i - \phi_o^i \right| \tag{3.2}$$

$$R = \frac{\frac{1}{N} \sum_{i=1}^{N} \left(\phi_m^i - \overline{\phi_m^i} \right) \left(\phi_o^i - \overline{\phi_o^i} \right)}{\phi_{\sigma m} \phi_{\sigma m}} \tag{3.3}$$

The number of observations is denoted by N, while the model outputs and observations of suspended sediment are represented by ϕ_m, ϕ_o, respectively. The mean values are denoted by $\overline{\phi_m}$ and $\overline{\phi_o}$ and the standard deviations are denoted by $\phi_{\sigma m}$ and $\phi_{\sigma o}$.

These indices are used to indicate which model set up gives the best representation of SSCs for the study area. The area average RMSE (calculated considering the entire study area at different dates) is utilised as the statistical indicator for determining the optimal setup.

3.3 Sensitivity analysis done on event scale

For the present project, a sensitivity analysis has been conducted on two distinct events that transpired in 2019. An overview of the events in the Emilia-Romagna region during 2019 is provided in Pavan and Marletto (2020).

The initial event, documented on the 25^{th} and the 26^{th} of March, has been categorised as a level 3 wave event by Arpae (the Arpae scale utilises a 5-level classification system for wave events), exhibiting intense Bora winds. A comprehensive description of the event can be found in Celano and Stanzani (2019).

The second event commenced on the 22^{nd} of November and concluded on the 3^{rd} of December. This event is recognised as a flood of the Po River since its discharge at Pontelagoscuro station reached 8000 $m^3 s^{-1}$. Further details on this event can be found in Ricciardi and Comune (2019).

The subsequent subchapters provide a comprehensive overview of the simulation setups, and the results obtained from these setups.

3.3.1 Level 3 wave event - 25-26 March 2019

The simulations incorporating the wave event commence on 20 March 2019, a period of five days before the actual event, and conclude on 5 April 2019. This decision is made in recognition of the necessity for a spin-up period for the model, owing to the absence of initial condition data concerning the suspended sediments and waves within the designated domain. Initially, the SSC and all the wave variables are set to zero throughout the domain. The additional days are considered because sediment transport is expected to last longer than the event itself.

Four different dates are used to calculate the statistical indices: 22.03.2019, 25.03.2019 (dur-

Simulation	RMSE [kgm^{-3}], 10^{-3}	MAE [kgm^{-3}], 10^{-3}	R [-], 10^{-2}
Event03_4tauin	3.2424	2.1793	3.9966
Event03_tauin0.02	3.2424	2.1793	3.9966
Event03_Stokes	3.2480	2.1803	3.8406
Event03_ENGHAN	3.2476	3.9689	3.5993
Event03_2sed	3.2476	2.1794	3.9800
Event03_2sedfin	3.2562	2.1697	4.7115
Event03_nowaves	3.2471	2.1851	2.8631
Event03_sedhpar0.005	3.2626	2.1812	3.4096
Event03_sedhpar0.01	3.2609	2.1809	3.3996
Event03_sedhpar0.05	3.2404	2.1792	3.9558
Event03_sedhpar0.1	3.2416	2.1802	3.8008
Event03_sedhpar0.2	3.2411	2.1811	3.7567
Event03_sedhpar1	3.2414	2.1828	4.1900
Event03_rhos1800	4.3022	2.1677	7.2746
Event03_2sedfin_SavioReno	4.0957	2.2113	2.8753
Event03_2sedfin_SavioReno2	3.2359	2.1586	5.1457

Table 3.4: Statistical indices calculated for the various setups in relation to the March wave event.

ing the wave event), 30.03.2019, 01.04.2019. The indices are calculated over these dates for each simulation of the sensitivity analysis, and the area average RMSE, hereafter referred to as RMSE, is used as the indicator to ascertain which setup is performing better. The statistical indices calculated are outlined in table 3.4, while the setup considered for the different simulations is specified in appendix D.

As illustrated in table 3.4, the simulation yielding the lowest RMSE is the one that incorporates the two finest sediments at the river mouths (14 and 32.5 μm) and the weighted solid discharge for the Savio and Reno rivers. The analysis is comprised of two setups, each employing Savio and Reno boundary conditions. The distinction between these setups lies in the methodology employed to calculate the solid discharge of the two rivers. Specifically, for the Savio and Reno rivers, the available data is limited to the total yearly solid load. Based on this information, it was determined that either a constant solid discharge or a weighted discharge would be utilised. The former method (SavioReno, as designated in the simulation nomenclature) employs a constant solid discharge throughout the year for both rivers. Specifically, a constant solid discharge of 31.43 and 27.69 kgs^{-1} is, respectively, utilised for Reno and Savio. In contrast, the latter method (SavioReno2) assigns a weight to the solid discharge based on the liquid discharge as reported in Raicich (1994)'s climatology.

An additional intriguing aspect that merits consideration is the observation of how the RMSE varies for differing horizontal sediment diffusion coefficients. Specifically, figure 3.3 presents a scatter plot of RMSE for the first six values of $K_{sed,h}$ used for the sensitivity. This figure enables the observation of the non-linear relationship between these two quantities, whilst simultaneously highlighting the minimal impact of this coefficient on the simulation outcome. The fluctuations observed in the RMSE are of the order of 10^{-5} $[kgm^{-3}]$. The results presented in figure 3.3 indicate that the optimal configuration is the one with a zero horizontal diffusion coefficient. This is due to the minimal improvement observed when using a different value and the simplification of the model's computation when setting it to zero.

As illustrated in figure 3.4, the RMSE maps for two simulations are presented: Event03_2sedfin and Event03_2sedfin_SavioReno2, from left to right. The sole distinction between the two configurations depicted in this figure is the incorporation of the sediment lateral boundary condition at the mouth of Savio and Reno (illustrated in figure 3.4 (b) by the two green arrows). The enhancement of the RMSE along the Emilia-Romagna coastline is discernible, particularly in the vicinity of the two estuaries. However, no such enhancement is observed in the vicinity of the Po Delta region.

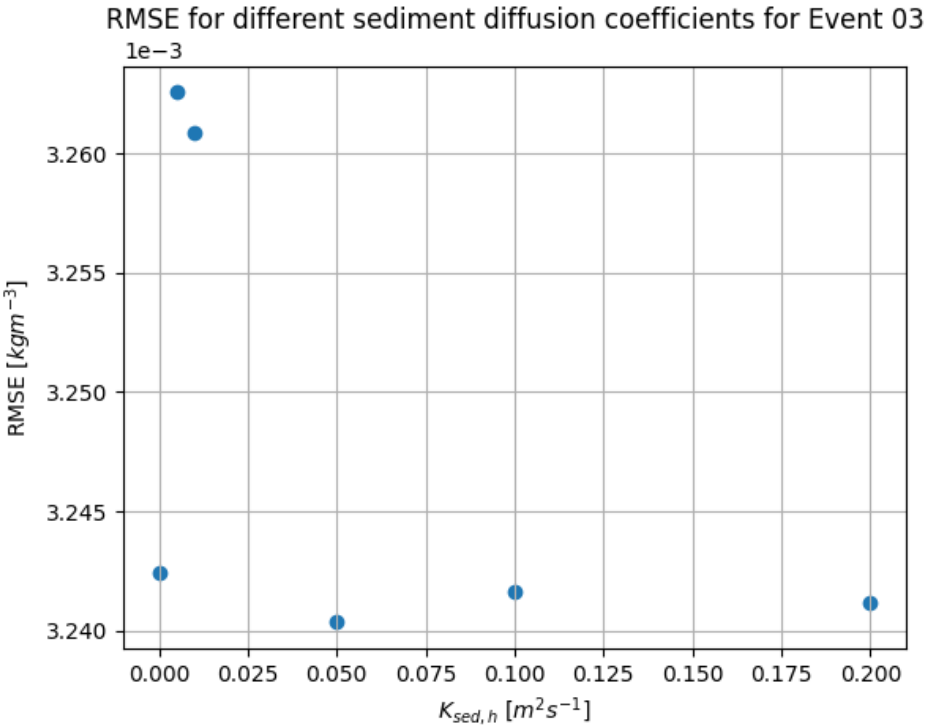

Figure 3.3: RMSE calculated for the sensitivity analysis conducted for the March wave event of 2019, incorporating various horizontal diffusion coefficients.

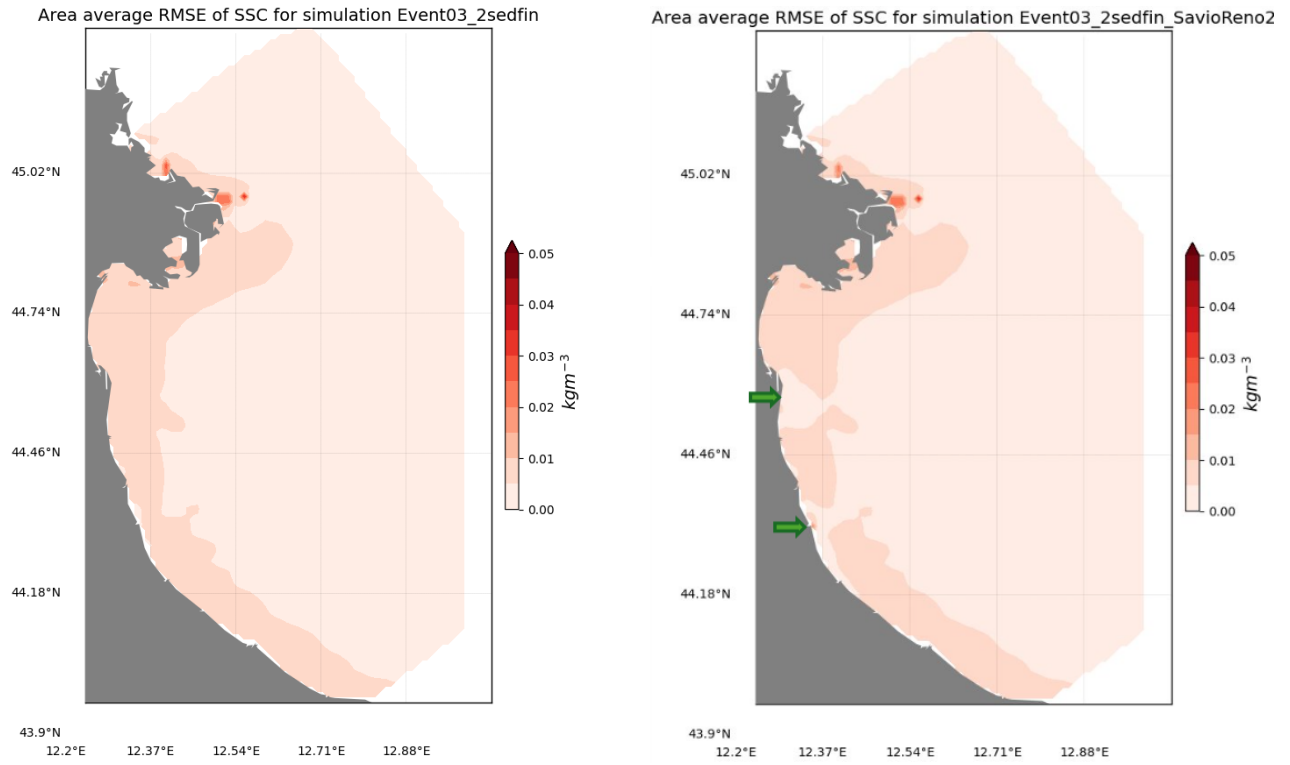

Figure 3.4: Comparison between the RMSE calculated for the simulation without (a) and with (b) the lateral sediment boundary condition at Savio and Reno rivers. The green arrows denote the Savio and Reno mouths.

To ascertain the actual discrepancy between the model results and the observations, it is necessary to consider the bias. Figure 3.5 provides an overview of the bias calculated for the optimal model setup. Specifically, figure 3.5 illustrates the bias associated with five dates, four of which are the ones used to calculate the RMSE. The calculation of the bias is outlined as follows:

$$bias = \phi_m^i - \phi_o^i \tag{3.4}$$

For all the i grid points. A negative bias indicates that the observations have higher concentrations than the model, while a positive bias indicates the opposite.

As illustrated in the various plots presented in figure 3.5, the model initially displays the most significant differences but subsequently improves over time. Of note is the initial plot (a), which is conducted after a period of ten hours since the initiation of the model's deployment. This outcome is anticipated, given that the simulation commenced with a zero concentration of suspended sediment in the entire study area. A notable observation is that the plot exhibiting the lowest RMSE corresponds to the date of the wave event, which occurred on the 25^{th} of March. This outcome is encouraging for the utilisation of waves calculated directly by SHYFEM-MPI,

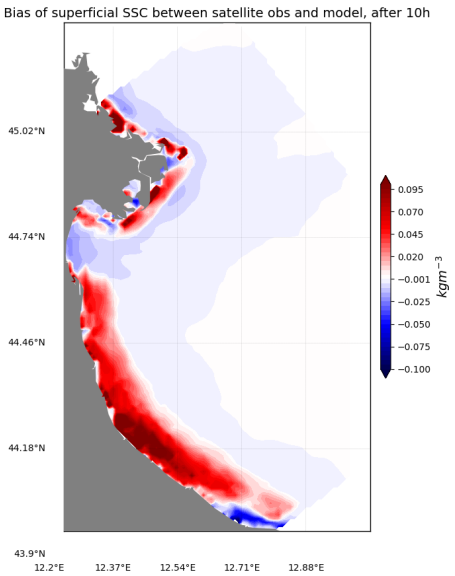

(a) Bias observed a on the 20^{th} of March 2019

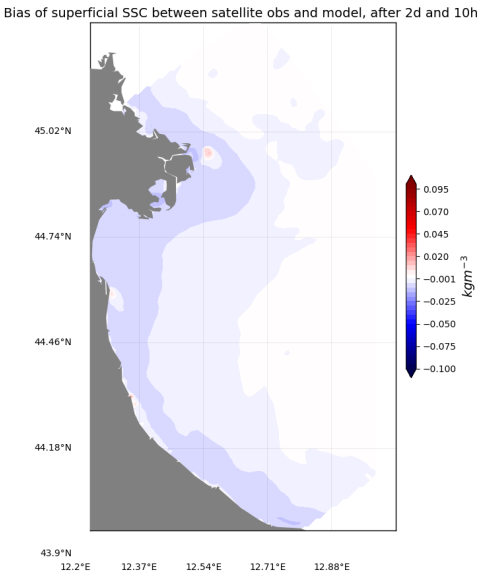

(b) Bias observed on the 22^{nd} of March 2019

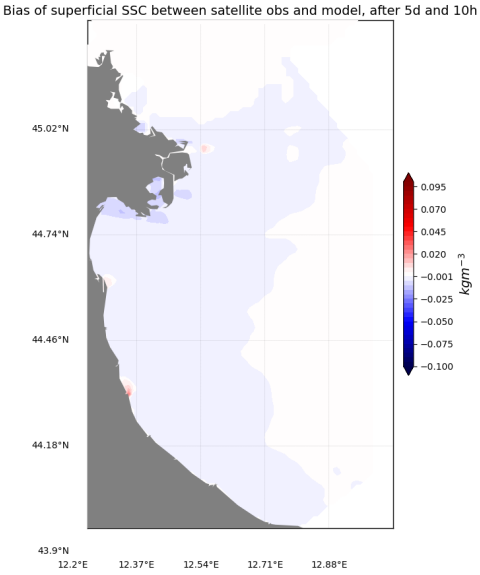

(c) Bias observed on the 25^{th} of March 2019

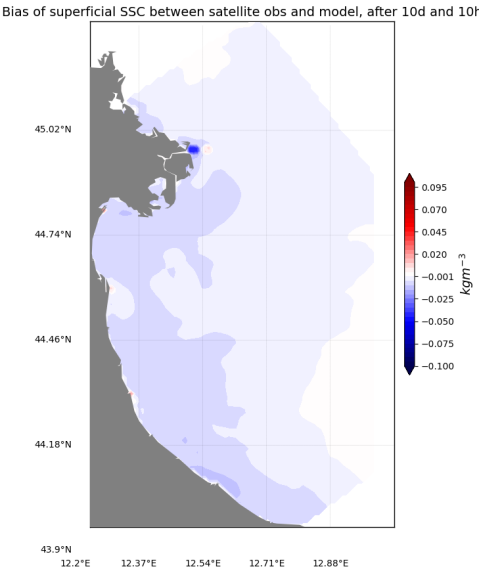

(d) Bias observed on the 30^{th} of March 2019

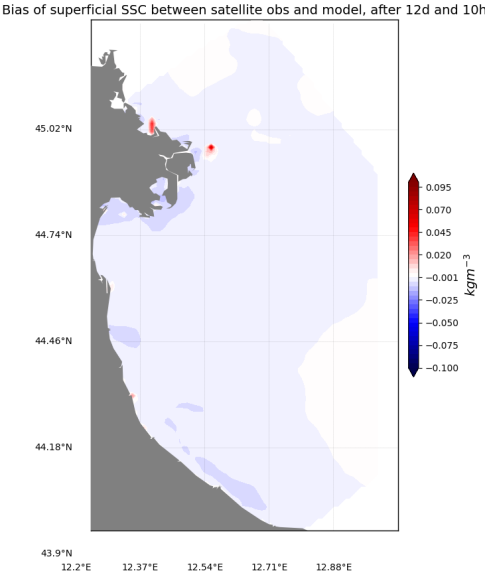

(e) Bias observed on the 1^{st} of April 2019

Figure 3.5: Comparative analysis of the bias between the model outputs and satellite data for five distinct dates. The dates utilised from (b) to (e), correspond to those employed in the calculation of the RMSE depicted in figure 3.4.

τ_c [Pa]	W_s calculation	sediment transport method	Sediment at rivers	waves	$K_{sed,h}$ $[m^2s^{-1}]$	ρ_s $[kgm^{-3}]$	SavioReno forcing
Calculated τ_c	Soulsby (1997)	Van Rijn et al. (1993)	2 finer (14 & 32.5μm)	Yes	0	2650	weighted

Table 3.5: The simulation setup yielding the most optimal outcome for the event in March 2019.

as this is the wave forcing employed in this study.

Based on all the information gathered during the sensitivity analysis, the optimal simulation setup for this wave event is identified as Event03_2sedfin_SavioReno2. The general overview of this setup is offered in table 3.5. The sole discrepancy from the initial simulation setup delineated in table 3.3 pertains to the incorporation of the Savio and Reno sediment forcing with the weighted sediment transport rate.

3.3.2 Po River flood

The second event under consideration for the sensitivity analysis is of a distinct nature, given that it pertains to the Po River flood of 2019.

For the simulations examining the flood event, the period under review extends from the 18^{th} of October to the 31^{st} of December 2019, although the flood is documented by Arpae from the 22^{nd} of November until the 3^{rd} of December. The decision to consider such a broad period is based on the daily discharge and the turbidity recorded at Pontelagoscuro. A close examination of the subsequent chapter's figures, specifically 4.1 and 4.2, reveals a discernible increase in both discharge and turbidity from the end of October. The former figure presents the daily discharges measured at Pontelagoscuro during 2019, while the latter illustrates the turbidity data for the corresponding period.

The calculation of the RMSE is based on five dates: 21.10.2019, 26.10.2019, 07.11.2019, 10.11.2019, 10.12.2019. These dates have been determined based on the list of available dates provided in the appendix C. Regrettably, there is an absence of viable satellite data during the flood event period as recognised by Arpae.

The table 3.6 provides an overview of the statistical indices calculated for the sensitivity simulations. In comparison to the RMSE values previously outlined in the preceding subchapter, the ones calculated here are higher. Specifically, they are double the values presented in table 3.4. The increase in RMSE can be attributed primarily to the significant impact of flood events on suspended sediment concentrations, particularly within a Delta region. During floods, ad-

Simulation	RMSE $[kgm^{-3}]$, 10^{-3}	MAE $[kgm^{-3}]$, 10^{-3}	R [-], 10^{-1}
Event10_4tauin	6.3255	2.3607	1.2716
Event10_tauin0.02	6.3255	2.3607	1.2716
Event10_Stokes	6.3101	2.3605	1.2829
Event10_ENGHAN	1031.0	21.625	0.8151
Event10_2sed	6.3947	2.3603	1.3986
Event10_2sedfin	6.3215	2.2860	2.4258
Event10_nowaves	6.2407	2.3541	1.5917
Event10_sedhpar0.005	6.3374	2.3610	1.2436
Event10_sedhpar0.01	6.3184	2.3600	1.2856
Event10_sedhpar0.05	6.3343	2.3612	1.2488
Event10_sedhpar0.1	6.3213	2.3599	1.2722
Event10_sedhpar0.2	6.3168	2.3597	1.2735
Event10_sedhpar1	6.2431	2.3522	1.5093
Event10_rhos1800	8.5417	2.4751	1.1402
Event10_2sedfin_SavioReno	6.7776	2.3110	1.6787
Event10_2sedfin SavioReno2	6.2983	2.2765	2.3999

Table 3.6: Statistical indices calculated for the various setups in relation to the flood event.

ditional input areas for sediments may be present (e.g. river overflow from the Delta or newly formed streams due to high water levels), and the sediment forcing used as a boundary condition may have a higher error, since it is collected during an extreme event, making it more difficult to obtain an adequate sample. The various setups employed, along with their respective designations, are delineated in the appendix D.

As demonstrated in table 3.4, the initial critical stress of the sediment classes does not result in any alterations to the RMSE. Conversely, in contrast to the preceding sensitivity analysis, the optimal configuration for this event appears to be the one devoid of waves (Event10_nowaves), with the configuration involving a diffusion coefficient equal to one ranking second. The optimal configuration identified in the previous sensitivity analysis (Event03_2sedfin_SavioReno2) is surpassed as the third best configuration for the flood event. A notable finding of this sensitivity analysis is the significant discrepancy in the use of the method outlined in Engelund and Hansen (1967) for sediment transport calculation, a discrepancy that was not identified in the preceding analysis.

As illustrated in figure 3.6, the three RMSE maps, calculated for the three optimal setups of this sensitivity analysis, are presented. A close examination of the three maps reveals that the Po River Delta region exhibits the highest levels of error across all three setups. The initial two

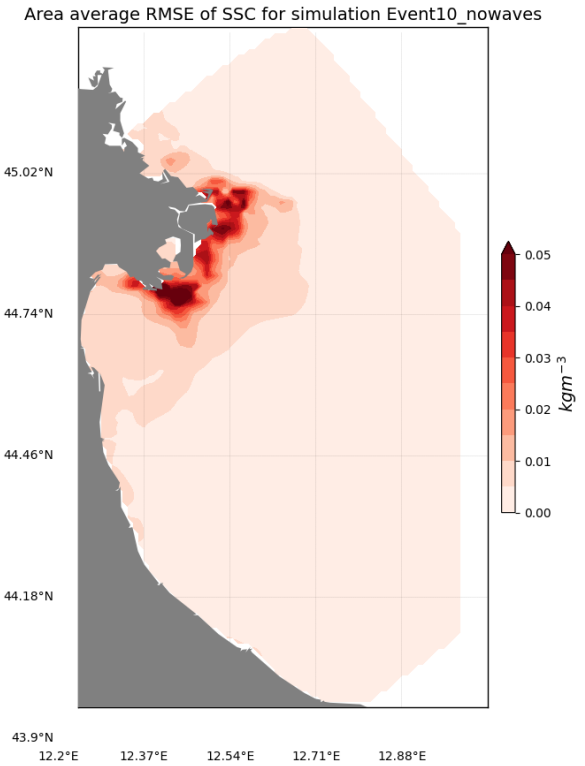

(a) RMSE calculated for the simulation in the absence of waves

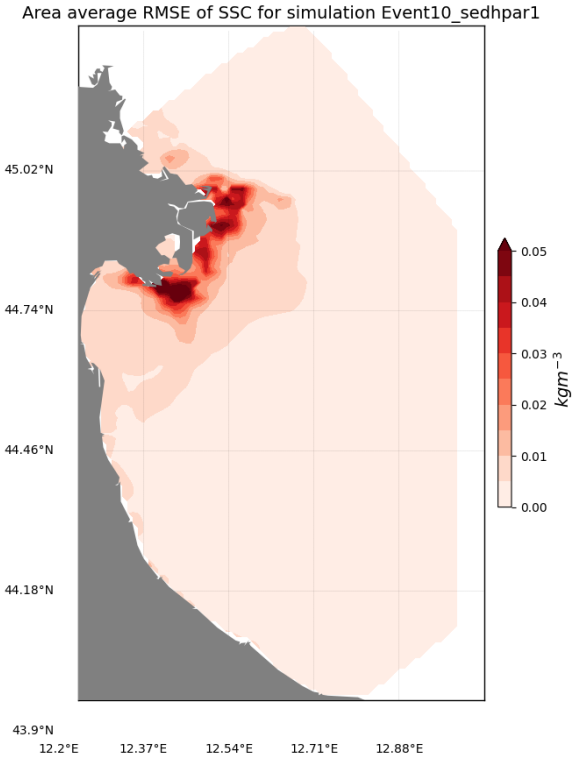

(b) RMSE of the simulation with the horizontal diffusion coefficient set at one

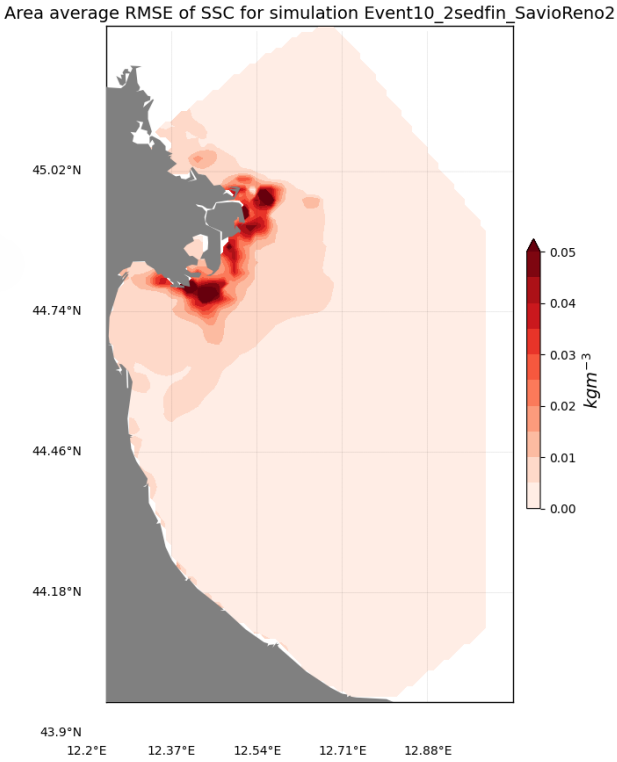

(c) RMSE of simulation incorporating sediment forcing at the Savio and Reno mouths, with the weighted solid discharge

Figure 3.6: Comparison of the RMSE calculated for the three optimal configurations of the 2019 flood event.

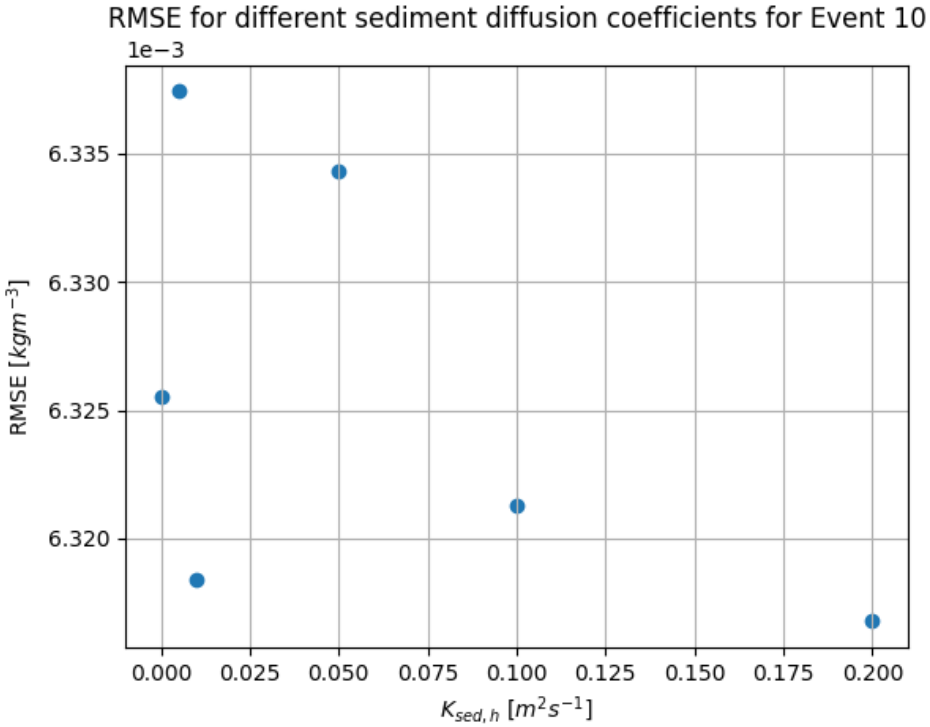

Figure 3.7: RMSE calculated for the sensitivity analysis conducted for the 2019 flood event, taking into account various values of the horizontal diffusion coefficient.

configurations (illustrated in (a) and (b)) demonstrate slightly enhanced representation of the SSCs surrounding the Po mouths, particularly the Busa di Dritta, while the third configuration (depicted in map (c)) exhibits superior representation along the coastline and a conspicuously diminished RMSE in the vicinity of the Reno mouth.

To corroborate the preceding finding of a non-linear correlation between the RMSE and the horizontal diffusion coefficient for sediments, figure 3.7 demonstrates the RMSE calculated for the initial six values of $K_{sed,h}$. As was previously established, the alteration in the horizontal diffusion coefficient elicits negligible alterations in the RMSE (persisting at the level of 10^{-5}). Consequently, it was determined that the designation of zero as the optimal configuration would serve to streamline the computational procedures.

The optimal model configuration is determined to be the configuration devoid of waves, as illustrated in table 3.7. This outcome can be rationalised by the fact that the model's waves are

τ_c [Pa]	W_s calculation	sediment transport method	Sediment at rivers	waves	$K_{sed,h}$ [m^2s^{-1}]	ρ_s [kgm^{-3}]	SavioReno forcing
Calculated τ_c	Soulsby (1997)	Van Rijn et al. (1993)	2 finer ()14 & 32.5μm	No	0	2650	x

Table 3.7: The simulation setup yielding the most optimal outcome for the 2019 flooding event.

τ_c [Pa]	W_s calculation	sediment transport method	Sediment at rivers	waves	$K_{sed,h}$ $[m^2s^{-1}]$	ρ_s $[kgm^{-3}]$	SavioReno forcing
Calculated τ_c	Soulsby (1997)	Van Rijn et al. (1993)	2 finer (14 & 32.5μm)	Yes	0	2650	weighted

Table 3.8: Configuration employed for the one-year simulation, derived from sensitivity analysis conducted for two distinct events in 2019.

derived using a highly simplified method that does not consider numerous wave effects that are significant for sediment transport, such as wave breaking. Furthermore, during periods of low wind intensity, wave calculations are known to be more prone to error, and it is reasonable to expect that the errors inherent in a simplified model such as this will be even more pronounced. This hypothesis is corroborated by the validation of the wave model conducted in the preceding chapter, wherein it is evident that the wave field modelled by the model significantly deviates from the observations during the period in question.

3.4 Summary of the sensitivity results

Tables 3.5 and 3.7 offer an overview of the setups that give the lowest RMSE for the two periods considered in the sensitivity analysis.

Sediment transport is driven by a range of factors, including waves, which cannot be neglected in this context. Consequently, the configuration presented in table 3.7 is deemed an unsuitable option for a long-term simulation of sediment transport.

The optimal overall configuration, as determined by a sensitivity analysis, involves the imposition of forces on the most fine-grained sediment classes at the river mouths, in conjunction with the utilisation of a weighted solid discharge for the Savio and Reno rivers. Considering these findings, it is determined that the configuration will be maintained for the one-year simulation. The configuration that has been determined to be optimal for the one-year simulation is outlined in table 3.8.

The subsequent chapters are devoted to the one-year simulation of this project.

Chapter 4

One-year simulation

4.1 Study period

The temporal framework of this research pertains to the availability of data on river discharge and turbidity at Pontelagoscuro. Of the two datasets under consideration, the one pertaining to turbidity is the more limited in terms of temporal scope. As specified in the previous subchapter (number 2.2.1), the available turbidity data is from 2011 to 2020. It is also noteworthy that

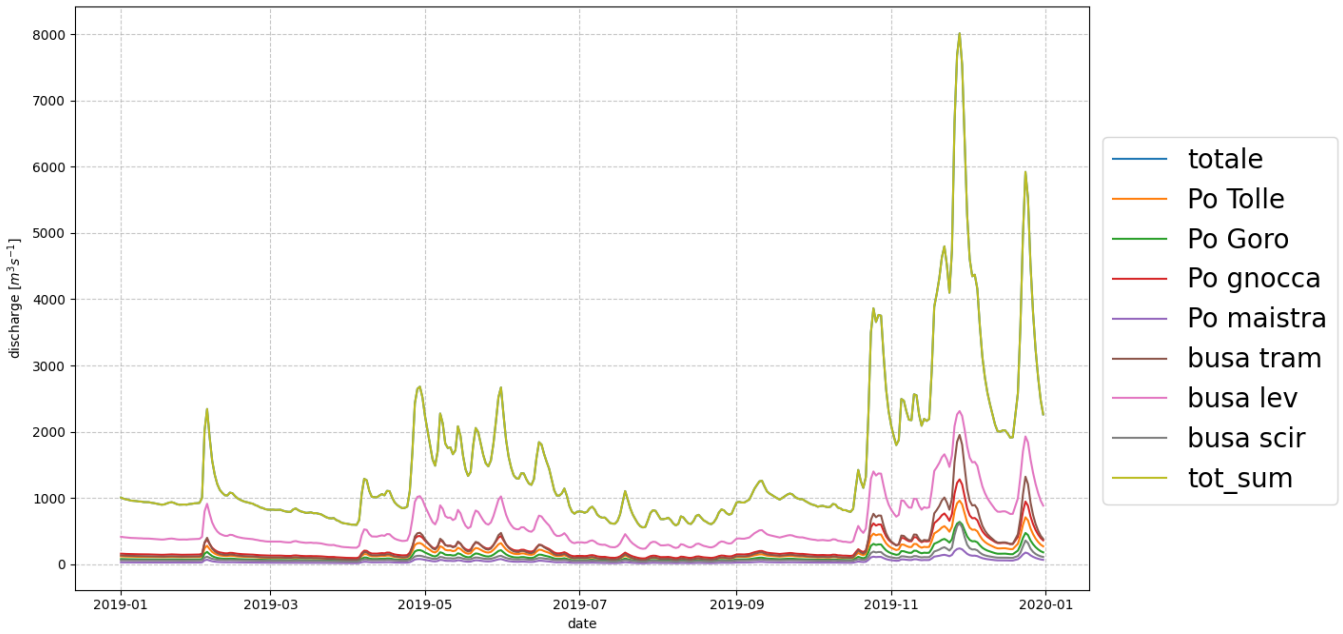

Figure 4.1: Discharge data at Pontelagoscuro station for the year 2019, including the division of this data between the various Delta branches.

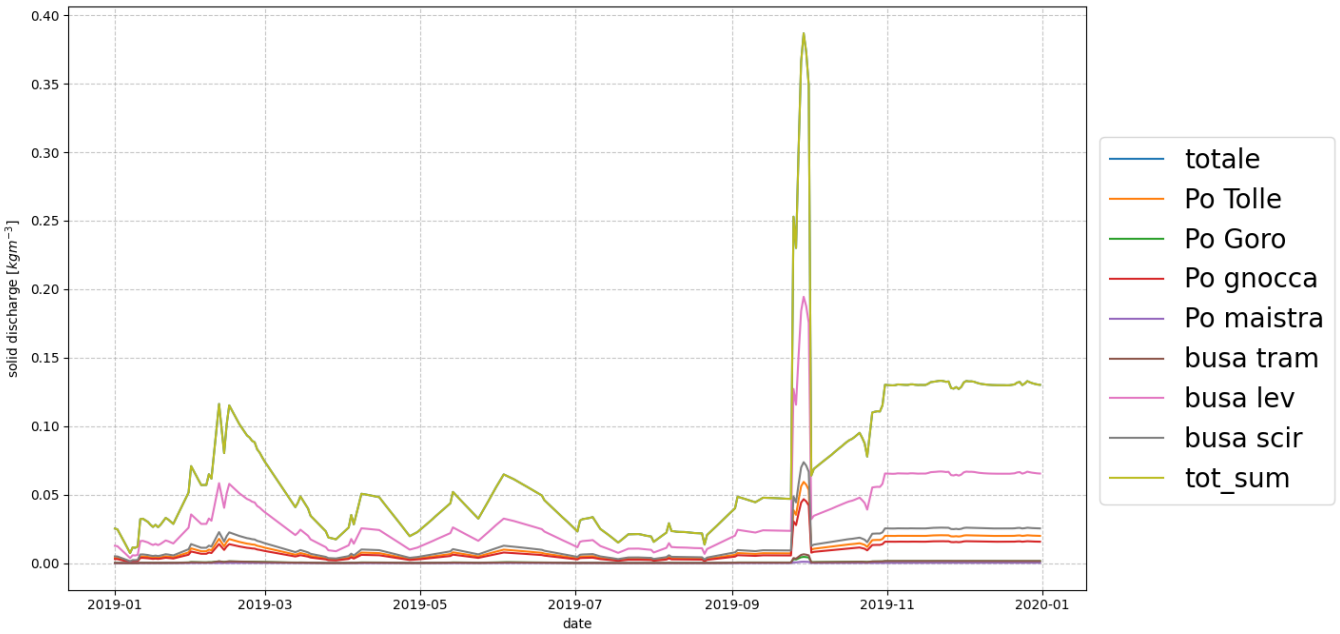

Figure 4.2: The suspended sediment concentration measured at the Pontelagoscuro station over the course of the year 2019, with the concentration of suspended sediment being divided into different Delta branches.

during this interval, maintenance of the Pontelagoscuro measuring station was undertaken in 2018. This intervention resulted in the absence of data from 25.07.2018 to 28.10.2018. Consequently, it was determined that the study period would span the year 2019. This is the most recent year for which turbidity data is available, and it is also notable that the Po River experienced a flood event during the winter period. Specifically, the Po discharge at Pontelagoscuro station reached 8000 m^3s^{-1}, whereas the average discharge is 1480 m^3s^{-1} (Correggiari et al., 2005). The daily mean discharge measured at Pontelagoscuro station for 2019, and the subsequent partitioning between the different mouths, is presented in figure 4.1, while the respective suspended sediment concentrations are shown in figure 4.2.
An overview of all events that occurred in 2019 in the Emilia-Romagna region is offered in Arpae's annual report Pavan and Marletto (2020). This report summarises the meteorological, hydrological and climate events that affected the region during the specified year.

In the ensuing sections, three types of model outputs are exhibited and elucidated. The initial section concentrates on the SSC, the subsequent section focuses on the mean grain size at the sea bottom, and the last section focuses on the erosion and deposition height of the seabed.

4.2 Suspended Sediment Concentration

The present section is concerned with the provision of an overview of the SSCs given by the one-year simulation with the model setup summarised in table 3.8. The primary objective is to ascertain whether the model is capable of accurately reproducing the SS patterns along the coast.

Prior to the presentation of the results of the SSCs, it is pertinent to ascertain whether the RMSE of this extended simulation has improved from the values obtained in the sensitivity analysis. The comparisons are presented in figure 4.3 for the wave event and in figure 4.4 for the flood event. Both figures present the maps derived from the sensitivity analysis and the one-year simulation, accompanied by their respective area average RMSE. Furthermore, they illustrate the discrepancy between the two RMSE maps. The third plot is particularly noteworthy in this regard, as it illustrates the areas where the model results have shown enhancement in the one-year simulation (green areas) as compared to the areas where no such enhancement has been observed (pink areas). A clear improvement in the model's performance for the wave event is evident in the longer run (see figures 4.3 a and b), in comparison to the flood period. The difference maps reveal that for the wave event, green areas are more prominent along the coastline, while for the flood event, pink areas (indicative of deteriorating model performance) are more prevalent, particularly in the vicinity of the Po Delta. A general improvement is evident in both cases when considering the one-year simulation, as highlighted by the area average RMSE value being smaller for the one-year results.

To provide an overview of the SSCs results given by the model, it was decided to utilise monthly mean values, which were then compared to the monthly mean values of the satellite data. Additionally, a bias is calculated between these two means to identify areas where higher errors are present and to ascertain whether the model is overestimating or underestimating the SSCs. It should be noted that the representation of only monthly means precludes the full variability of suspended sediment concentrations. However, this method is regarded as an effective means of ascertaining the model's capacity to replicate observed SSC patterns. The calculation of monthly means and the subsequent bias is conducted for all months; however, in this thesis, it is decided to present only a limited number. This decision was taken since by looking at the results of each month, it was possible to recognise similar patterns and observa-

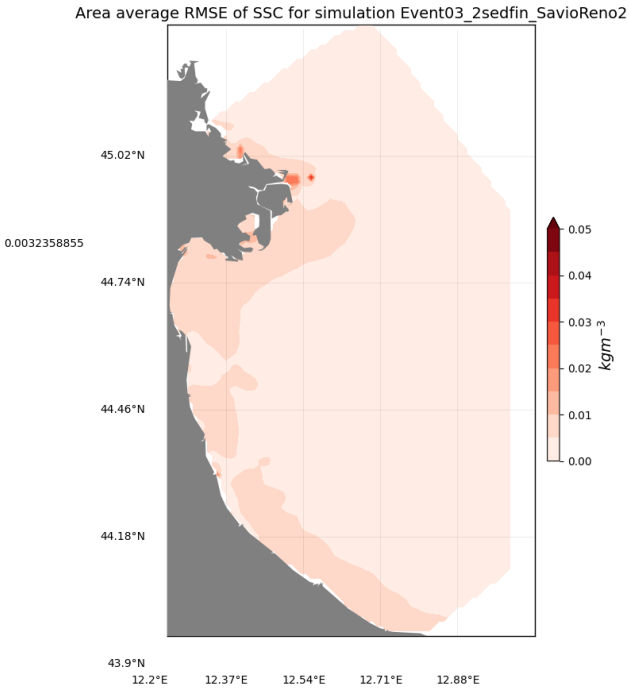

(a) RMSE of the sensitivity analysis simulation for the wave event

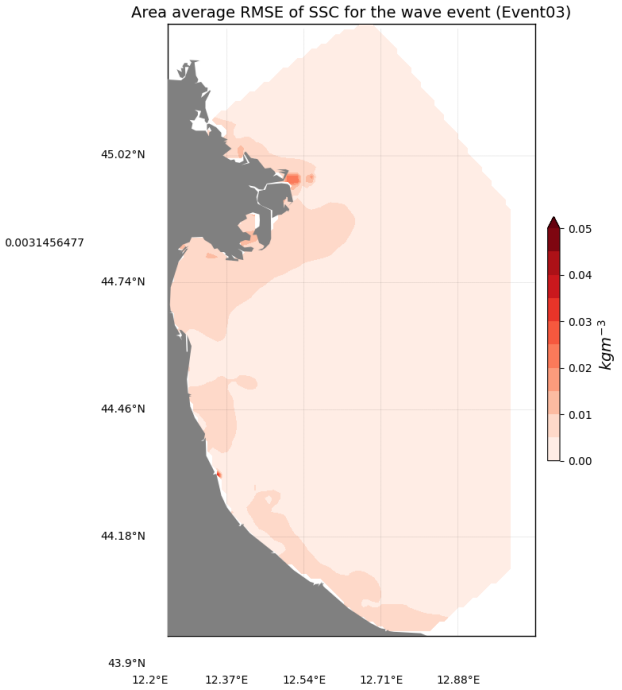

(b) RMSE of the one-year simulation for the wave event

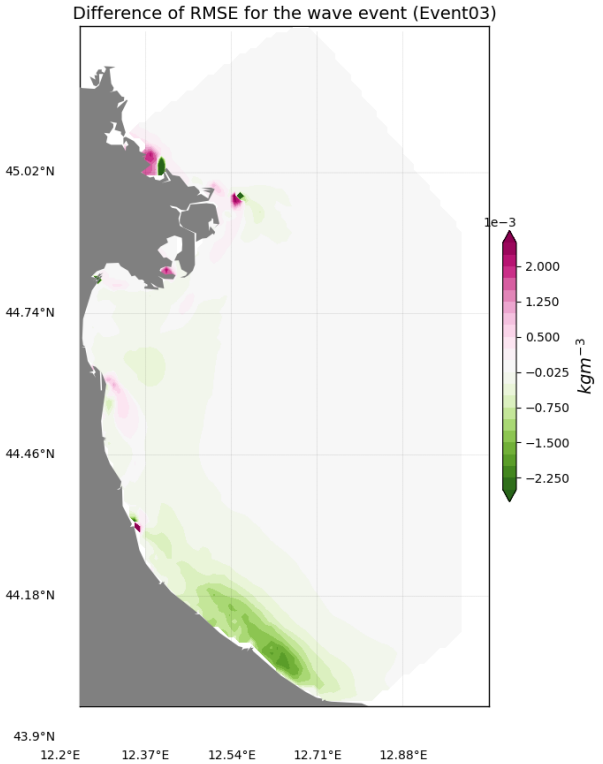

(c) Bias between the one-year and the sensitivity analysis RMSE for the wave event [plot (b)- plot (a)]

Figure 4.3: Comparison made between the RMSE of the one-year run results (plot (b)) and the best simulation for the sensitivity analysis carried out in chapter 3 for the wave event in March (plot (a)). In these two plots, the area average RMSE is specified on the left side of the map. The difference between these two maps is illustrated by plot (c).

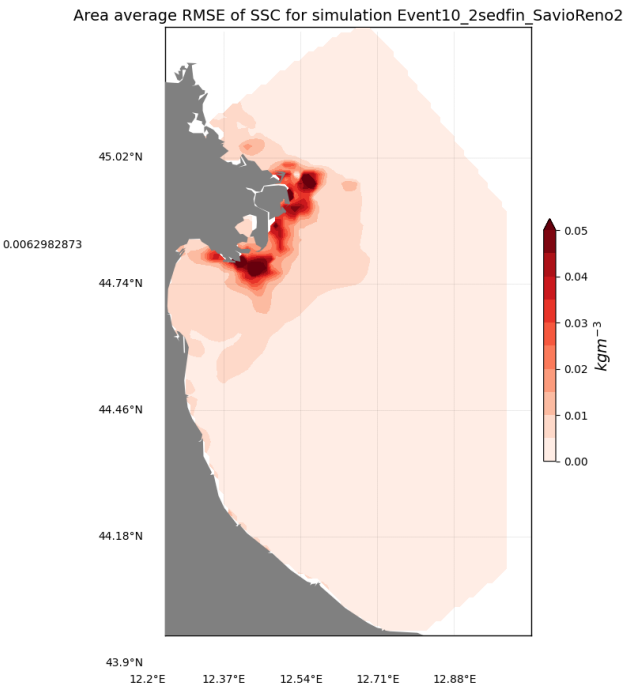

(a) RMSE of the sensitivity analysis simulation for the flood event

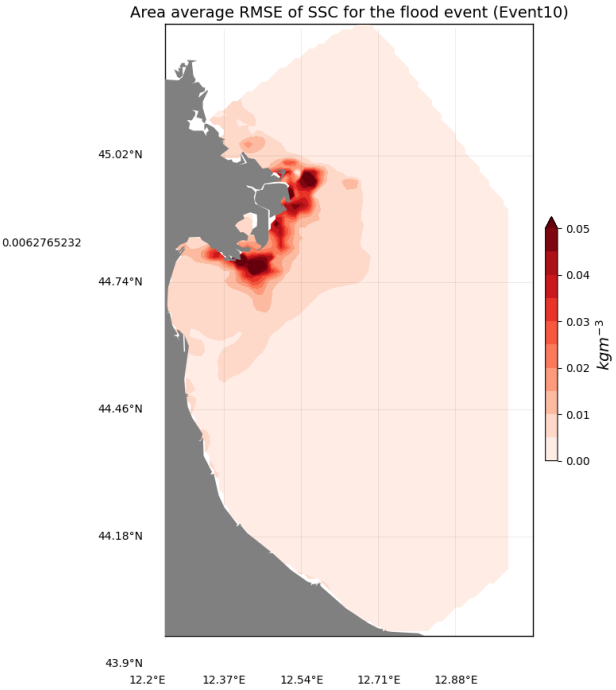

(b) RMSE of the one-year simulation for the flood event

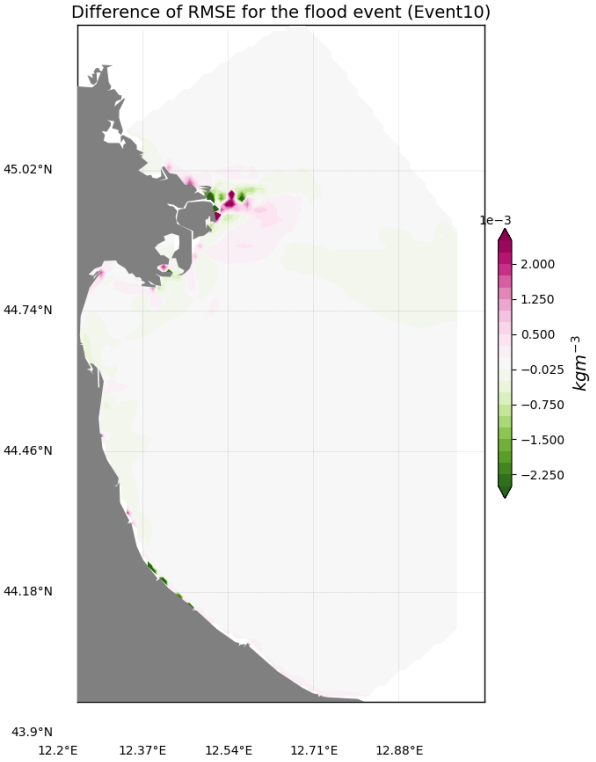

(c) Bias between the one-year and the sensitivity analysis RMSE for the flood event[plot (b)- plot (a)]

Figure 4.4: Comparison between the RMSE of the one-year run results (plot (b)) and the best simulation for the sensitivity analysis carried out in chapter 3 for the flood event (plot (a)). In these two plots, the area average RMSE is specified on the left side of the map. The difference between these two maps is illustrated by plot (c).

tions for months of the same season. Consequently, a single month per season is designated as the representative one, with February representing Winter, May representing Spring, August representing Summer, and October representing Autumn. In addition to these four months, the performance of the model under flood conditions is also presented for November and Decembre. It is noteworthy that all maps depicting SSCs utilise a logarithmic colour scale, while the bias maps no. The use of a logarithmic colour scale is explained by the fact that sediment concentration in the water column is normally low, so this type of colour map will show better the patterns present.

The initial maps presented for the SSCs are those depicted in figure 4.5. These maps, which are calculated for February, are presented as a representation of the winter period. As is evident in the first two maps, the model demonstrates an ability to replicate the concentration pattern along the coast, albeit with lower values in comparison to the observed data. However, the model concentrations are higher than the observations in front of the three mouths of Po di Pila, especially in front of Busa di Dritta, and in front of Po di Maistra mouth. One potential explanation for this discrepancy could be attributed to the application of an incorrect sediment load at these specific locations. Conversely, the areas in proximity to the open boundary exhibit minimal or no suspended sediment, a phenomenon that contrasts with the observations. The lower SSCs observed in these areas can be attributed to the absence of a lateral boundary condition for sediments forced at the ocean boundary. This absence can be attributed to the paucity of measurements and data regarding suspended sediments in the open ocean, which hinders the generation of a viable lateral boundary condition for the model. Other potential explanations for this discrepancy may include the presence of extremely low concentrations of particularly fine sediments that are permanently suspended and cannot be addressed by the model, or the recognition of other suspended material (e.g. organic matter, chlorophyll) as SS by the satellite. The bias map (c) substantiates these observations, yet it demonstrates that the discrepancy at the open boundary is not as pronounced as anticipated from the analysis of plots (a) and (b). This latter consideration lends further support to the hypothesis that there might be exceptionally fine particles, permanently suspended, throughout the domain.

The second maps, presented in figure 4.6, are calculated over the month of May and are used to represent the Spring period. A notable similarity is observed between these maps and their

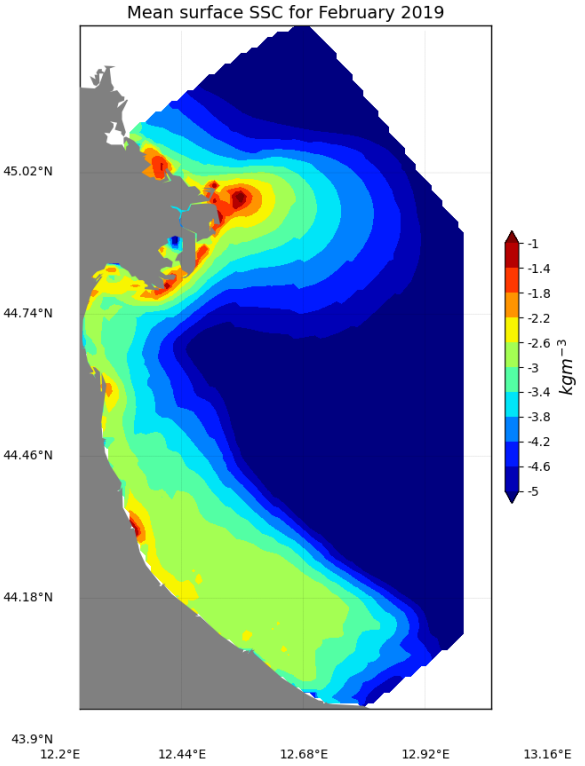

(a) Model result provided for the mean SSC in February 2019

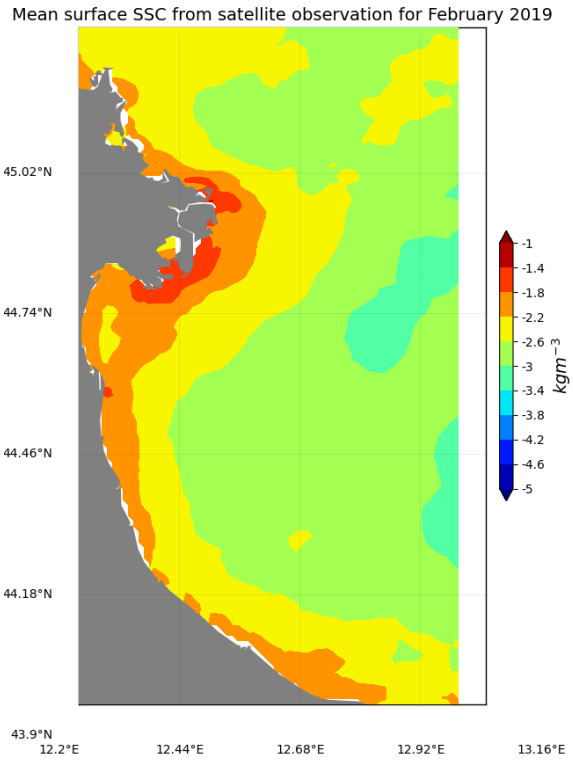

(b) Mean SSC in February 2019 calculated from satellite data

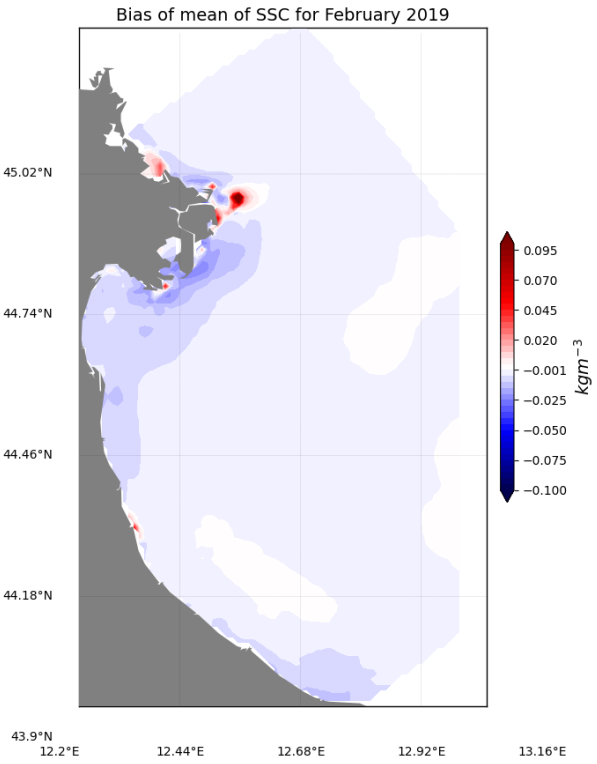

(c) Bias between the findings of the model and observations

Figure 4.5: Mean surface SSC for February 2019, along with its associated bias. For plot (a) and (b), a logarithmic colormap has been employed.

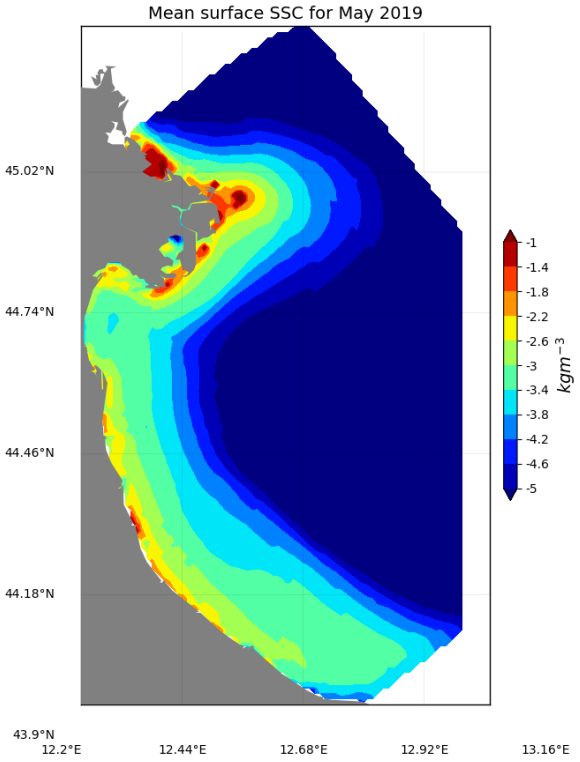

(a) Model result provided for the mean SSC in May 2019

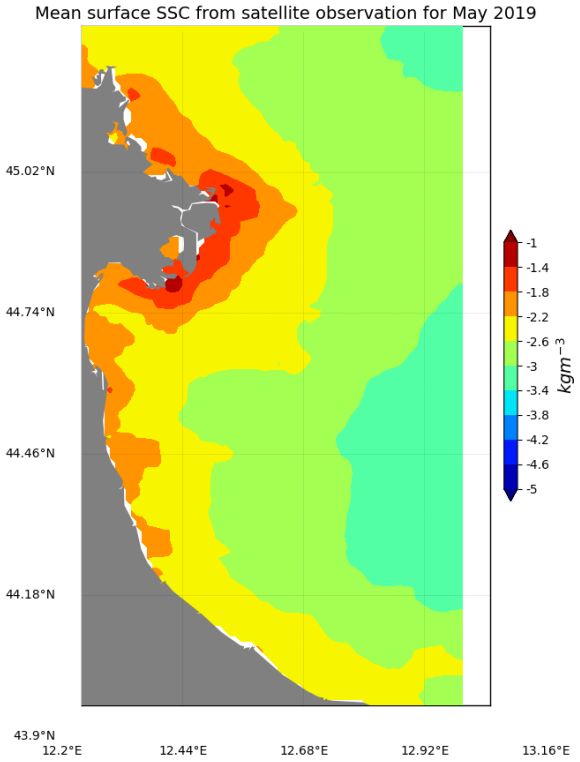

(b) Mean SSC in May 2019 calculated from satellite data

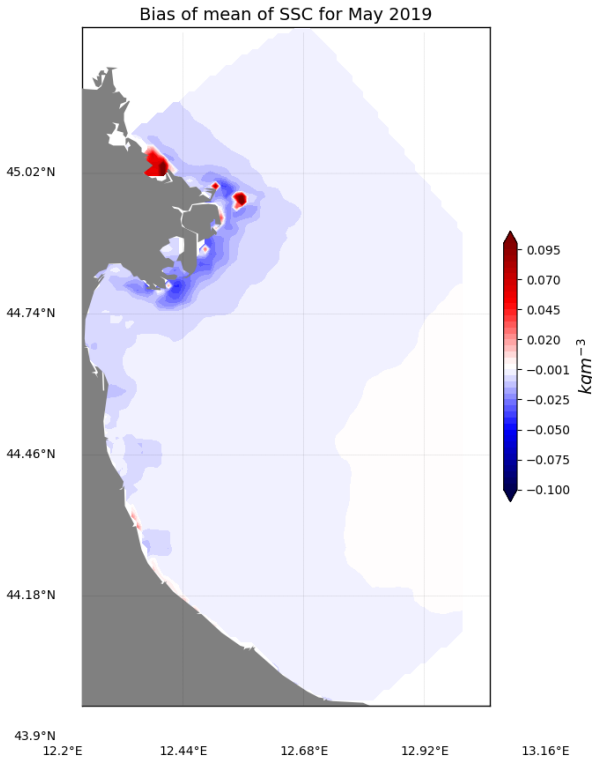

(c) Bias between the findings of the model and observations

Figure 4.6: Mean surface SSC for May 2019, along with its associated bias. For plot (a) and (b), a logarithmic colormap has been employed.

predecessors, thus enabling the repetition of the same observations. The only discernible difference is the higher bias in the Po Delta area, where the observed SSCs are higher than the modelled ones and the bias is visibly lower than in figure 4.5 (c), particularly in the southern part of the Delta region.

When both figures 4.5 and 4.6 are considered, it is noteworthy that both the model and the observations exhibit an area with lower SSC in front of the Sacca di Goro. This observation serves to reinforce the model's capacity to reproduce SSC patterns along the coast.

In the context of the summer period, figure 4.7 provides a representation of the three maps calculated for the month of August. Upon examination of plots (a) and (b), it is immediately evident that there has been a decrease in concentrations for both the model and the observations. It is evident from this that the along-shore pattern of suspended sediment is no longer reflected in the model, despite the bias plot exhibiting lower values than previously observed, extending across the entire study area. The bias plot reveals that the model concentrations are elevated in the vicinity of the Busa di Dritta and the Po di Maistra mouths. The general lower concentrations can be explained by the lower river discharges during summer, while the extremely low concentrations for the model results can be explained by the presence of biological cycles and changes in sediment erodibility, due to benthic organisms (Stevens et al., 2007). In summary, the model demonstrates no discernible SSC pattern along the coastline during the summer months.

The autumn period is denoted by the month of October, and the maps are displayed in figure 4.8. It is evident that the outcomes derived for the Autumn period bear a resemblance to those observed in the Winter period, wherein the alongshore concentration pattern remains consistent, exhibiting lower concentrations compared to the observed values, and the bias surrounding the Po Delta is less pronounced than that seen in the Spring period. Notably, the model consistently exhibits elevated concentrations in the same areas, indicating an error in the sediment or discharge boundary conditions imposed at these mouths. As previously mentioned, the suspended sediment forcing measured at Pontelagoscuro is divided between the different Po mouths using the percentages specified by Correggiari et al. (2005). For discharges, the partitioning between the different mouths is done using Zasso and Settin (2012).

In addition to representing the four seasons, the flood period SSC patterns are presented. Specif-

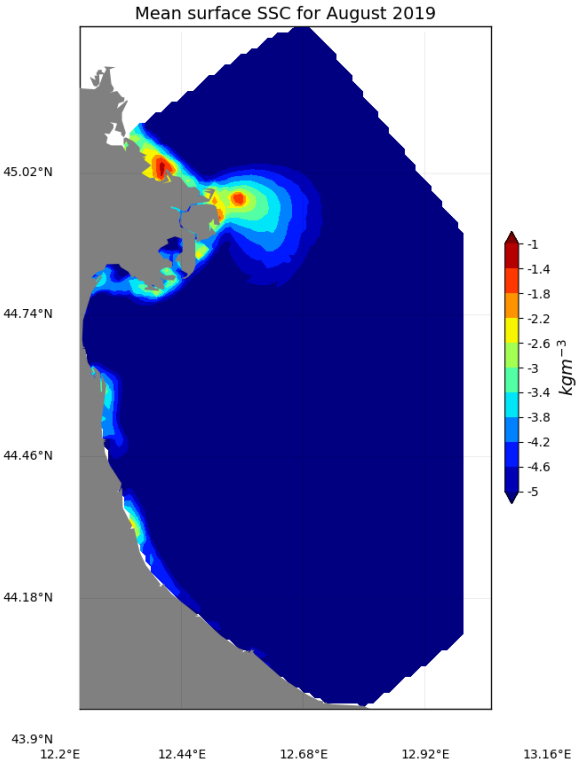

(a) Model result provided for the mean SSC in August 2019

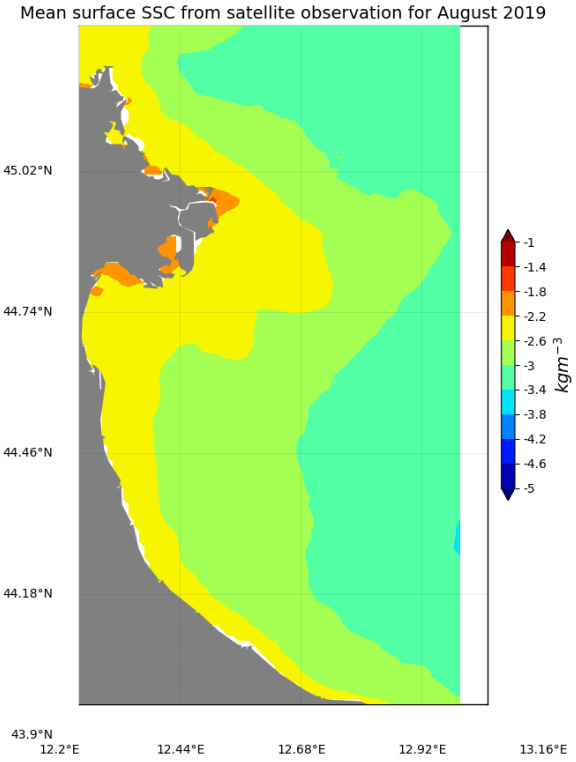

(b) Mean SSC in August 2019 calculated from satellite data

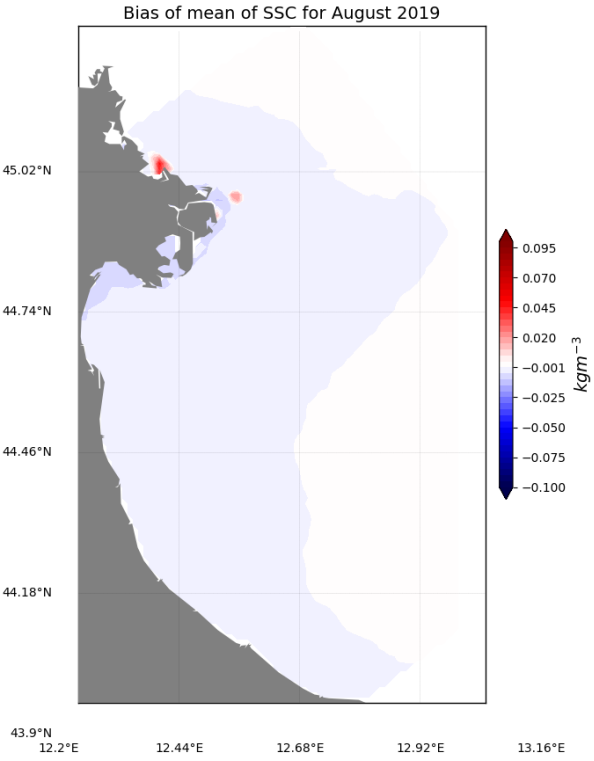

(c) Bias between the findings of the model and observations

Figure 4.7: Mean surface SSC for August 2019, along with its associated bias. For plot (a) and (b), a logarithmic colormap has been employed.

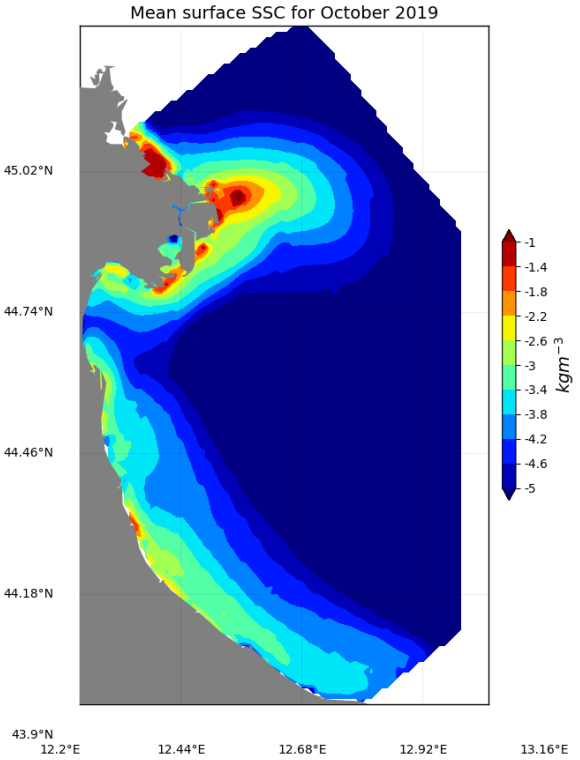

(a) Model result provided for the mean SSC in October 2019

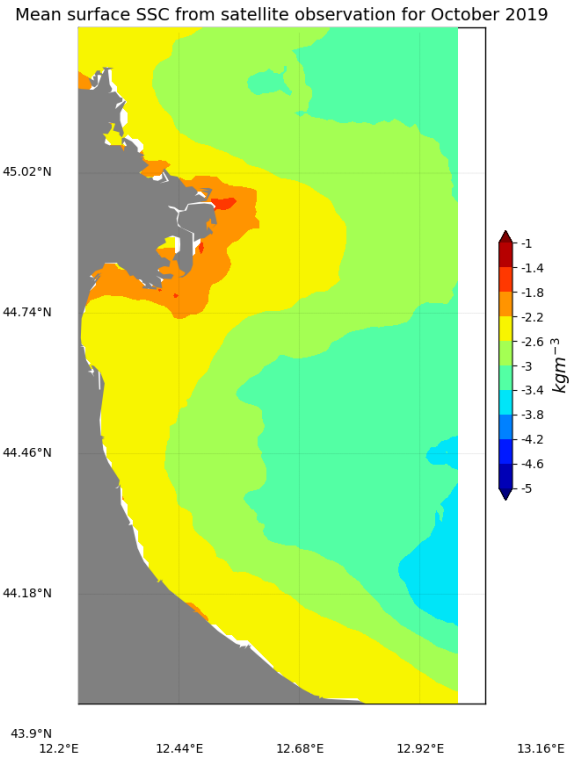

(b) Mean SSC in October 2019 calculated from satellite data

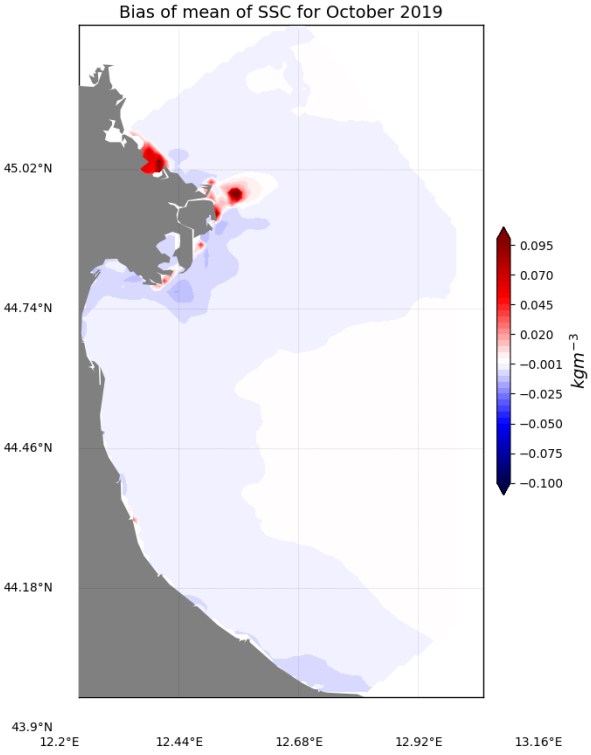

(c) Bias between the findings of the model and observations

Figure 4.8: Mean surface SSC for October 2019, along with its associated bias. For plot (a) and (b), a logarithmic colormap has been employed.

ically, figures 4.9 and 4.10 illustrate the SSCs for November and December of 2019, respectively. A notable observation from the model results is the augmentation in both the concentration and the area of the Po sediment plume, as anticipated during a flood period. The modelled plume is tilted towards the south, as highlighted by the observed concentrations. However, the model overestimates the deposition of suspended sediments, as the plume is constrained near the mouths and along the coastline, exhibiting high concentrations, while observations reveal a more expansive plume, with lower concentrations, particularly at the river mouths and along the southern coast of the Po Delta. The model's elevated sedimentation can be attributed to several factors, but the primary cause is likely the inaccurate representation of wave action. Wave calculations performed by SHYFEM-MPI do not incorporate wave breaking, a process that is widely acknowledged as being particularly significant in terms of resuspending sediments. This is because wave breaking affects the bottom shear stresses and generates turbulence (Cavaleri et al., 2012; Wu et al., 2011; Warner et al., 2008). Freshly deposited sediment is more susceptible to resuspension due to its increased porosity (Stevens et al., 2007). In addition to the lower concentrations and the high deposition rate of the model, these two figures illustrate the significance of sediment input from the northern lateral boundary, particularly evident in the November observations of plot (b). The model's ability to replicate the observed plume pattern is noteworthy, and the distinction between normal conditions and the flood event is clearly discernible, which is advantageous for future developments.
The model demonstrates a satisfactory reproduction of the alongshore pattern of SSCs, which is identified as the predominant transport direction in low-energy environments (Fain et al., 2007). The only months during which this pattern becomes undetectable are the summer months, a consequence of the seasonal erodibility of sediments and the development of benthic diatoms (Milligan and Cattaneo, 2007).

Prior to progression to subsequent chapters, an overview of the Secchi depths utilised for the model SSC calculations is provided in figure 4.11. As previously mentioned, the Secchi depth is utilised to ascertain the number of vertical levels to be considered in the calculation of the SSC of the model result, which is then compared to the satellite observation. A close examination of the various plots reveals two notable observations. Firstly, the shore parallel pattern of the Secchi depth during the four months used as normal conditions (plots from (a) to (d)) is not

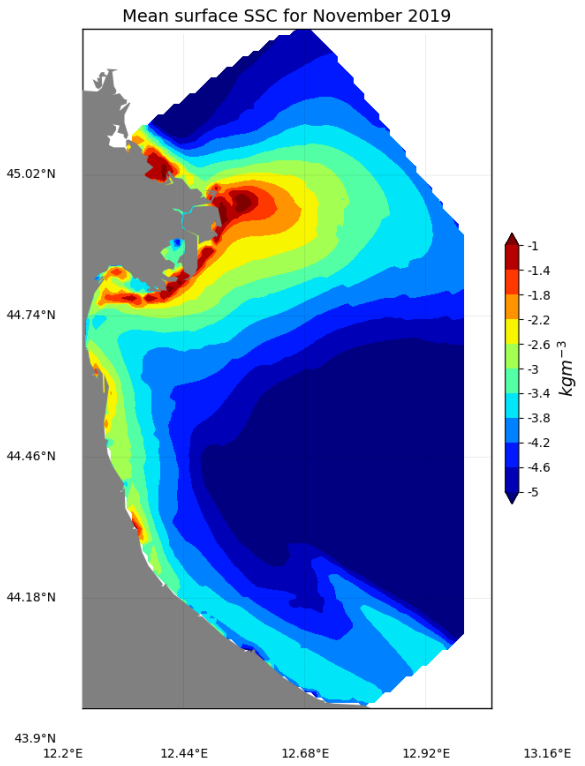

(a) Model result provided for the mean SSC in November 2019

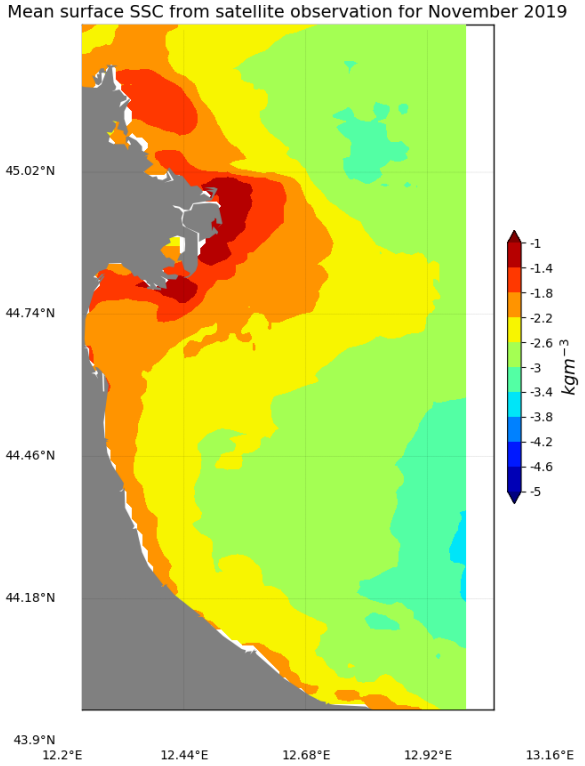

(b) Mean SSC in November 2019 calculated from satellite data

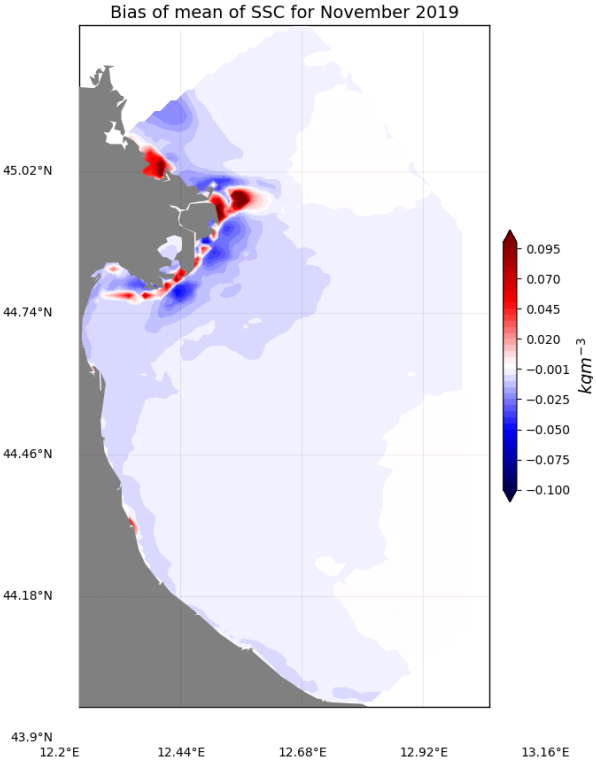

(c) Bias between the findings of the model and observations

Figure 4.9: Mean surface SSC for November 2019, along with its associated bias. For plot (a) and (b), a logarithmic colormap has been employed.

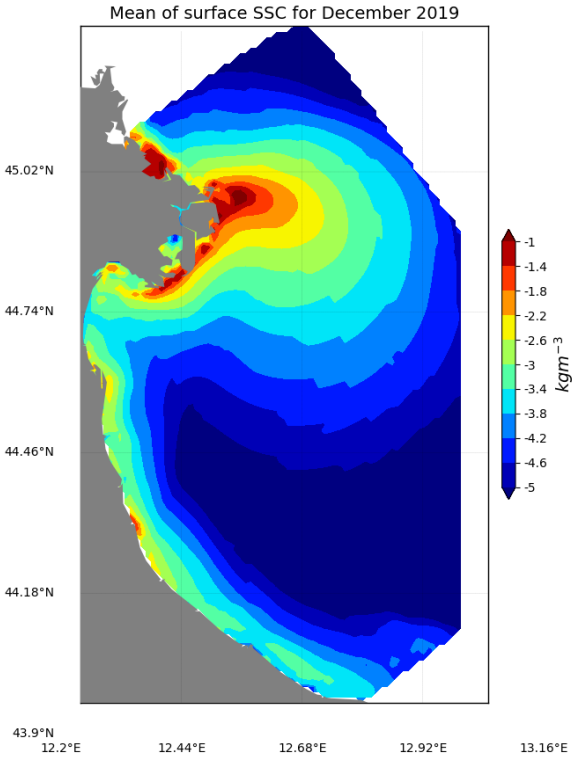

(a) Model result provided for the mean SSC in December 2019

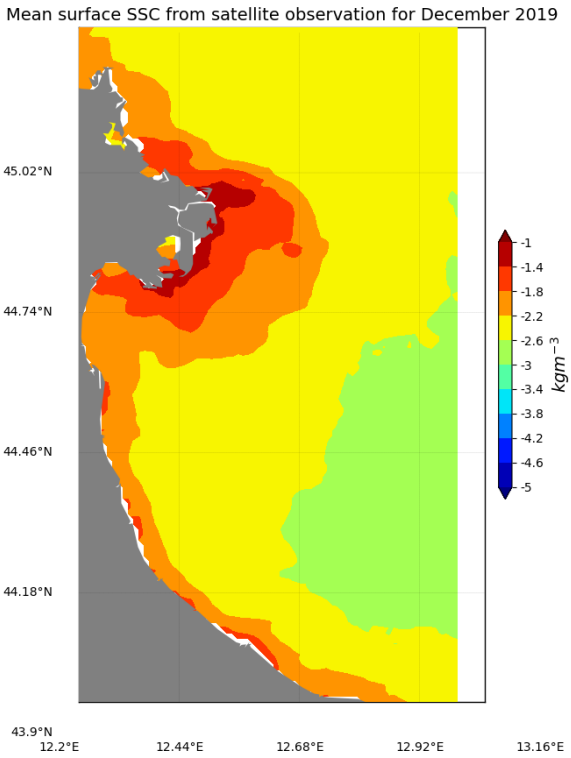

(b) Mean SSC in December 2019 calculated from satellite data

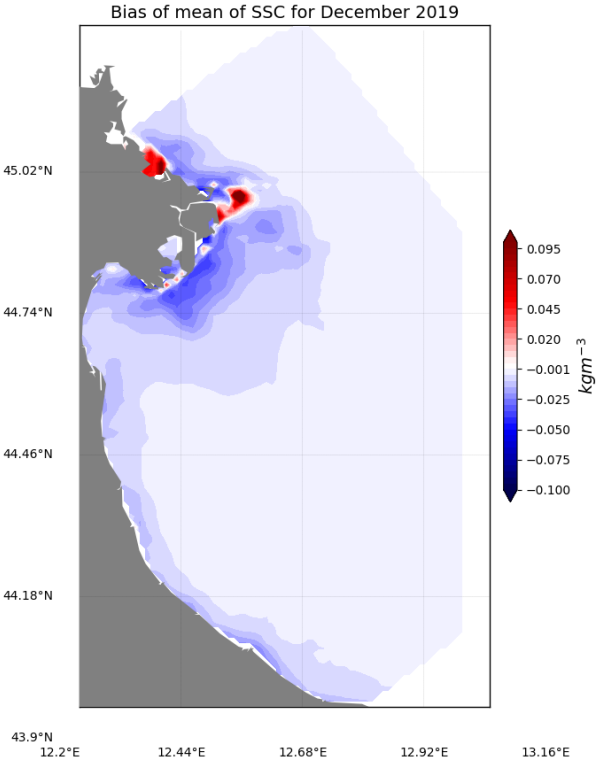

(c) Bias between the findings of the model and observation

Figure 4.10: Mean surface SSC for December 2019, along with its associated bias. For plot (a) and (b), a logarithmic colormap has been employed.

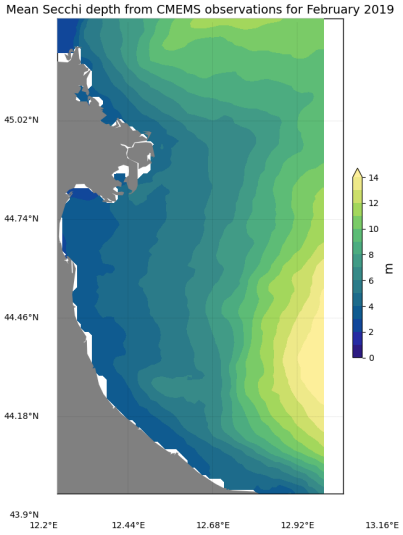

(a) February 2019

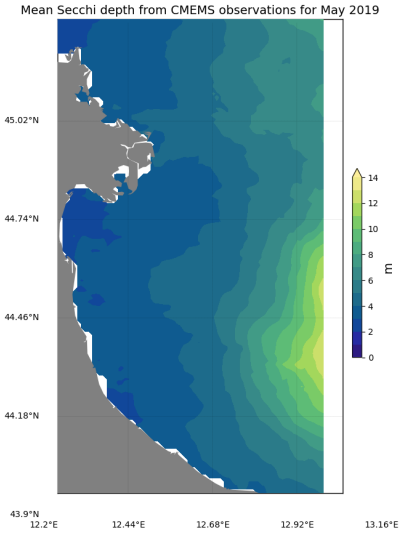

(b) May 2019

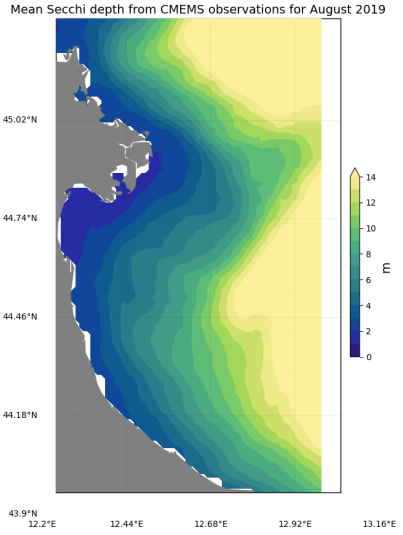

(c) August 2019

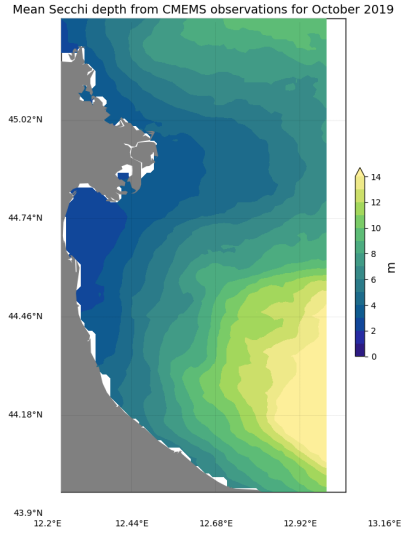

(d) October 2019

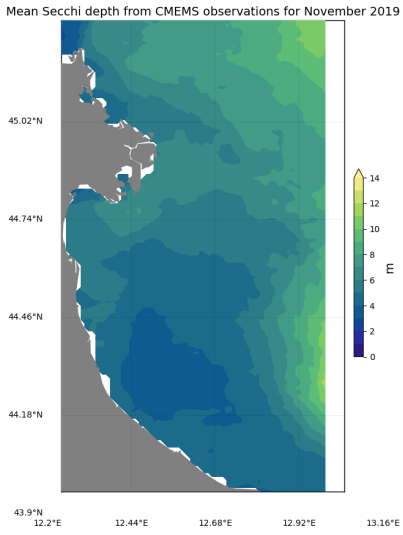

(e) November 2019

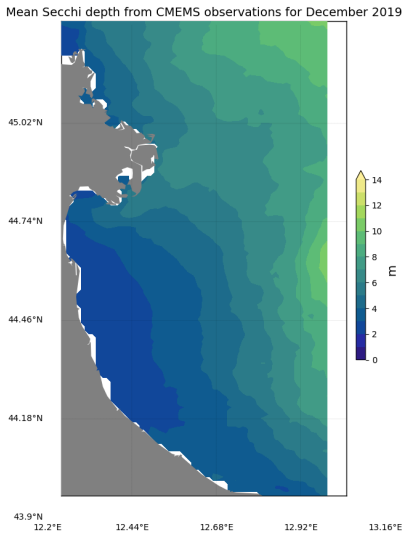

(f) December 2019

Figure 4.11: Maps illustrating the monthly mean Secchi depths utilised in the calculations of the SSC model maps. The Secchi depth is utilised to ascertain the number of vertical levels for the calculation of the SSC of the model.

adhered to during the flood event. Specifically, during the flood months, the Secchi depth increases in the Po Delta region, particularly in front of the Busa di Dritta mouth, extending towards the open ocean and the south along the coastline, as illustrated in the November map (e). A second noteworthy observation is evident in the summer Secchi depth map, which displays the lowest depths around the Po Delta, yet the highest at the ocean open boundary. This signifies a pronounced gradient in visibility, transitioning from onshore to offshore areas. This phenomenon can be attributed to the increased prevalence of algal blooms during summer months in proximity to coastal regions, particularly at river mouths (Alessandri, 2022; Simoncelli, 2010).

4.3 Grain size pattern

The second model result presented in this research is the grainsize pattern following a 12-month simulation period. This output is utilised for the purpose of studying the depositional pattern of the various sediment classes and is furthermore subjected to comparison with the measured seabed composition. The ultimate objective is to ascertain whether the model begins to mirror the mud wedge that extends from the Po Delta in a coast parallel belt and the coarsen of

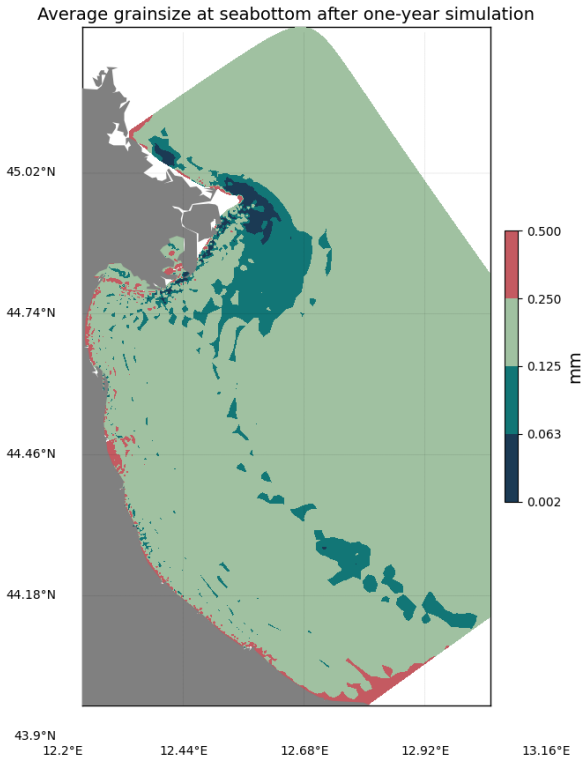

Figure 4.12: Final condition of the numerical model for the average grain size at the seabed.

sediments on both sides of the belt (Fain et al., 2007; Frignani et al., 2005).

For the representation of the grainsize maps, it is decided to use a stepped colormap with four colours. Each colour is assigned to one of the four sediment classes identified in the study area: sand, muddy sand, sandy mud, and mud (from coarser to finer). It is noteworthy that these are congruent with the colours employed in figure 1.5.

The final grainsize pattern at the sea bottom of the model is presented in figure 4.12 for the entire study area and in figure 4.13 for a zoomed-in view of the Po Delta region. The result is then compared to the EMODnet data, which represents the seabed substrate present in the study area and the sedimentation pattern that the model should aim to.

Following a 12-month period of simulation, the model has demonstrated an inability to accurately replicate the substantial band of small-grained sediments indicated by EMODnet data. However, the model's outcome for fine-grained sediments aligns with the configuration depicted in figure 1.5, which illustrates the mud wedge delineated by EMODnet. Specifically, a continuous fine-grained belt commences formation from the Po River, accompanied by coarser sediments on either side of this mud belt. Sandy materials are present in inshore areas, as illustrated in figure 4.13. This sedimentation pattern has been described by Spagnoli et al.

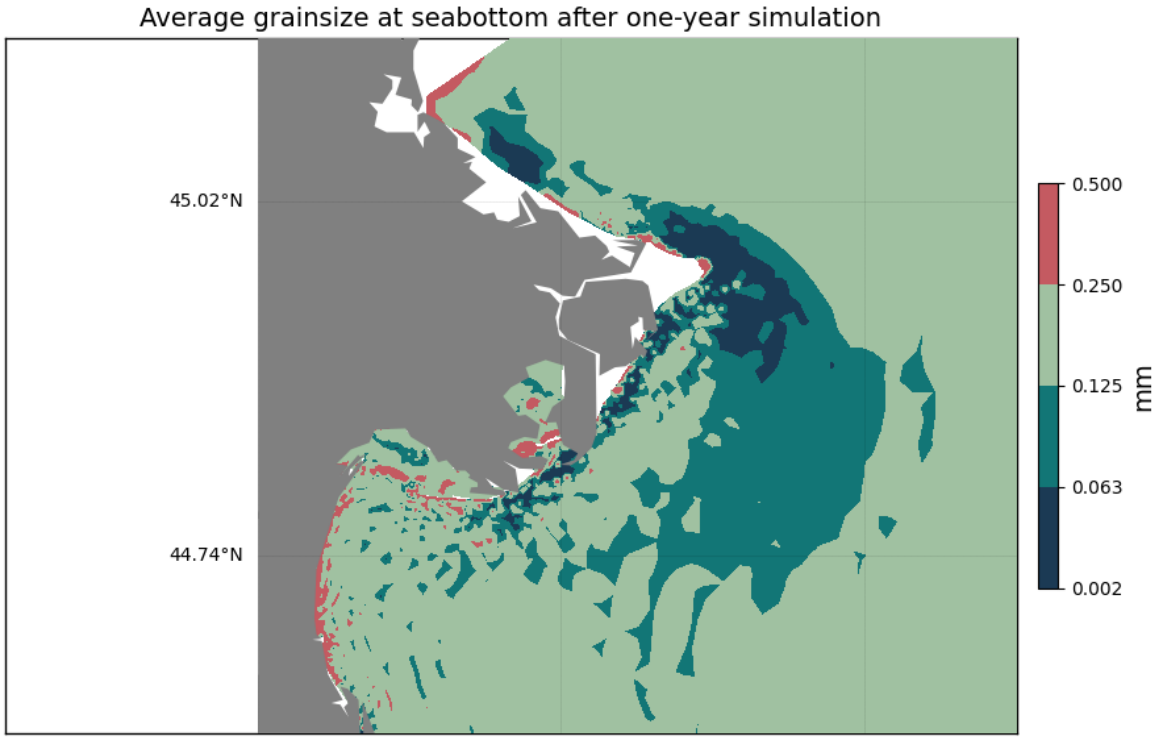

Figure 4.13: Concluding condition of the numerical model with regard to the mean grain size at the seabed in the delta region.

(2014) in their study of the Northern Adriatic sedimentological facies. It is important to note that the maps in figures 4.12 and 4.13 illustrate the average grainsize present within the study area, not the most prevalent of the grainsize classes. A further noteworthy observation is that the model shows sandy areas close to the lateral boundaries of the domain; however, this outcome is attributable to the influence of lateral boundaries, and thus, it should not be taken as definitive.

4.4 Erosion and deposition pattern

The result presented for the one-year simulation is the erosion and deposition patterns. As previously stated, one of the objectives of this research is to depict the recorded erosion and deposition patterns along the Emilia-Romagna coastline. Specifically, the objectives include the depiction of erosion in the vicinity of the Po di Goro mouth and in front of Ravenna, as well as the accretion in front of the Goro lagoon. These three areas of interest are also shown by the dataset of Luijendijk et al. (2018), previously presented in figure 1.6, chapter 1.4.
Furthermore, given the occurrence of a flood event in late 2019, two maps are presented: one prior to and one following the flood. The latter decision is taken because floods are recognised as periods of rapid accumulation near the sources, and these deposits are then reworked (Sherwood et al., 2015; Palinkas et al., 2005).
The two maps are displayed in figure 4.14, in which (a) illustrates the erosion and deposition pattern prior to the flood, and (b) demonstrates the model's result following the event. The latter map demonstrates the significance of floods in terms of sedimentation, particularly when considering the temporal distance between the two maps, which are separated by two months. Specifically, map (a) illustrates the erosion and deposition pattern of the 18^{th} October, while map (b) depicts the pattern of 31^{st} December, which are congruent with the dates utilised in chapter 3.3.2 for the sensitivity analysis of the flood event. A preliminary analysis of the first map reveals that the model's primary depocenters are in the vicinity of the Po River mouths, with notable intensity observed at the Pila, Goro, and Maistra mouths. In the aftermath of the flood, these depocenters are accentuated, and areas where erosion was previously visible are now less eroded, particularly in the southern portion of the Delta. The model can identify the two depocenters of the Pila and Goro distributaries, which are characterised by the highest ac-

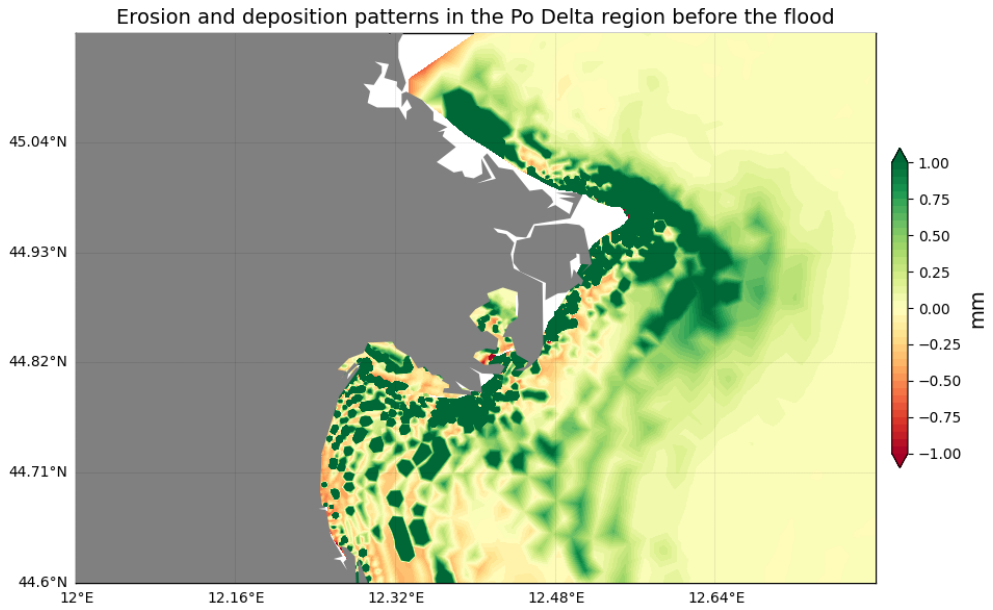

(a) Prior to the 2019 flood

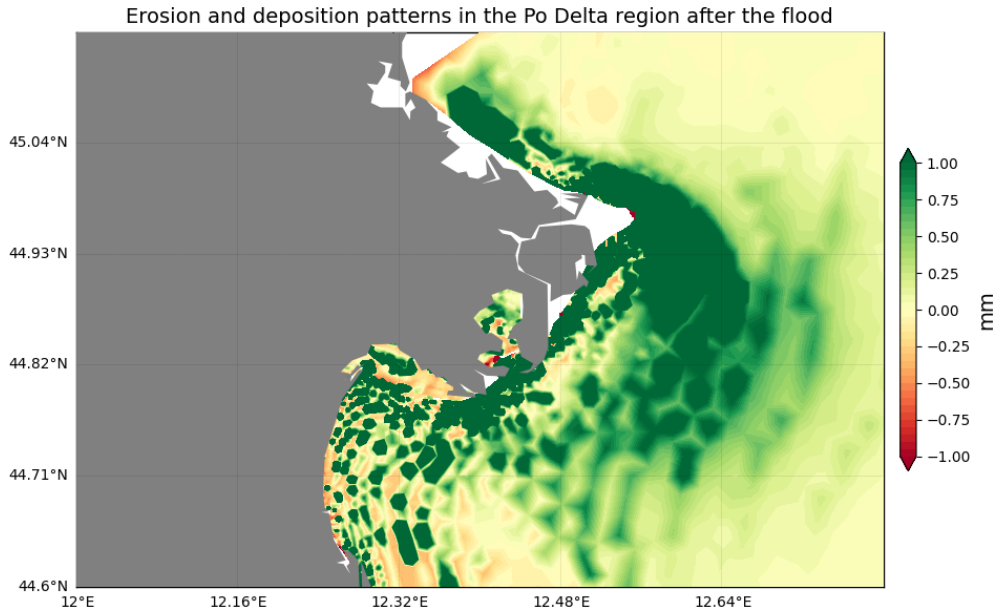

(b) After the 2019 flood

Figure 4.14: Erosion and deposition patterns offered by the model. The colour green is used to denote deposition, whereas red is used to indicate erosion.

cumulation rates (Palinkas and Nittrouer, 2007). This outcome is obtained despite the presence of spurious oscillations in the erosion/deposition pattern exhibited by the model. These oscillations are attributable to numerical challenges in solving the bed continuity equation (Exner equation of the seabed). Two potential causes for this phenomenon are identified: firstly, the grid used in the model, which is corroborated by the pattern geometry given by the model that highly resembles the grid used; and secondly, the consideration of exceptionally sediments (14 μm) as non-cohesive. The latter cause must be considered, given that non-cohesive sediments

exhibit bedload transport, which is not possible for cohesive sediments. Additionally, cohesive sediments flocculate, thereby increasing their resistance to resuspension.

It is acknowledged that flood events have a significant impact on the depositional pattern of the area; therefore, the pre-flood condition is utilised to describe the standard erosion and deposition pattern along the Emilia-Romagna coastline. Specifically, this result is compared with the erosion and deposition trend calculated by Deltares for the shoreline retreat and accretion, and it is also used to check if the three areas of interest are respected. The comparison is illustrated in figure 4.15. The circles are used to show areas where marked erosion (red) or deposition (green) is measured by the Deltares dataset. It is noteworthy that the model successfully captures all four areas identified in the Deltares dataset, albeit with a northward shift and a reduction in erosion intensity. It is important to acknowledge that the two measurements considered here, the model result and satellite observation, are not equivalent. The Deltares dataset represents a rate calculated over a thirty-year period and describes changes to the shoreline; the model result shows changes in the height of the bed from the initial condition. However, after only one year, the model begins to exhibit the observed trend of

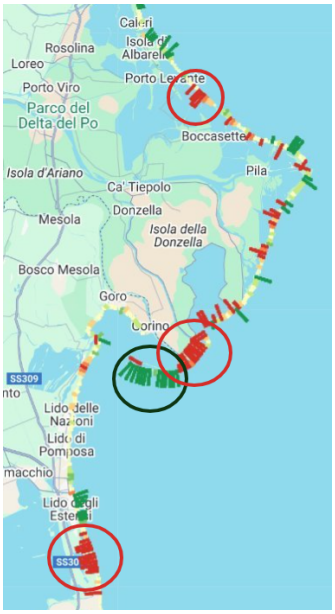

(a) Deltares calculated shoreline accretion and erosion rates for the period 1984-2016

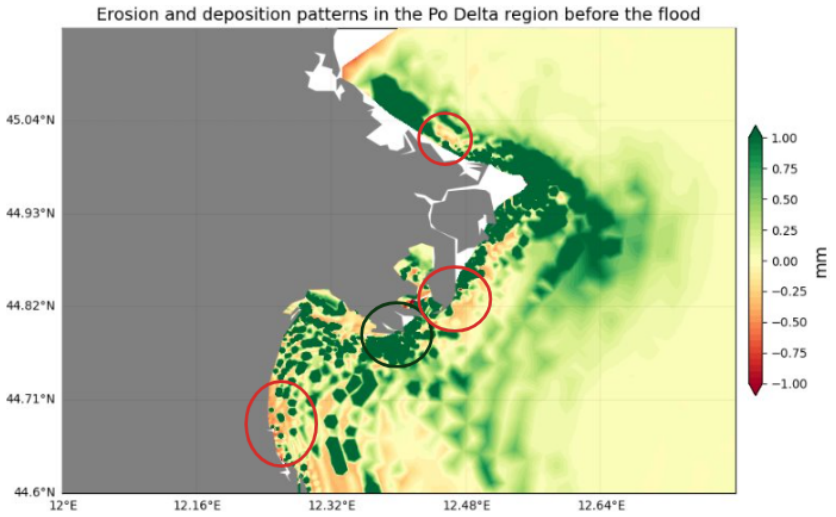

(b) Pattern of erosion and deposition as modelled prior to the occurrence of the flooding event

Figure 4.15: Comparison made between the Deltares dataset of shoreline accretion and erosion rates over multiple years and the model erosion and deposition patterns after one year of simulation. The utilisation of circles is employed to illustrate the areas of accretion (green) and erosion (red) observed in both maps.

erosion and deposition. It is also important to note that the model rates are only given by the sediment transport processes and do not consider any other processes that are present in the area, namely the known subsidence. This discrepancy is the primary factor contributing to the observed divergence in erosion rates between the model and the Deltares dataset, with the model estimating rates of approximately 1 $mmyr^{-1}$, whereas the Deltares data indicates higher values. A more thorough discussion of this discrepancy is provided in the subsequent chapter.

The ensuing discussion will address the findings presented here. This discussion will focus on the suspended sediment transport results and the erosion and deposition patterns.

Chapter 5

Discussion

5.1 Remarks

In the ensuing sections, a more thorough examination of the results presented in chapter 4 is conducted, with a particular focus on suspended sediment concentrations and erosion/deposition patterns.

However, it is imperative to acknowledge the limitations of the model prior to proceeding further. The following list specifies the limitations of the model:

- The entire domain is initialised with four sediment grain sizes (32.5, 94, 187, 375μm) with a 25% proportion of each. In the numerical model, it is not possible to consider the natural layering of the different substrates, but they are all mixed in one layer;
- The linear wave theory present in the SHYFEM-MPI version used for this thesis is remarkably simple and does not consider wave refraction, dispersion and breaking (Umgiesser et al., 2006). Additionally, swell is not considered, as waves are calculated based on the wind field forced over the study area;
- Sediment boundary conditions are only given at the Po River (excluding the Po Levante and Po di Volano, which are not considered in the repartition campaign reported in Zasso and Settin (2012)), Savio and Reno. No boundary condition of sediment is given at the open boundary and at other river mouths, because there is no data;
- The discharges used for all rivers, besides the Po, are monthly climatology taken by Raicich (1994);

- The Po discharges and sediment loadings used as lateral boundary conditions at each mouth are based on the measurements taken at Pontelagoscuro station, assuming no delays or changes.

Awareness of these limitations will facilitate subsequent discussion.

5.2 Suspended sediment transport

The sole available measurements of suspended sediment in the study area and period are satellite observations. The validation of these measurements is carried out by ACRI-ST, who utilise the Copernicus-GlobColour, derived from satellite data, in conjunction with in situ data. Further information regarding the quality of the data provided by CMEMS' OCEANCOLOUR observations can be found in Garnesson et al. (2024). It is important to note that these measurements are only on the near-surface and can only be recorded in cloud-free conditions. However, they offer a robust monitoring system and can be used to observe temporal variability (Villar et al., 2013). Notwithstanding their limitations, these measurements have been utilised to calibrate and validate sediment transport numerical models (e.g. Sadeghian et al. (2017)), as is demonstrated in this research.

The results of the one-year simulation demonstrate the model's capacity to reproduce the alongshore transport of suspended sediment along the coastline, albeit with an underestimation of the concentrations, which increases in proximity to the coast. The underestimation of the model can be attributed to a multitude of factors, but the primary ones can be identified as follows:

- not employing a coupled model with a third-generation wave model;
- erroneous boundary conditions were assigned to sediments at the open and lateral boundaries;
- inaccurate estimation of the critical threshold for motion initiation;
- erroneous particle size classes

The initial aspect, utilising a coupled model with waves, is of particular significance for the resuspension of sediments (Wang et al., 2007). The bottom orbital velocity of waves is found to be a critical parameter for wave-induced bed shear stress, which in turn is a pivotal factor in the

processes of sedimentation, erosion, and resuspension of seabed sediments(Li et al., 2022). Furthermore, wave breaking has been shown to have a significant impact on wind-driven currents, with the Stokes drift being a primary source of these currents (Cavaleri et al., 2012). Lastly, radiation stresses are particularly important in shallow water regions and highly affect wave-driven currents, especially in the alongshore direction (Ji et al., 2024). Additionally, as found by King et al. (2021), micro-tidal regions with fine-grained sediments are wave-dominated, reinforcing the need for a coupled model that incorporates hydrodynamics and waves.

The second feature, incorrect boundary conditions, is evident in the model results. A correct estimation of the sediment boundary condition is an important aspect for modelling sediment transport (Sadeghian et al., 2017). This estimation could be achieved by utilising satellite data; however, it would exclusively consider the suspended sediment concentration, neglecting the size distribution of grains, which is a crucial attribute to ascertain (Ouillon et al., 2004), especially at the boundaries (Lee et al., 2007). Additionally, the data set used for generating the boundary condition would be the same as that used for validating the model result. The simulation does not utilise boundary conditions at the open boundary, owing to the unavailability of data, and the model has not been nested within a larger model. However, it is anticipated that significant contributions from the Alpine rivers and the Venice lagoon will enter the study area from the north and north-eastern open boundaries (Milligan and Cattaneo, 2007), resulting in an overall increase of SSCs.

The third aspect, incorrect critical shear stress estimation, has been identified by previous authors as a primary cause of erroneous sediment transport representation (e.g. Cilli et al. (2018)). Indeed, critical shear stress is utilised as the threshold for the initiation of motion of seabed sediments, both for bed and suspended load transport, and it is calculated using empirical formulas. These formulas are based on one index, grain size, and the Shields criterion, but this solution does not always work for natural sediments, where mixtures are present (Wilcock, 1993). One way of improving this feature is to have direct measurements of the critical stresses for sediment transport initiation or conduct laboratory experiments with a realistic mixture of sediments. Another option would be to update the method used by SHYFEM-MPI to calculate the critical threshold stress during the simulation. Indeed, SHYFEM-MPI calculates the critical motion threshold for all time steps, besides the initial one, that can be specified. For

this thesis, it was not possible to apply any of these approaches, so no improvement was given for the calculation or estimation of the critical shear stresses.

A further potential explanation for the underestimation of SSC by the model is the utilisation of erroneous grain sizes. Specifically, the four sediment classes present in the study area range from grains of 2 μm to 500 μm, yet the model employs only five grain sizes. The five grainsizes selected correspond to the mean value of each class (32.5, 94, 187 and 375 μm) and an additional finer grainsize (14 μm), based on field data. A more accurate representation could be achieved by utilising a greater number of grainsizes, particularly those that are more prevalent. The grain size distribution is a significant aspect to consider when constructing a robust and reliable model for sediment transport (Sadeghian et al., 2017).

Grain size distribution is also a particularly important aspect for satellite data collection. Indeed, granulometric distribution has been demonstrated to affect the optical characteristics of the Total Suspended Matter (TSM) in the water column, thereby alterating the relationship between reflectance and TSM concentrations recorded by the satellite (Miller and McKee, 2004). It is acknowledged that granulometric distribution can vary throughout the year (Villar et al., 2013), yet maintaining a sampling programme that adequately describes these variations is a fundamental limiting factor (Stroud et al., 2009). While classical monitoring for suspended sediment concentrations is highly valuable and necessary, it is costly, time-consuming, and limited in its spatiotemporal representation (Pandey et al., 2016). Consequently, the in situ data can be utilised to validate the SPM's satellite measurements, which in turn, can be employed to calibrate and validate transport models (de Oliveira Fagundes et al., 2020). In the context of this research, this knowledge could confirm the presence of permanently suspended particles in the considered domain, as appears to be recorded by satellites.

The model displays lower concentrations overall, yet at certain river mouths, an inverse phenomenon is observed. This phenomenon is particularly evident in the vicinity of Busa di Dritta and Po di Maistra. This discrepancy can be attributed to an inaccurate allocation of sediment load among the various mouths and the utilisation of erroneous sediment forcing. Specifically, the sediment forcing applied at the mouths is derived from the sediment load measurement conducted at Pontelagoscuro, under the assumption of no deposition or resuspension downstream. Furthermore, the elevated model concentrations are characterised by minimal spatial

extension, suggesting a substantial accumulation of suspended sediments in the vicinity of the river mouths. The settling velocity is calculated using the Soulsby and Whitehouse (1997) method for each grain size, which can result in some uncertainties (Schippa et al., 2019). It has been acknowledged that settling velocity is a pivotal parameter for evaluating the efficacy of the model (Allen et al., 2021). Two proposed solutions for this issue are: to specify measured settling velocities for each grainsize or to use another method to calculate settling velocities.
During summer, the model is not able to represent the along-shore pattern of sediment concentrations. Suspended sediments have been observed to decrease in measurements, yet the model results have sediments only close to the river mouths. The lower concentrations observed during the summer months can be attributed to the reduced river discharges, which are utilised for agricultural purposes, and the decreased precipitation levels. Concerning the model's failure to replicate the along-shore pattern, two factors have been identified as contributing factors. Firstly, an increase in benthic organisms residing on the seabed has been observed, leading to enhanced sediment erodibility and, consequently, facilitated resuspension (Stevens et al., 2007). The second is the settling velocities employed, as discussed in the preceding paragraph. A potentially beneficial approach would be to implement a more flexible settling coefficient for sediments, as suggested by Sadeghian et al. (2017).
During the flood event, the model displays an elevated level of representation of the pattern along the coast and is also capable of correctly representing the plume evolution. This is particularly evident when considering the plume's initiation at Busa di Dritta, its subsequent trajectory towards the open ocean, and its subsequent deviation towards the south. It is notable that the concentrations in the Po Delta region are consistently lower compared to other periods. During flood events, elevated levels sediment are anticipated to be transported to the coastal waters, attributable to increased river discharges, leading to heightened sediment resuspension along riverbeds, particularly in the vicinity of the Delta area, and to the opening of sluice gates in minor rivers. This phenomenon is particularly pronounced in the case of minor rivers, such as the Apennine rivers, which are characterised by sluice gates that are utilised for the regulation of their discharge. These gates exert a major influence on the transport and accumulation of sediments (Cilli et al., 2021). During periods of flooding, the sluice gates are opened, resulting in the resuspension of sediments upstream of the gate and subsequent

discharge into the sea. However, the dynamics of sluice gate operation remains a critical yet unaccounted parameter in existing simulations, due to the paucity of data available on this subject. In addition to the increased sediment load in coastal waters, flood events are commonly associated with heightened stratification, attributable to salinity and temperature variations. As Verri et al. (2023) have demonstrated, during flood periods, the freshwater is confined to a thin surface layer, which subsequently spreads further away from the Delta. Consequently, it is anticipated that sediments will be transported further offshore. This representation of the river plume is optimised through the utilisation of a z* vertical discretisation, as opposed to the z discretisation employed in this study. The z* vertical discretisation ensures an even distribution of oscillation of the free surface between the vertical levels, independent of the characteristics of the bottom topography.

The model demonstrates an ability to replicate the primary along-shore sediment pattern; however, its efficacy is diminished in more offshore locations. This outcome is encouraging for prospective applications; however, to develop a viable model for studying sediment transport with precise volume estimations, additional data is required. The following datasets have the potential to enhance the model's performance for SSC:

- The solid discharge of all the rivers
- The grain size information of the solid load of the different rivers
- Direct measurements of critical shear stresses for the initiation of motion
- The suspended sediment concentrations at the open boundary of the model, with particular attention to the northern boundary

5.3 Sediment accumulation and erosion areas

During the study period, no measurement campaign of coastal transects or bathymetric surveys were conducted. The only available dataset that can be used as a guide of the erosion and deposition patterns present along the Emilia-Romagna coastline is the shoreline accretion and erosion rate offered by Luijendijk et al. (2018). As previously mentioned, this dataset measures the changing rate of shoreline transects over a thirty-year period. This rate is calculated using

satellite images and indicates whether the transect has evolved inshore (erosion, red) or offshore (accretion, green). Conversely, the model delineates the vertical bed alteration in relation to the initial bathymetry, and it should be noted that this research employs a one-year simulation exclusively. Despite the disparity in the temporal extents and the distinct nature of these processes, a comparative analysis is undertaken between the two measurements.

The results presented in figure 4.15 demonstrate that, despite the model exhibiting spurious oscillations in the solution of the bed continuity equation and a dependence on the grid used, it can represent the pattern of erosion and deposition. This observation can be made only in the vicinity of the Po Delta. However, the erosion rates calculated by the model are underestimated and the model pattern is skewed toward the North.

The underestimation of the erosion rates can be attributed to the observation that the dataset of Luijendijk et al. (2018) exhibits comparable levels of erosion and accretion in areas subject to these processes. In contrast, the model demonstrates significantly less intense erosion rates in comparison to deposition rates. Another justification for the underestimation of the model is that calculated annual erosion rates are of the order of $mmyr^{-1}$, which are in line with the SLR recorded for the northern Adriatic Sea (1.3 $mmyr^{-1}$ in Trieste (Douglas, 1997)), which should result in a relatively stable coast. However, this is not the case for the study area. Consequently, there must be some additional processes that are not considered by the model, but which affect the erosion rate calculated by the model. The primary cause of the erosion underestimation by the model could be the subsidence of the area, due to secondary sediment consolidation and sediment loading (Bezzi et al., 2021). The Delta region subsidence rate has been measured to be between 2.5 and 7.5 $mmyr^{-1}$ (Bitelli et al., 2020), resulting in a decrease in terrain elevation. It is acknowledged that the subsidence rate cannot be incorporated into the model results. However, the anticipated response to the erosion and deposition pattern is a decline in deposition rates and an increase in erosion rates, given the decreasing terrain level over time. This increase in erosion and decrease in accretion results in two rates closer in intensity. For the dataset presented in Luijendijk et al. (2018), the subsidence of the Delta region has already been applied, since the measurement is calculated on the shoreline given by satellite images.

Conversely, the skewness towards the North remains unproven, although several hypothe-

ses have been postulated to explain it. The primary reason pertains to the utilisation of a parametrization technique, a method that invariably gives rise to a certain degree of uncertainty. A notable element that has been identified as a crucial factor in critical shear stress is the porosity of the seabed sediment, as highlighted by Stevens et al. (2007). Secondly, the transport of sediment is a complex system, and the processes involved are not yet fully understood, which hinders the accuracy of the model (Margvelashvili et al., 2013). Thirdly, there is an inaccurate depiction of current intensities and directions in proximity to the shoreline, owing to the inaccuracy in the representation of wave-current interaction and the inappropriate forcing employed for rivers. The fourth and final reason is based on the grid used for the research, which forces rivers directly at the coastline. A more accurate representation would be achieved by incorporating additional elements within the rivers' inlets, thereby enhancing the outflow representation of the rivers, particularly with regard to direction. Additionally, the resolution of the grid along the coastline could be enhanced to ensure more precise representation of the river estuaries present in the study area, as a resolution of 330 m is inadequate for accurate depiction. It is noteworthy that the mouths of all rivers in the study area are narrower than 330 m, apart from Busa di Dritta. It is further posited that modifications to the grid resolution may yield enhancements in the spurious oscillations that have been identified, as well as the erosion/deposition pattern that exhibits a discernible correlation with the grid.

In conclusion, the model exhibits a congruent erosion and deposition pattern with the measured Po Delta area, although it should be noted that the model is constrained to a one-year period, whereas the measurement is derived from three decades of data. Consequently, the observations can be regarded as a climatology of this process.

However, the observed pattern does not align with the expected behaviour for the entire study area, as it exhibits a greater degree of accretion than what is measured. The maps depicting the measurement and the model result before and after the flooding of the entire Emilia-Romagna coastline are presented in figure 5.1. In manner consistent with the Po Delta area, the erosion pattern documented by Luijendijk et al. (2018) exhibits a skewing towards the north. However, for the remainder of the coastline, the model displays marked accretion, both prior to and following the flood, thus failing to align with observations that indicate a state of equilibrium (yellow bars). As previously mentioned, the only rivers that are forced by sediments are the Po

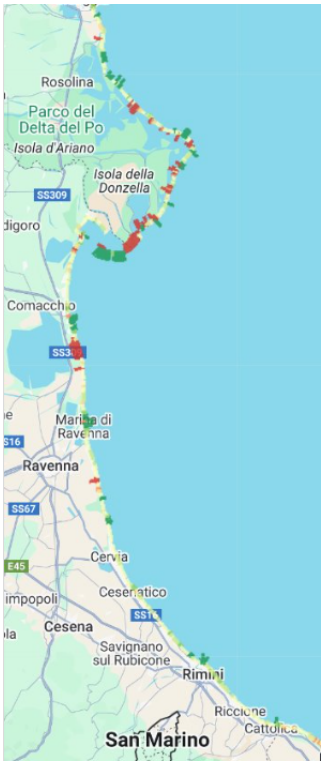

(a) Deltares shoreline accretion and erosion rates for the period 1984-2016

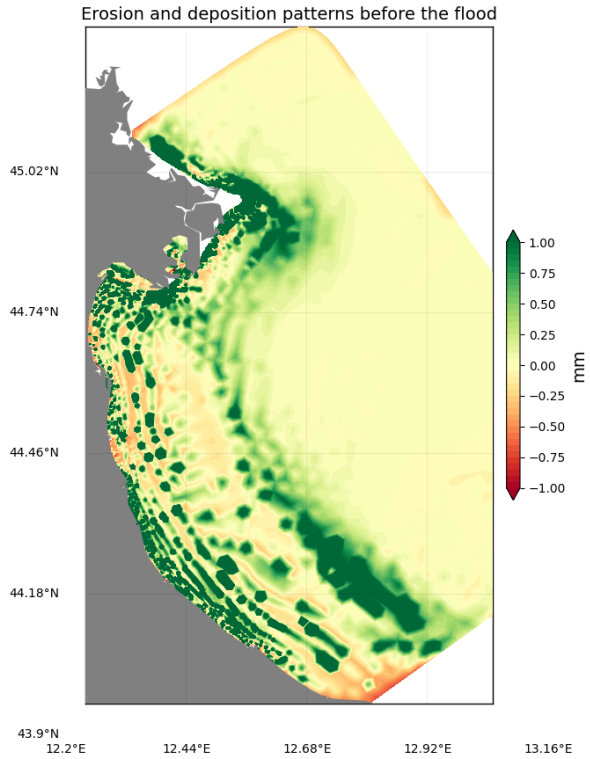

(b) Erosion and deposition rates along the Emilia-Romagna coastline prior the occurrence of the flood

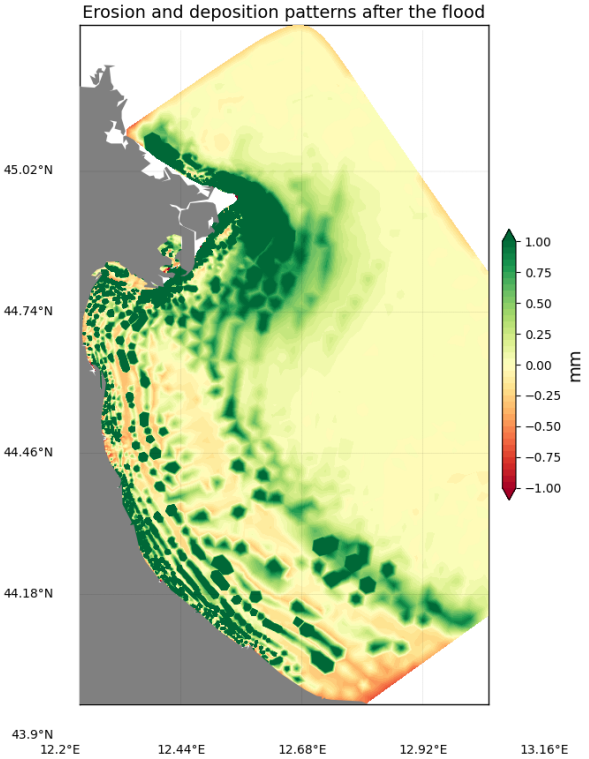

(c) Erosion and deposition rates along the Emilia-Romagna coastline in the aftermath of the flood

Figure 5.1: Comparison made between the Deltares dataset of shoreline accretion and erosion rates over multiple years (a) and the model erosion and deposition patterns before (b) and after (c) the flood event of 2019.

River, the Savio and the Reno. The Po River is distinguished by direct measurements of both discharges and turbidity, while the Savio and Reno rivers are characterised using climatological data. For all other rivers, the only available data are those relating to discharge, due to a paucity of data on suspended sediment load for Italian rivers (Frignani et al., 2005). However, Apennine rivers have been identified as significant contributors to the sediment load of the Emilia-Romagna coastline (Harris et al., 2008). Consequently, a precise representation of river contribution, both in terms of discharge and sediment load, has been identified as a crucial aspect for modelling (Sherwood et al., 2015). Consequently, to ensure an accurate depiction of sediment transport processes along the entire Emilia-Romagna coastline, it is imperative that rivers are modelled using actual discharge and sediment loading measurements rather than climatological data. The implementation of enhanced lateral boundaries for rivers is anticipated to enhance both hydrodynamics and sediment transport processes. This assertion is substantiated by empirical evidence from the Po Delta region, where the utilisation of actual discharge and sediment load measurements has been demonstrated to yield more accurate depictions of erosion and deposition patterns. Furthermore, it is anticipated that Po River flood events will result in elevated accretion rates across the entire study area. However, the methodology employed in this study identifies higher accretion exclusively within in the Po Delta region. The remaining coastal areas exhibit no alteration in accretion rates, both prior to and following the flood event.

In Conclusion, to achieve a more accurate depiction of the erosion and accretion patterns along the Emilia-Romagna coastline, it is imperative to enhance river forcing through the utilisation of empirical measurements of discharge and turbidity. Indeed, the erosion and depositions demonstrate a high degree of agreement for areas where fluvial forcing is taken from measurements. Furthermore, the measurement of turbidity data is imperative, as it is not feasible to utilise or delineate a relationship between liquid and solid discharge, as highlighted by Cilli et al. (2021).

5.4 Sediment transport dynamics in the study area

The primary dispersal trajectory of sediments within the study area is along the shoreline. Specifically, suspended sediments are ensnared within the WACC current that is present along the Western border of the Adriatic Sea, and are subsequently advected, predominantly in a southerly direction. This dispersion pattern is more visible during Po River floods, where the plume extends further offshore than in normal conditions and then deviates towards the south. An interesting pattern that is more visible when considering the model results is the lower SSC in the bay in front of the Sacca di Goro, extending from Lido di Volano and Bellocchio. This area exhibits reduced concentrations of suspended sediments, as highlighted by satellite data, though these concentration gradients are less perceptible.

The model distinctly demonstrates that during the summer months, the sediment concentration within the domain undergoes a substantial decline, exhibiting no discernible along-shore pattern. This outcome can be ascribed to the diminished discharges of the rivers, both in terms of water and sediments, and to the reduced intensity of both waves and currents that are typically present during summer. This is highlighted by the absence of significant wave events during the summer months of 2019.

Wave resuspension is a crucial factor to consider in this study area, and the accurate modelling of wave forcing leads to enhanced sediment transport process modelling. This assertion is substantiated by the observation that when wave forcing is moderately well represented by the rudimentary wave model employed in this research, there is a concomitant alignment between the modelled SSC and the observations. Conversely, when wave forcing is significantly underestimated, the SSC are underestimated relative to the measured values. Beyond the phenomenon of resuspension, it is anticipated that wave breaking will also exert an influence on currents, through an augmentation in their intensity.

The examination of the mean grain size pattern presented in the concluding section of the one-year simulation reveals that the sediments introduced by the Po River, characterised by their fine grain size, are deposited in a belt that extends from the Busa di Dritta mouth, the most efficient of the mouths, in a northerly and southerly direction. This phenomenon is in accordance with the along-shore evolution of the plume, and some sediments even reach the southern boundary of the domain and exit it. A notable phenomenon is the presence of a

sand layer along the coast, which is slightly more pronounced than its real-world counterpart. This sand layer is a consequence of the model's representation of the reworking of the initial sediments forced at the bed. It is notable that no sand is introduced by rivers in the configuration employed; therefore, the sole available source is the seabed. This phenomenon can be interpreted as a result of the energy levels present near the coast being insufficient to remove the sandy part of the seabed, but sufficient to resuspend only the smaller particles.

The deposition recorded by the model resembles the mean grain size pattern, especially when considering the fine-grained sediments. The highest deposition is observed in the vicinity of the Po River mouths and along the plume dispersion pattern. However, the most prominent identifiable deposition centre is in front of Busa di Dritta, exhibiting a slight tilt towards the south. Another area that has a high deposition for the model is the coastline south of Lido Adriano, resulting from the incorrect forcing applied to the Savio river, both for water and sediments.

Areas of erosion are recorded close to the coast and in the southern part of the bays present. Two distinct bay-like areas are evident: the first is situated between Lido di Volano and Bellocchio, and the second is located between Bellocchio and Lido Adriano. The erosion is particularly pronounced in the latter area, extending beyond the breakwaters of Porto Corsini, encompassing the region of Marina di Ravenna. In contrast, the Po Delta region exhibits a less pronounced degree of erosion.

The subsequent chapter will provide a synopsis of the findings of this research, encompassing both the sensitivity analysis and the one-year simulation. It will also offer insights into potential avenues for future research and the enhancement of the sediment transport model presented in this thesis.

Chapter 6

Conclusions

This chapter provides a synopsis of the thesis's primary conclusions, derived from both the sensitivity analysis simulation experiments and the one-year simulation. It further explores avenues for research that could enhance the outcomes achieved to date.

In recent years, there has been a surge of interest in the field of sediment transport and the response of coastlines to erosion and deposition processes, particularly in the context of climate change. Numerical models are recognised as the only available methods to study these processes and define the best management strategy in the changing climate conditions.

Before listing all the results and conclusions, it is important to highlight that this marks the first attempt to represent sediment transport along the Emilia-Romagna coastline using SHYFEM-MPI finite element model, which incorporates varying resolution and multiple sediment classes. The unstructured grid has a resolution of 330 metres at the coast and five different sediment classes, ranging from sand to silt.

In summary, this research successfully achieved its main objective of developing a numerical model capable of describing sediment transport in the Emilia-Romagna coastal zone. Looking at the research questions for this research:

1. Does SHYFEM-MPI have the capacity to adequately represent the observed suspended sediment concentration patterns along the coast? Does the plume geometry and evolution resemble the observed patterns?

   The model displays a high degree of proficiency in reproducing the SSC patterns, particularly in the case of the Po plume. It is particularly adept at replicating the along-shore pattern of SS, which extends from the Po Delta in a northerly and southerly direction.

Moreover, during the flooding period, the plume exhibits patterns analogous to those observed. Additionally, the model reproduces the seasonality of sediment transport in the study area.

2. Can the model reproduce the depositional pattern of the study area? Is the mud belt surrounded by coarser sediments?

   Following a period of one year's worth of modelling, the model exhibits characteristics of the depositional pattern that are distinctive of the study area. In particular, the mud belt, which is situated around the 20-metre isobath, commences formation, and the presence of coarser grain size is observed, particularly in the vicinity of the coast. Furthermore, the model can represent the sandy layer that is present at the shoreline, albeit in a more extensive area that which was observed.

3. Can the model reproduce the recorded erosion deposition patterns? Can the model represent the erosion in the Po di Goro area and in front of Ravenna? Can the model represent the deposition present at the Goro lagoon?

   Despite the model's apparent dependency on the grid configuration and the presence of oscillations in the bed continuity equation's outcomes, the results exhibit comparable patterns to the observed ones. The model yields results that are skewed towards the north and exhibit lower erosion rates than those observed. These observations have been previously explained and discussed in the preceding chapter. With regard to the requested erosion area, the model displays reasonable agreement with the observed erosion in front of Ravenna, particularly in the southern area from the breakwaters of the Marina. However, the erosion of the Po di Goro is shifted more northward, and the deposition occurring in front of the Goro lagoon is also shifted northward from the observed depositional area.

The following additional findings are listed here:

- The critical erosion stress (a free parameter for the sediment model) does not appear to have an impact on the result, since the calculated area average RMSE is identical for the two values used;

- The settling velocity used for each sediment grain size is an important variable, and further research should be conducted to determine the best parametrization;

- The Van Rijn et al. (1993) method is the most effective in describing the sediment transport processes of the study area;
- The sediment horizontal diffusion coefficient has minimal impact on suspended sediment transport calculations; therefore, it is set to zero, reducing the computational time of the model.
- The model can represent the along-shore suspended sediment concentration pattern, albeit with lower concentrations. However, the model does not reproduce this pattern during the summer months, due to the absence of contribution from the northern rivers and the background suspended sediment concentrations.
- The model is unable to accurately represent the background SSCs offshore due to the absence of sediment forcing at the open boundary;
- During flood events, the model accurately replicates the Po plume shape, despite its spatial confinement;
- The model successfully reproduces the overall erosion and deposition patterns measured along the coasts near the Po River Delta, utilising measured discharge and turbidity data.
- A significant limitation of the research has been the unavailability of sediment data, both as input from the rivers and suspended concentrations in distinct parts of the basin.

The next chapter offers an overview of additional studies or steps to take to improve the modelling of sediment transport in the Emilia-Romagna coastal strip.

6.1 Outlook and future steps

A significant challenge encountered during this research pertains to the paucity of observational data, particularly with regard to river sediment loads. The Po River stands as a notable exception, as it is the sole subject for which empirical measurements of discharge and solid load were available, a feature that was absent in the other cases. The utilisation of climatological data alone does not permit the consideration of the substantial interannual variability associated with sediment inputs from rivers (Milligan and Cattaneo, 2007). The incorporation of

in situ observations at river mouths is therefore essential for enhancing more accurate results. Apart from river forcings, there is an absence of direct measurements of suspended sediments along the coast, with satellite imagery being the sole source of knowledge in this regard. While satellite imagery is undoubtedly a valuable asset for future research, the available products still require refinement to accurately differentiate between the sediment signal and organic material concentrations. However, in this thesis, the available satellite imagery from ocean colour sensors offers an exceptionally suitable alternative to the missing in situ data for suspended sediments. Satellite imagery in the visible range is also limited by cloud cover and only offers an overview for integrated suspended sediment, not giving information on sediment transport close to the seabed. In previous experimental studies, a tripod station was considered for measuring concentration measurements close to the seabed (e.g. Traykovski et al. (2007)). Another interesting observational dataset could be collected by successive bathymetric surveys of the same area with a monthly or bi-monthly periodicity. It is expected that these tripod and successive bathymetric survey observations will improve the calibration and validation of the model setup. A further issue encountered by the subregional model utilised in this thesis pertains to the absence of sediment conditions at the open boundary. This paucity of boundary conditions gives rise to diminished concentrations within the model domain, thereby engendering an erroneous representation of sediments offshore. To address this challenge, a potential approach involves the consideration of a parent model encompassing the entire Adriatic Sea, with the present model being nested within this larger model. Alternatively, augmenting the model domain to encompass the entire North Adriatic Sea could serve as a solution. Alternatively, the derivation of sediment boundary conditions from satellite measurements, incorporating their near-surface values and extrapolating them to deeper levels, could be considered.

The third aspect that should be improved is the wave field used for the calculations, given that waves are recognised as one of the most crucial factors for sediment resuspension, especially under wave-breaking conditions. The configuration utilised in this study simplifies the wave processes to linear wave theory, neglecting breaking waves and non-linear interactions between hydrodynamics and waves. A more accurate representation of the wave field and the resultant stresses could be achieved by employing a third-generation wave model, such as Wave Watch III, in online coupling with the hydrodynamic model. In Pillai et al. (2022), an offline coupling

of SHYFEM-MPI with WWIII was conducted for the same grid utilised in this thesis, demonstrating the feasibility of a coupling between the two models. Improved representation of the waves is anticipated to yield enhanced representation of suspended sediments along the coast and elevate the model concentrations.

The fourth proposed improvement pertains to the grid under consideration. The current grid, it is argued, imposes a direct force of rivers along the coastline; however, a more accurate representation may be achieved by incorporating additional elements within the river inlets. Indeed, imposing such direct force of rivers along the coastline has the potential to introduce errors in the discharge direction. Additionally, incorporating additional elements and enhancing the resolution of the coastline would be advantageous, as the current resolution of 330 meters can be considered coarse when compared to the river estuaries present in the region and the infrastructures present along the coast.

Furthermore, there are other proposed future lines of development related to sediment parameters that have not been considered in this study. The first parameter that requires further research is the porosity, both superficial and not. The second parameter is the sediment density, for which only two values have been considered in this thesis, both of which are based on literature. The third and final parameter is the settling velocity, which should be defined for each sediment class.

As previously mentioned, this research is the first of a series of developments to be carried out in the next few years, describing the sediment transport along the Emilia-Romagna coastline. The ultimate objective is to develop a sediment transport model for the region, with the aim of quantifying and evaluating the future risks of climate change for coastal sea flooding and beach erosion. This model will provide local authorities with the necessary information to inform risk management plans.

Appendix A

Example of .str file

$title

er

er_sed

ER_newbathy_luis_new.bas

$end

$para

date = 20190320

time = 000000

coumax = 0.9

itsplt = 0

idtsyn = 3600

idtmin = 0.5

itanf = 0 itend = 1468800 idt = 80

idtout = 3600 itmout = 3600

idtcon = 3600 itmcon = 3600

idtrst = 864000

itmrst = 864000

ilin = 0

itlin = 0

iclin = 0

rlin = 1

ampar = 0.6

azpar = 0.6

avpar = 0

aapar = 0

ievap = 1

isolp = 1

botabs = 1

ihtype = 3

iheat = 8

iwtype = 1

itdrag = 4

dragco = 0.0025

isphe = 1

noslip = 1

iturb = 1

ireib = 6

czdef = 0.01

ibarcl = 1

itemp = 1

isalt = 1

idhtyp = 2

vismol = 1.e-6

difmol = 1.e-7

vreps = 1.e-3

ilytyp = 2

ihwadv = 2

itvdv = 0

ahpar = 0.2

shpar = 0.2

thpar = 0.2

chpar = 0.2

dhpar = 0.2

$end

$waves

iwave = 1

idtwav = 3600

itmwav = 3600

$end

$sedtr

isedi = 1

itmsed = 3600

idtsed = 3600

adjtime = 3600

sedgrs = 0.0325 0.094 0.187 0.375

tauin = 0.04 0.06 0.08 0.1

percin = 0.25 0.25 0.25 0.25

sedhpar = 0

$end

$levels

1.5 2.0 3.0 4.0 5.0 6.0 7.0 8.0 9.0 10.0 12.0 14.0 16.0 18.0 20.0 22.0 24.0 26.0 28.0 30.0 32.0 34.0 36.0 38.0 40.0 42.0 44.0 46.0 48.0 50.0 52.0 54.0 56.0

$end

$bound1

kbound =

37 38 39 40 41 42 43 44 45 46 47 48 49 50 51 52 53 54 55 56 57 58 59 60 61 62 63 64 65 66 67 68 69 70 71 72 73 74 75 76 77 78 79 80 81 82 83 84 85 86 87 88 89 90 91 92 93 94 95 96 97 98 99 100 101 102 103 104 105 106 107 108 109 110 111 112 113 114 115 116 117 118 119 120 121 122 123 124 125 126 127 128 129 130 131 132 133 134 135 136 137 138 139 140 141 142 143 144 145 146 147 148

ibtyp = 1

intpol = 2

tnudge = 3600

boundn = 'Input/boundn_1_Juno.dat'

saltn = 'Input/saltn_1.dat'

tempn = 'Input/tempn_1.dat'

vel3dn = 'Input/uv3d_1.dat'

$end

Po Levante

$bound2

kbound =

150 151

ibtyp = 2

salt = 15.000000

tempn = 'Input/rivers/temp/Po_levante_temp_new.txt'

boundn = 'Input/rivers/Po_levante_2018_2019.txt'

$end

Po Maistra

$bound3

kbound =

154 155

ibtyp = 2

salt = 17.000000

tempn = 'Input/rivers/temp/Po_maistra_temp_new.txt'

boundn = 'Input/rivers/Po_mst.dat'

sed2dn = 'Input/rivers/sed/sed4_new_Po_mst.dat'

$end

Busa di Tramontana

$bound4

kbound =

177 178

ibtyp = 2

salt = 17.000000

tempn = 'Input/rivers/temp/Busa_tram_temp_new.txt'

boundn = 'Input/rivers/Busa_tram.dat'

sed2dn = 'Input/rivers/sed/sed4_new_Busa_tram.dat'

$end

Busa di Dritta

$bound5

kbound =

194 195 196

ibtyp = 2

salt = 17.000000

tempn = 'Input/rivers/temp/Busa_drit_temp_new.txt'

boundn = 'Input/rivers/Busa_dritta.dat'

sed2dn = 'Input/rivers/sed/sed4_new_Busa_dritta.dat'

$end

Busa di Scirocco

$bound6

kbound =

215 216

ibtyp = 2

salt = 17.000000

tempn = 'Input/rivers/temp/Busa_scir_temp_new.txt'

boundn = 'Input/rivers/Busa_scir.dat'

sed2dn = 'Input/rivers/sed/sed4_new_Busa_scir.dat'

$end

Busa Storiana

$bound7

kbound =

238 239

ibtyp = 2

salt = 17.000000

tempn = 'Input/rivers/temp/Busa_stor_temp_new.txt'

boundn = 'Input/rivers/Busa_stor.dat'

sed2dn = 'Input/rivers/sed/sed4_new_Busa_stor.dat'

$end

Bocca Nord - Gnocca

$bound8

kbound =

340 341

ibtyp = 2

salt = 17.000000

tempn = 'Input/rivers/temp/Po_gnocca_N_temp_new.txt'

boundn = 'Input/rivers/Po_gnocca_N.dat'

sed2dn = 'Input/rivers/sed/sed4_new_Po_gnocca_N.dat'

$end

Bocca Sud - Gnocca

$bound9

kbound =

346 347

ibtyp = 2

salt = 17.000000

tempn = 'Input/rivers/temp/Po_gnocca_S_temp_new.txt'

boundn = 'Input/rivers/Po_gnocca_S.dat'

sed2dn = 'Input/rivers/sed/sed4_new_Po_gnocca_S.dat'

$end

Po di Goro

$bound10

kbound =

350 351

ibtyp = 2

salt = 17.000000

tempn = 'Input/rivers/temp/Po_Goro_temp_new.txt'

boundn = 'Input/rivers/Po_goro.dat'

sed2dn = 'Input/rivers/sed/sed4_new_Po_goro.dat'

$end

Volano

$bound11

kbound =

556 557

ibtyp = 2

salt = 15.000000

tempn = 'Input/rivers/temp/Po_Volano_temp_new.txt'

boundn = 'Input/rivers/Po_volano_2018_2019.txt'

$end

Reno

$bound12

kbound =

668 669

ibtyp = 2

salt = 15.000000

tempn = 'Input/rivers/temp/Reno_temp_new.txt'

boundn = 'Input/rivers/Reno_2018_2019.txt'

$end

Lamone

$bound13

kbound =

692 693

ibtyp = 2

salt = 15.000000

tempn = 'Input/rivers/temp/Lamone_temp_new.txt'

boundn = 'Input/rivers/Lamone_2018_2019.txt'

$end

Fiumi Uniti

$bound14

kbound =

770 771

ibtyp = 2

salt = 15.000000

tempn = 'Input/rivers/temp/FiumiUniti_temp_new.txt'

boundn = 'Input/rivers/Fiumi_uniti_2018_2019.txt'

$end

Bevano

$bound15

kbound =

781 782

ibtyp = 2

salt = 15.000000

tempn = 'Input/rivers/temp/Bevano_temp_new.txt'

boundn = 'Input/rivers/Bevano_2018_2019.txt'

$end

Savio

$bound16

kbound =

797 798

ibtyp = 2

salt = 15.000000

tempn = 'Input/rivers/temp/Savio_temp_new.txt'

boundn = 'Input/rivers/Savio_2018_2019.txt'

$end

Rubicone

$bound17

kbound =

861 862

ibtyp = 2

salt = 15.000000

tempn = 'Input/rivers/temp/Rubicone_temp_new.txt'

boundn = 'Input/rivers/Rubicone_2018_2019.txt'

$end

Uso

$bound18

kbound =

875 876

ibtyp = 2

salt = 15.000000

tempn = 'Input/rivers/temp/Uso_temp_new.txt'

boundn = 'Input/rivers/Uso_2018_2019.txt'

$end

Marecchia

$bound19

kbound =

913 914

ibtyp = 2

salt = 15.000000

tempn = 'Input/rivers/temp/Marecchia_temp_new.txt'

boundn = 'Input/rivers/Marecchia_2018_2019.txt'

$end

Bocca di Tolle

$bound20

kbound =

250 251

ibtyp = 2

salt = 17.000000

tempn = 'Input/rivers/temp/Busa_toll_temp_new.txt'

boundn = 'Input/rivers/bocca_tolle.dat'

sed2dn = 'Input/rivers/sed/sed4_new_bocca_tolle.dat'

$end

$name

tempin = 'Input/tempin.dat'

saltin = 'Input/saltin.dat'

wind = 'Input/wp.dat'

qflux = 'Input/tc.dat'

gotmpa = 'Input/gotmturb.nml'

rain = 'Input/rain.dat'

$end

Appendix B

Example of sediment forcing file

The example file shown is for a simulation with four sediment classes (four grainsizes specified in ***sedgrs***) and it is taken from the boundary of Busa di Dritta, which has three boundary nodes.

0 2 957839 3 1 4 1

20190101 00000

concentration [kg/m3]

0.003269774099899

0.003269774099899

0.003269774099899

concentration [kg/m3]

0.003269774099899

0.003269774099899

0.003269774099899

concentration [kg/m3]

0.003269774099899

0.003269774099899

0.003269774099899

concentration [kg/m3]

0.003269774099899

0.003269774099899

0.003269774099899

0 2 957839 3 1 4 1

20190102 00000

concentration [kg/m3]

0.003198793198524

0.003198793198524

0.003198793198524

concentration [kg/m3]

0.003198793198524

0.003198793198524

0.003198793198524

concentration [kg/m3]

0.003198793198524

0.003198793198524

0.003198793198524

concentration [kg/m3]

0.003198793198524

0.003198793198524

0.003198793198524

Appendix C

Satellite dates of 2019 with Sentinel 2 and maximum 30% of cloud cover

The red dates are the ones used for the RMSE calculations in the sensitivity analysis, while the blue ones are the ones used in the one-year simulation and the magenta ones are used for both.

04.01.2019, 06.01.2019, 14.01.2019, 16.01.2019, 24.01.2019, 29.01.2019, 31.01.2019

05.02.2019, 08.02.2019, 13.02.2019, 18.02.2019, 23.02.2019, 25.02.2019, 28.02.2019

02.03.2019, 12.03.2019, 15.03.2019, 17.03.2019, 20.03.2019, 22.03.2019, 25.03.2019, 30.03.2019

01.04.2019, 16.04.2019, 19.04.2019

01.05.02019, 16.05.2019, 24.05.2019

03.06.2019, 13.06.2019, 18.06.2019, 20.06.2019, 23.06.2019, textcolorblue25.06.2019, 28.06.2019, 30.06.2019

03.07.2019, 05.07.2019, 20.07.2019, 23.07.2019, 25.07.2019, 30.07.2019

04.08.2019, 09.08.2019, 19.08.2019, 27.08.2019, 29.08.2019

11.09.2019, 13.09.2019, 16.09.2019, 21.09.2019

08.10.2019, 11.10.2019, 16.10.2019, 21.10.2019, 26.10.2019

07.11.2019, 10.11.2019

10.12.2019, 25.12.2019, 30.12.2019

Appendix D

Simulation names and their respective setups

Name	Period	Sed classes at seabed	Sed classes at river mouths	transport rate method	Settling velocity	Sed density [kgm^{-3}]	Sed critical stress [Pa]	sedhpar	waves	Savio Reno forcing
Event03_4tauin	20.03.2019-05.04.2019	4 classes, 25% each	4 classes, 25% each	Van Rijn (1993)	Soulsby (1997)	2650	0.058, 0.098, 0.15, 0.22	0	Yes	X
Event03_tauin0.02	20.03.2019-05.04.2019	4 classes, 25% each	4 classes, 25% each	Van Rijn (1993)	Soulsby (1997)	2650	0.02 for all	0	Yes	X
Event03_Stokes	20.03.2019-05.04.2019	4 classes, 25% each	4 classes, 25% each	Van Rijn (1993)	Stokes law	2650	0.058, 0.098, 0.15, 0.22	0	Yes	X
Event03_ENGHAN	20.03.2019-05.04.2019	4 classes, 25% each	4 classes, 25% each	Engelund & Hansen (1967)	Soulsby (1997)	2650	0.058, 0.098, 0.15, 0.22	0	Yes	X
Event03_2sed	20.03.2019-05.04.2019	4 classes, 25% each	2 classes (32.5 & 94 μm), 50% each	Van Rijn (1993)	Soulsby (1997)	2650	0.058, 0.098, 0.15, 0.22	0	Yes	X
Event03_2sedfin	20.03.2019-05.04.2019	4 classes, 25% each & 0 of 14 μm	2 classes (14 & 32.5 μm), 50% each	Van Rijn (1993)	Soulsby (1997)	2650	0.058, 0.098, 0.15, 0.22	0	Yes	X
Event03_nowaves	20.03.2019-05.04.2019	4 classes, 25% each	4 classes, 25% each	Van Rijn (1993)	Soulsby (1997)	2650	0.058, 0.098, 0.15, 0.22	0	No	X
Event03_sedhpar0.005	20.03.2019-05.04.2019	4 classes, 25% each	4 classes, 25% each	Van Rijn (1993)	Soulsby (1997)	2650	0.058, 0.098, 0.15, 0.22	0.005	Yes	X
Event03_sedhpar0.01	20.03.2019-05.04.2019	4 classes, 25% each	4 classes, 25% each	Van Rijn (1993)	Soulsby (1997)	2650	0.058, 0.098, 0.15, 0.22	0.01	Yes	X
Event03_sedhpar0.05	20.03.2019-05.04.2019	4 classes, 25% each	4 classes, 25% each	Van Rijn (1993)	Soulsby (1997)	2650	0.058, 0.098, 0.15, 0.22	0.05	Yes	X
Event03_sedhpar0.1	20.03.2019-05.04.2019	4 classes, 25% each	4 classes, 25% each	Van Rijn (1993)	Soulsby (1997)	2650	0.058, 0.098, 0.15, 0.22	0.1	Yes	X
Event03_sedhpar0.2	20.03.2019-05.04.2019	4 classes, 25% each	4 classes, 25% each	Van Rijn (1993)	Soulsby (1997)	2650	0.058, 0.098, 0.15, 0.22	0.2	Yes	X
Event03_sedhpar1	20.03.2019-05.04.2019	4 classes, 25% each	4 classes, 25% each	Van Rijn (1993)	Soulsby (1997)	2650	0.058, 0.098, 0.15, 0.22	1	Yes	X
Event03_rhos1800	20.03.2019-05.04.2019	4 classes, 25% each	4 classes, 25% each	Van Rijn (1993)	Soulsby (1997)	1800	0.058, 0.098, 0.15, 0.22	0	Yes	X
Event03_SavioReno	20.03.2019-05.04.2019	4 classes, 25% each	4 classes, 25% each	Van Rijn (1993)	Soulsby (1997)	2650	0.058, 0.098, 0.15, 0.22	0	Yes	constant
Event03_SavioReno2	20.03.2019-05.04.2019	4 classes, 25% each	4 classes, 25% each	Van Rijn (1993)	Soulsby (1997)	2650	0.058, 0.098, 0.15, 0.22	0	Yes	weighted
Event10_4tauin	18.10.2019-31.12.2019	4 classes, 25% each	4 classes, 25% each	Van Rijn (1993)	Soulsby (1997)	2650	0.058, 0.098, 0.15, 0.22	0	Yes	X
Event10_tauin0.02	18.10.2019-31.12.2019	4 classes, 25% each	4 classes, 25% each	Van Rijn (1993)	Soulsby (1997)	2650	0.02 for all	0	Yes	X
Event10_Stokes	18.10.2019-31.12.2019	4 classes, 25% each	4 classes, 25% each	Van Rijn (1993)	Stokes law	2650	0.058, 0.098, 0.15, 0.22	0	Yes	X
Event10_ENGHAN	18.10.2019-31.12.2019	4 classes, 25% each	4 classes, 25% each	Engelund & Hansen (1967)	Soulsby (1997)	2650	0.058, 0.098, 0.15, 0.22	0	Yes	X
Event10_2sed	18.10.2019-31.12.2019	4 classes, 25% each	2 classes (32.5 & 94 μm), 50% each	Van Rijn (1993)	Soulsby (1997)	2650	0.058, 0.098, 0.15, 0.22	0	Yes	X
Event10_2sedfin	18.10.2019-31.12.2019	4 classes, 25% each & 0 of 14 μm	2 classes (14 & 32.5 μm), 50% each	Van Rijn (1993)	Soulsby (1997)	2650	0.058, 0.098, 0.15, 0.22	0	Yes	X
Event10_nowaves	18.10.2019-31.12.2019	4 classes, 25% each	4 classes, 25% each	Van Rijn (1993)	Soulsby (1997)	2650	0.058, 0.098, 0.15, 0.22	0	No	X
Event10_sedhpar0.005	18.10.2019-31.12.2019	4 classes, 25% each	4 classes, 25% each	Van Rijn (1993)	Soulsby (1997)	2650	0.058, 0.098, 0.15, 0.22	0.005	Yes	X
Event10_sedhpar0.01	18.10.2019-31.12.2019	4 classes, 25% each	4 classes, 25% each	Van Rijn (1993)	Soulsby (1997)	2650	0.058, 0.098, 0.15, 0.22	0.01	Yes	X
Event10_sedhpar0.05	18.10.2019-31.12.2019	4 classes, 25% each	4 classes, 25% each	Van Rijn (1993)	Soulsby (1997)	2650	0.058, 0.098, 0.15, 0.22	0.05	Yes	X
Event10_sedhpar0.1	18.10.2019-31.12.2019	4 classes, 25% each	4 classes, 25% each	Van Rijn (1993)	Soulsby (1997)	2650	0.058, 0.098, 0.15, 0.22	0.1	Yes	X
Event10_sedhpar0.2	18.10.2019-31.12.2019	4 classes, 25% each	4 classes, 25% each	Van Rijn (1993)	Soulsby (1997)	2650	0.058, 0.098, 0.15, 0.22	0.2	Yes	X
Event10_sedhpar1	18.10.2019-31.12.2019	4 classes, 25% each	4 classes, 25% each	Van Rijn (1993)	Soulsby (1997)	2650	0.058, 0.098, 0.15, 0.22	1	Yes	X
Event10_rhos1800	18.10.2019-31.12.2019	4 classes, 25% each	4 classes, 25% each	Van Rijn (1993)	Soulsby (1997)	1800	0.058, 0.098, 0.15, 0.22	0	Yes	X
Event10_SavioReno	18.10.2019-31.12.2019	4 classes, 25% each	4 classes, 25% each	Van Rijn (1993)	Soulsby (1997)	2650	0.058, 0.098, 0.15, 0.22	0	Yes	constant
Event10_SavioReno2	18.10.2019-31.12.2019	4 classes, 25% each	4 classes, 25% each	Van Rijn (1993)	Soulsby (1997)	2650	0.058, 0.098, 0.15, 0.22	0	Yes	weighted

Acknowledgments

Every day I try to ask myself "What do you want to be when you grow up?" and I still do not have a precise answer. Sometimes, not knowing my next step or what to do scares me but growing up I figured that everything goes into place if you keep going on and trust the process. For example, in 2020 I was finishing my master's degree in the Netherlands, and I was applying for a position in Boskalis, the dredging company with whom I did my thesis project, when Covid-19 happened, and all my plans changed. First thing that changed was that I was not going to stay in the Netherlands, because I wanted to be closer to my family and be back in Italy, not knowing how things would have evolved. Second, job offers were being withdrawn and finding something, as a newly graduated student, did not seem an easy task. In the midst of all this, my mom called me and told me of this PhD in Bologna that a family friend was doing. I applied with only one week of time before the deadline, not confident at all that I was going to get in. Since then, it has been a rollercoaster, both emotionally and physically, and I still do not know what I want to be when I grow up, but this journey has made me stronger and more aware of myself. I am immensely proud for reaching the end and I am curious of what the future will offer me.

Out of all the people that have helped me during these four years I wanted to thank my two supervisors Andrea and Nadia, that with their guidance and knowledge allowed me to reach this goal. With them I also want to mention my two co-supervisors Jacopo and Ivan, that have mainly helped me with the practical aspects of this research and without them I would have had a extremely challenging time with SHYFEM. I also want to give a special thanks to my supervisor in Lisbon, Andre Fortunato, whom during my period abroad made me feel at home and we managed to make my stay in Lisbon fruitful, even with all the technical problems that I faced. A big thank you also goes to my coworkers at Arpae, especially to Silvia, Anna, and

Margherita, that have always made me laugh when needed, helped me see things in other ways and, above all, made me feel accepted.

Besides the people that I worked with, a special thank you goes to my two grandmas, that have always been inspirational for me, and I love them dearly. Grazie Nonna Espana e Grazie Nonna Maria Stefania. Thank you to my cousins and friends, that have always been there for me and helped me through this journey. Thank you also to my boyfriend, who had to deal with my mood swings and accept my constant commute to Bologna. Grazie Federico. However, the biggest thank you goes to my parents, that have granted me this possibility and have been by my side through all of it. Without them I would surely not be here. Grazie Mamma e Grazie Papà, devo tutto a voi.

PS: thank you also to my two pets, Accipicchia and Cotakinabalu, that have offered me immense comfort during the darkest period and immense joy in the brightest ones.

Grazie a tutti,

Emilia Rizzi

Bibliography

Alessandri, J. (2022). *Coastal modelling studies for forecasting and remediation solutions*. PhD thesis, University of Bologna.

Allen, R. M., Lacy, J. R., and Stevens, A. W. (2021). Cohesive sediment modeling in a shallow estuary: Model and environmental implications of sediment parameter variation. *Journal of Geophysical Research: Oceans*, 126(9).

Alvisi, F., Cibic, T., Fazi, S., Bongiorni, L., Relitti, F., and Del Negro, P. (2019). Role of depositional dynamics and riverine input in shaping microbial benthic community structure of po prodelta system (nw adriatic, italy). *Estuarine, Coastal and Shelf Science*, 227:106305.

Amorosi, A., Sammartino, I., Dinelli, E., Campo, B., Guercia, T., Trincardi, F., and Pellegrini, C. (2022). Provenance and sediment dispersal in the po-adriatic source-to-sink system unraveled by bulk-sediment geochemistry and its linkage to catchment geology. *Earth-Science Reviews*, 234.

Amoudry, L. O. and Souza, A. J. (2011). Deterministic coastal morphological and sediment transport modeling: A review and discussion. *Reviews of Geophysics*, 49(2).

Artegiani, A., Bregant, D., and Paschini, E. (1998). The adriatic sea general circulation. part ii: baroclinic circulation structure. *Oceanographic Literature Review*, 3(45):445.

Bagnold, R. (1963). Mechanics of marine sedimentation. *The sea*, 3:507–528.

Bever, A. J., Harris, C. K., Sherwood, C. R., and Signell, R. P. (2009). Deposition and flux of sediment from the po river, italy: An idealized and wintertime numerical modeling study. *Marine Geology*, 260(1-4):69–80.

Bezzi, A., Pillon, S., Popesso, C., Casagrande, G., Da Lio, C., Martinucci, D., Tosi, L., and Fontolan, G. (2021). From rapid coastal collapse to slow sedimentary recovery: The morphological ups and downs of the modern po delta. *Estuarine, Coastal and Shelf Science*, 260:107499.

Billi, P. and Spalevic, V. (2022). Suspended sediment yield in italian rivers. *CATENA*, 212.

Bitelli, G., Bonsignore, F., Del Conte, S., Franci, F., Lambertini, A., Novali, F., Severi, P., and Vittuari, L. (2020). Updating the subsidence map of emilia-romagna region (italy) by integration of sar interferometry and gnss time series: The 2011–2016 period. *Proceedings of the International Association of Hydrological Sciences*, 382:39–44.

Blair, T. C. and McPherson, J. G. (1999). Grain-size and textural classification of coarse sedimentary particles. *Journal of Sedimentary Research*, 69(1):6–19.

Blumberg, A. F. and Mellor, G. L. (1987). A description of a three-dimensional coastal ocean circulation model. *Three-dimensional coastal ocean models*, 4:1–16.

Bonaldo, D., Benetazzo, A., Sclavo, M., and Carniel, S. (2015). Modelling wave-driven sediment transport in a changing climate: a case study for northern adriatic sea (italy). *Regional Environmental Change*, 15:45–55.

Bondesan, M. (1990). L'area deltizia padana: caratteri geografici e geomorfologici. *Il parco del delta del Po. Studi e immagini*, 1:9–48.

Bosman, A., Romagnoli, C., Madricardo, F., Correggiari, A., Remia, A., Zubalich, R., Fogarin, S., Kruss, A., and Trincardi, F. (2020). Short-term evolution of po della pila delta lobe from time lapse high-resolution multibeam bathymetry (2013–2016). *Estuarine, Coastal and Shelf Science*, 233.

Brambati, A., Bregant, D., Lenardon, G., and Stolfa, D. (1973). *Transport and sedimentation in the Adriatic Sea*. Museo Friulano di Storia Naturale.

Brown, C. B. (1950). Sediment transport, in engineering hydraulics. *John Willey and Sons, New York*.

Burchard, H., Bolding, K., and Villarreal, M. (1999). Gotm, a general ocean turbulence model: Theory. *Implementation and Test Cases*, page 103.

Campos-Caba, R., Alessandri, J., Camus, P., Mazzino, A., Ferrari, F., Federico, I., Vousdoukas, M., Tondello, M., and Mentaschi, L. (2024). Assessing storm surge model performance: what error indicators can measure the model's skill? *Ocean Science*, 20(6):1513–1526.

Cattaneo, A., Correggiari, A., Langone, L., and Trincardi, F. (2003). The late-holocene gargano subaqueous delta, adriatic shelf: sediment pathways and supply fluctuations. *Marine Geology*, 193(1-2):61–91.

Cavaleri, L. and Bertotti, L. (1997). In search of the correct wind and wave fields in a minor basin. *Monthly weather review*, 125(8):1964–1975.

Cavaleri, L., Fox-Kemper, B., and Hemer, M. (2012). Wind waves in the coupled climate system. *Bulletin of the American Meteorological Society*, 93(11):1651–1661.

Celano, M. and Stanzani, R. (2019). Rapporto dell'evento meteorologico del 25 e 26 marzo 2019. Technical report, Arpae Emilia-Romagna - Struttura Idro-Meteo-Clima.

Cencini, C. (1998). Physical processes and human activities in the evolution of the po delta, italy. *Journal of Coastal Research*, pages 775–793.

Center, U. C. E. R. (1984). *Shore protection manual*. United States. Army. Corps of Engineers, 1 edition.

Ciabatti, M. (1967). Ricerche sull'evoluzione del delta padano. *Geornale di Geologia*, 34:381–406.

Ciavola, P., Armaroli, C., Chiggiato, J., Valentini, A., Deserti, M., Perini, L., and Luciani, P. (2007). Impact of storms along the coastline of emilia-romagna: the morphological signature on the ravenna coastline (italy). *Journal of Coastal Research*, pages 540–544.

Cilli, S., Billi, P., Schippa, L., Grottoli, E., and Ciavola, P. (2018). Field data and regional modeling of sediment supply to emilia-romagna's river mouths. In *E3S Web of Conferences*, volume 40. EDP Sciences.

Cilli, S., Billi, P., Schippa, L., Grottoli, E., and Ciavola, P. (2020). Bedload transport processes in a coastal sand-bed river: The study case of fiumi uniti river in the northern adriatic. *Mathematical Approach to Climate Change and its Impacts: MAC2I*, pages 133–145.

Cilli, S., Billi, P., Schippa, L., Grottoli, E., and Ciavola, P. (2021). Bedload transport and dune bedforms characteristics in sand-bed rivers supplying a retreating beach of the northern adriatic sea (italy). *Journal of Hydrology: Regional Studies*, 37.

Colella, S., Böhm, E., Cesarini, C., Garnesson, P., Netting, J., and Calton, B. (2023). *PRODUCT USER MANUAL For Ocean Colour Products*. Copernicus Marine Service, 4.0 edition.

Corbau, C., Zambello, E., Nardin, W., and Simeoni, U. (2022). Secular diachronic analysis of coastal marshes and lagoons evolution: Study case of the po river delta (italy). *Estuarine, Coastal and Shelf Science*, 268.

Correggiari, A., Cattaneo, A., and Trincardi, F. (2005). The modern po delta system: Lobe switching and asymmetric prodelta groth. *Marine Geology*, 223:49–74.

de Oliveira Fagundes, H., de Paiva, R. C. D., Fan, F. M., Buarque, D. C., and Fassoni-Andrade, A. C. (2020). Sediment modeling of a large-scale basin supported by remote sensing and in-situ observations. *Catena*, 190:104535.

Douglas, B. C. (1997). Global sea rise: a redetermination. *Surveys in Geophysics*, 18(2):279–292.

Dunn, F. E., Darby, S. E., Nicholls, R. J., Cohen, S., Zarfl, C., and Fekete, B. M. (2019). Projections of declining fluvial sediment delivery to major deltas worldwide in response to climate change and anthropogenic stress. *Environmental Research Letters*, 14(8):084034.

Egbert, G. D. and Erofeeva, S. Y. (2002). Efficient inverse modeling of barotropic ocean tides. *Journal of Atmospheric and Oceanic technology*, 19(2):183–204.

Engelund, F. and Hansen, E. (1967). A monograph on sediment transport in alluvial streams. *Technical University of Denmark 0stervoldgade 10, Copenhagen K.*

Fain, A., Ogston, A., and Sternberg, R. (2007). Sediment transport event analysis on the western adriatic continental shelf. *Continental Shelf Research*, 27(3-4):431–451.

Ferrarin, C., Cucco, A., Umgiesser, G., Bellafiore, D., and Amos, C. L. (2010). Modelling fluxes of water and sediment between venice lagoon and the sea. *Continental Shelf Research*, 30(8):904–914.

Ferrarin, C., Umgiesser, G., Cucco, A., Hsu, T.-W., Roland, A., and Amos, C. L. (2008). Development and validation of a finite element morphological model for shallow water basins. *Coastal Engineering*, 55(9):716–731.

Ferrarin, C., Umgiesser, G., Roland, A., Bajo, M., De Pascalis, F., Ghezzo, M., and Scroccaro, I. (2016). Sediment dynamics and budget in a microtidal lagoon—a numerical investigation. *Marine Geology*, 381:163–174.

Filipponi, F., Taramelli, A., Zucca, F., Valentini, E., and El Serafy, G. (2015). Ten-years sediment dynamics in northern adriatic sea investigated through optical remote sensing observations. In *2015 IEEE International Geoscience and Remote Sensing Symposium (IGARSS)*, pages 2265–2268. IEEE.

Friedrichs, C. and Scully, M. (2007). Modeling deposition by wave-supported gravity flows on the po river subaqueous delta: From seasonal floods to prograding clinoforms. *Continental Shelf Research*, 27.

Frignani, M., Langone, L., Ravaioli, M., Sorgente, D., Alvisi, F., and Albertazzi, S. (2005). Fine-sediment mass balance in the western adriatic continental shelf over a century time scale. *Marine Geology*, 222:113–133.

Gallina, V., Torresan, S., Zabeo, A., Rizzi, J., Carniel, S., Sclavo, M., Pizzol, L., Marcomini, A., and Critto, A. (2019). Assessment of climate change impacts in the north adriatic coastal area. part ii: Consequences for coastal erosion impacts at the regional scale. *Water*, 11(6):1300.

Garnesson, P., Mangin, A., Bretagnon, M., and Jutard, Q. (2024). Ocean colour production centre. satellite observation. copernicus-globcolour products. Quality information document 5.0, Copernicus Marine Service.

Group, W. I. D. (2016). *User manual and system documentation of WAVEWATCH III version 5.16*.

Guarnieri, A., Souza, A., Pinardi, N., and Traykovski, P. (2014). Numerical modelling of sediment transport in the adriatic sea. Copernicus GmbH.

Guarnieri-Minnucci, A. (2011). *Climate impact studies of sediment transport on the Adriatic coastal zone*. PhD thesis, University of Bologna.

Harley, M. D., Valentini, A., Armaroli, C., Ciavola, P., Perini, L., Calabrese, L., Marucci, F., et al. (2012). An early warning system for the on-line prediction of coastal storm risk on the italian coastline. *Coastal Engineering Proceedings*, 1(33).

Harris, C. K., Sherwood, C. R., Signell, R. P., Bever, A. J., and Warner, J. C. (2008). Sediment dispersal in the northwestern adriatic sea. *Journal of Geophysical Research: Oceans*, 113(C11).

Ji, C., Zhang, Q., Chen, T., Ma, D., and Huang, R. (2024). Modeling investigation of wave-induced longshore current distribution patterns on barred beaches. *Estuarine, Coastal and Shelf Science*, 229(108685).

Kettner, A. J. and Syvitski, J. P. (2008). Predicting discharge and sediment flux of the po river, italy since the last glacial maximum. *Analogue and numerical modelling of sedimentary systems: From understanding to prediction*.

King, E. V., Conley, D. C., Masselink, G., and Leonardi, N. (2021). Predicting dominance of sand transport by waves, tides, and their interactions on sandy continental shelves. *Journal of Geophysical Research: Oceans*, 126(9).

Kroon, M. E. (2016). Design method for multi-functional artificial reefs in a coastal environment.

Lecci, R., Drudi, M., Grandi, A., Cretì, S., and Clementi, E. (2022). *For Mediterranean Sea Physical Reanalysis Product MEDSEA_MULTIYEAR_PHY_006_004*, 2.3 edition.

Lee, C., Schwab, D. J., Beletsky, D., Stroud, J., and Lesht, B. (2007). Numerical modeling of mixed sediment resuspension, transport, and deposition during the march 1998 episodic events in southern lake michigan. *Journal of Geophysical Research: Oceans*, 112(C2).

Lesser, G., Roelvink, J., van Kester, J., and Stelling, G. (2004). Development and validation of a three-dimensional morphological model. *Coastal Engineering*, 51(8):883–915.

Li, L., Ren, Y., Wang, X. H., and Xia, Y. (2022). Sediment dynamics on a tidal flat in macro-tidal hangzhou bay during typhoon mitag. *Continental Shelf Research*, 237.

Li, M. Z. and Amos, C. L. (2001). Sedtrans96: the upgraded and better calibrated sediment-transport model for continental shelves. *Computers & Geosciences*, 27(6):619–645.

Luijendijk, A., Hagenaars, G., Ranasinghe, R., Baart, F., Donchyts, G., and Aarninkhof, S. (2018). The state of the world's beaches. *Scientific reports*, 8(1):1–11.

Maicu, F., Alessandri, J., Pinardi, N., Verri, G., Umgiesser, G., Lovo, S., Turolla, S., Paccagnella, T., and Valentini, A. (2021). Downscaling with an unstructured coastal-ocean model to the goro lagoon and the po river delta branches. *Frontiers in Marine Science*, 8.

Marchetti, M., Motta, R., Pettenella, D., Sallustio, L., Vacchiano, G., et al. (2018). Le foreste e il sistema foresta-legno in italia: verso una nuova strategia per rispondere alle sfide interne e globali. *Forest@*, 15:41–50.

Margvelashvili, N., Andrewartha, J., Herzfeld, M., Robson, B. J., and Brando, V. E. (2013). Satellite data assimilation and estimation of a 3d coastal sediment transport model using error-subspace emulators. *Environmental Modelling & Software*, 40:191–201.

Martínez, M. L., Intralawan, A., Vázquez, G., Pérez-Maqueo, O., Sutton, P., and Landgrave, R. (2007). The coasts of our world: Ecological, economic and social importance. *Ecological economics*, 63(2-3):254–272.

Melià, P., Schiavina, M., Rossetto, M., Gatto, M., Fraschetti, S., and Casagrandi, R. (2016). Melia et al 2016 srep supp.

Micaletto, G., Barletta, I., Mocavero, S., Federico, I., Epicoco, I., Verri, G., Coppini, G., Schiano, P., Aloisio, G., and Pinardi, N. (2021). Parallel implementation of the shyfem model. doi: 10.5194/gmd-2021-319.

Miller, M., McCave, I., and Komar, P. (1977). Threshold of sediment motion under unidirectional currents. *Sedimentology*, 24(4):507–527.

Miller, R. L. and McKee, B. A. (2004). Using modis terra 250 m imagery to map concentrations of total suspended matter in coastal waters. *Remote sensing of Environment*, 93(1-2):259–266.

Milligan, T. G. and Cattaneo, A. (2007). Sediment dynamics in the western adriatic sea: From transport to stratigraphy. *Continental Shelf Research*, 27(3):287–295.

Milliman, J. D. and Syvitski, J. P. (1992). Geomorphic/tectonic control of sediment discharge to the ocean: the importance of small mountainous rivers. *The journal of Geology*, 100(5):525–544.

Nelson, B. W. (1970). Hydrography, sediment dispersal, and recent historical development of the po river delta, italy1. In *Deltaic Sedimentation, Modern and Ancient*. SEPM Society for Sedimentary Geology.

Neumann, B., Vafeidis, A. T., Zimmermann, J., and Nicholls, R. J. (2015). Future coastal population growth and exposure to sea-level rise and coastal flooding-a global assessment. *PloS one*, 10(3):e0118571.

Neumeier, U., Ferrarin, C., Amos, C. L., Umgiesser, G., and Li, M. Z. (2008). Sedtrans05: An improved sediment-transport model for continental shelves and coastal waters with a new algorithm for cohesive sediments. *Computers & Geosciences*, 34(10):1223–1242.

Oddo, P., Pinardi, N., and Zavatarelli, M. (2005). A numerical study of the interannual variability of the adriatic sea (2000–2002). *Science of The Total Environment*, 353(1):39–56. Mucilages in the Adriatic and Tyrrhenian Seas.

Orlic, M., Gacic, M., and Laviolette, P. (1992). The currents and circulation of the adriatic sea. *Oceanologica acta*, 15(2):109–124.

Ouillon, S., Douillet, P., and Andréfouët, S. (2004). Coupling satellite data with in situ measurements and numerical modeling to study fine suspended-sediment transport: a study for the lagoon of new caledonia. *Coral Reefs*, 23:109–122.

Owens, R. G. and Hewson, T. (2018). *ECMWF forecast user guide*. ECMWF, 10 edition.

Palinkas, C. and Nittrouer, C. (2007). Modern sediment accumulation on the po shelf, adriatic sea. *Continental Shelf Research*, 27(3-4):489–505.

Palinkas, C., Nittrouer, C., Wheatcroft, R., and Langone, L. (2005). The use of 7be to identify event and seasonal sedimentation near the po river delta, adriatic sea. *Marine Geology*, 222:95–112.

Pandey, A., Himanshu, S. K., Mishra, S. K., and Singh, V. P. (2016). Physically based soil erosion and sediment yield models revisited. *Catena*, 147:595–620.

Pavan, V. and Marletto, V. (2020). Rapporto idrometeoclima emilia-romagna dati 2019. Technical report.

Pellegrini, C., Tesi, T., Schieber, J., Bohacs, K. M., Rovere, M., Asioli, A., Nogarotto, A., and Trincardi, F. (2021). Fate of terrigenous organic carbon in muddy clinothems on continental shelves revealed by stratal geometries: Insight from the adriatic sedimentary archive. *Global and Planetary Change*, 203:103539.

Pillai, U. P. A., Pinardi, N., Alessandri, J., Federico, I., Causio, S., Unguendoli, S., Valentini, A., and Staneva, J. (2022). A digital twin modelling framework for the assessment of seagrass nature based solutions against storm surges. *Science of the Total Environment*, 847.

Puig, P., Ogston, A. S., Guillén, J., Fain, A., and Palanques, A. (2007). Sediment transport processes from the topset to the foreset of a crenulated clinoform (adriatic sea). *Continental Shelf Research*, 27(3-4):452–474.

Raicich, F. (1994). Note on the flow rates of the adriatic rivers. Technical report, Tech. Rep. RF 02.

Ribbe, J. and Holloway, P. E. (2001). A model of suspended sediment transport by internal tides. *Continental Shelf Research*, 21(4):395–422.

Ricciardi, G. and Comune, E. (2019). Evento di piena del bacino del fiume po, novembre 2019. Technical report, Arpae Emilia-Romagna - Struttura Idro-Meteo-Clima, Bologna.

Sadeghian, A., Hudson, J., Wheater, H., and Lindenschmidt, K.-E. (2017). Sediment plume model—a comparison between use of measured turbidity data and satellite images for model calibration. *Environmental Science and Pollution Research*, 24:19583–19598.

Schippa, L., Cilli, S., Ciavola, P., and Billi, P. (2019). Dune contribution to flow resistance in alluvial rivers. *Water*, 11(10).

Sedrati, M., Ciavola, P., and Armaroli, C. (2011). Morphodynamic evolution of a microtidal barrier, the role of overwash: Bevano, northern adriatic sea. *Journal of Coastal Research*, pages 696–700.

Sherwood, C. R., Book, J. W., Harris, C. K., et al. (2015). Sediment dynamics in the adriatic sea investigated with coupled models. *Oceanography*, 17(4).

Simeoni, U., Bondesan, M., et al. (1997). The role and responsibility of man in the evolution of the adriatic alluvial coasts of italy. In *Transformation and evolution of the Mediterranean coastline*, volume 18, pages 111–132. Briand F., Maldonado A.

Simeoni, U. and Corbau, C. (2009). A review of the delta po evolution (italy) related to climatic changes and human impacts. *Geomorphology*, 107:64–71.

Simoncelli, S. (2010). *Towards Rapid Environmental Assessment and Coastal Forecasting inthe Northern Adriatic Sea*. PhD thesis, University of Bologna.

Smagorinsky, J. (1963). General circulation experiments with the primitive equations: I. the basic experiment. *Monthly weather review*, 91(3):99–164.

Smith, J. D. and McLean, S. (1977). Spatially averaged flow over a wavy surface. *Journal of Geophysical research*, 82(12):1735–1746.

Soulsby, R. (1997). *Dynamics of marine sands*, chapter Contents and Preliminary Pages, pages i–xxi. T. Telford London, UK.

Soulsby, R. L. and Whitehouse, R. J. (1997). Threshold of sediment motion in coastal environments. In *Pacific Coasts and Ports' 97: Proceedings of the 13th Australasian Coastal*

and Ocean Engineering Conference and the 6th Australasian Port and Harbour Conference; Volume 1, pages 145–150. Centre for Advanced Engineering, University of Canterbury, Christchurch, N.Z.

Spagnoli, F., Dinelli, E., Giordano, P., Marcaccio, M., Zaffagnini, F., and Frascari, F. (2014). Sedimentological, biogeochemical and mineralogical facies of northern and central western adriatic sea. *Journal of Marine Systems*, 139:183–203.

Stefani, M. and Vincenzi, S. (2005). The interplay of eustasy, climate and human activity in the late quaternary depositional evolution and sedimentary architecture of the po delta system. *Marine Geology*, 222:19–48.

Stevens, A., Wheatcroft, R., and Wiberg, P. (2007). Seabed properties and sediment erodibility along the western adriatic margin, italy. *Continental Shelf Research*, 27(3-4):400–416.

Stroud, J. R., Lesht, B. M., Schwab, D. J., Beletsky, D., and Stein, M. L. (2009). Assimilation of satellite images into a sediment transport model of lake michigan. *Water resources research*, 45(2).

Syvitski, J. P. and Kettner, A. J. (2007). On the flux of water and sediment into the northern adriatic sea. *Continental Shelf Research*, 27(3-4):296–308.

Syvitski, J. P., Kettner, A. J., Correggiari, A., and Nelson, B. W. (2005). Distributary channels and their impact on sediment dispersal. *Marine Geology*, 222:75–94.

Traykovski, P., Wiberg, P. L., and Geyer, W. R. (2007). Observations and modeling of wave-supported sediment gravity flows on the po prodelta and comparison to prior observations from the eel shelf. *Continental Shelf Research*, 27(3-4):375–399.

Umgiesser, G. (1986). A model for the venice lagoon. Master's thesis, University of Hamburg.

Umgiesser, G., Canu, D. M., Cucco, A., and Solidoro, C. (2004). A finite element model for the venice lagoon. development, set up, calibration and validation. *Journal of Marine Systems*, 51(1-4):123–145.

Umgiesser, G., De Pascalis, F., Ferrarin, C., and Amos, C. L. (2006). A model of sand transport in treporti channel: northern venice lagoon. *Ocean Dynamics*, 56:339–351.

Umgiesser, G., Ferrarin, C., Bajo, M., Bellafiore, D., Cucco, A., De Pascalis, F., Ghezzo, M., McKiver, W., and Arpaia, L. (2022). Hydrodynamic modelling in marginal and coastal seas—the case of the adriatic sea as a permanent laboratory for numerical approach. *Ocean Modelling*, 179:102–123.

Unguendoli, S., Biolchi, L. G., Aguzzi, M., Pillai, U. P. A., Alessandri, J., and Valentini, A. (2023). A modeling application of integrated nature based solutions (nbs) for coastal erosion and flooding mitigation in the emilia-romagna coastline (northeast italy). *Science of The Total Environment*, 867:161357.

Van Rijn, L. C. et al. (1993). *Principles of sediment transport in rivers, estuaries and coastal seas*, volume 1006. Aqua publications Amsterdam.

Verri, G., Barletta, I., Pinardi, N., Federico, I., Alessandri, J., and Coppini, G. (2023). Shelf slope, estuarine dynamics and river plumes in a z* vertical coordinate, unstructured grid model. *Ocean Modelling*, 184.

Verri, G., Pinardi, N., Oddo, P., Ciliberti, S. A., and Coppini, G. (2018). River runoff influences on the central mediterranean overturning circulation. *Climate Dynamics*, 50:1675–1703.

Villar, R. E., Martinez, J.-M., Le Texier, M., Guyot, J.-L., Fraizy, P., Meneses, P. R., and de Oliveira, E. (2013). A study of sediment transport in the madeira river, brazil, using modis remote-sensing images. *Journal of South American Earth Sciences*, 44:45–54.

Wang, X. and Pinardi, N. (2002). Modeling the dynamics of sediment transport and resuspension in the northern adriatic sea. *Journal of Geophysical Research: Oceans*, 107(C12).

Wang, X., Pinardi, N., and Malacic, V. (2007). Sediment transport and resuspension due to combined motion of wave and current in the northern adriatic sea during a bora event in january 2001: A numerical modelling study. *Continental Shelf Research*, 27(5):613–633.

Warner, J. C., Sherwood, C. R., Signell, R. P., Harris, C. K., and Arango, H. G. (2008). Development of a three-dimensional, regional, coupled wave, current, and sediment-transport model. *Computers & geosciences*, 34(10):1284–1306.

Wheatcroft, R. A., Stevens, A. W., Hunt, L. M., and Milligan, T. G. (2006). The large-scale distribution and internal geometry of the fall 2000 po river flood deposit: evidence from digital x-radiography. *Continental Shelf Research*, 26(4):499–516.

Wilcock, P. R. (1993). Critical shear stress of natural sediments. *Journal of Hydraulic Engineering*, 119(4):491–505.

Wu, L., Chen, C., Guo, P., Shi, M., Qi, J., and Ge, J. (2011). A fvcom-based unstructured grid wave, current, sediment transport model, i. model description and validation. *Journal of Ocean University of China*, 10:1–8.

Yalin, M. S. (1963). An expression for bed-load transportation. *Journal of the Hydraulics Division*, 89(3):221–250.

Zasso, M. and Settin, T. (2012). Sulla ripartizione delle portate del po tra i vari rami e le bocche a mare del delta: esperienze storiche e nuove indagini all'anno 2011. Technical Report 02/12, Arpav.

Zavatarelli, M. and Pinardi, N. (2003). The adriatic sea modelling system: a nested approach. *Annales Geophysicae*, 21(1):345–364.

Zavatarelli, M., Pinardi, N., Kourafalou, V., and Maggiore, A. (2002). Diagnostic and prognostic model studies of the adriatic sea general circulation: Seasonal variability. *Journal of Geophysical Research: Oceans*, 107(C1):2–1.

Zhu, C., Guo, L., van Maren, D., Wang, Z. B., and He, Q. (2021). Exploration of decadal tidal evolution in response to morphological and sedimentary changes in the yangtze estuary. *Journal of Geophysical Research: Oceans*, 126(9).